IN SITU TRANSMISSION ELECTRON MICROSCOPY CHARACTERIZATION OF NANOMATERIALS

A Dissertation

by

JOON HWAN LEE

Submitted to the Office of Graduate Studies of
Texas A&M University
in partial fulfillment of the requirements for the degree of

DOCTOR OF PHILOSOPHY

Approved by:

Chair of Committee,	Haiyan Wang
Committee Members,	Xinghang Zhang
	Lin Shao
	Jun Kameoka
Intercollegiate Faculty Chair,	Ibrahim Karaman

December 2012

Major Subject: Materials Science and Engineering

ABSTRACT

With the recent development of *in situ* transmission electron microscopy (TEM) characterization techniques, the real time study of property-structure correlations in nanomaterials becomes possible. This dissertation reports the direct observations of deformation behavior of Al_2O_3-ZrO_2-$MgAl_2O_4$ (AZM) bulk ceramic nanocomposites, strengthening mechanism of twins in $YBa_2Cu_3O_{7-x}$ (YBCO) thin film, work hardening event in nanocrystalline nickel and deformation of 2wt% Al doped ZnO (AZO) thin film with nanorod structures using the *in situ* TEM nanoindentation tool. The combined *in situ* movies with quantitative loading-unloading curves reveal the deformation mechanism of the above nanomaterial systems.

At room temperature, *in situ* dynamic deformation studies show that the AZM nanocomposites undergo the deformation mainly through the grain-boundary sliding and rotation of small grains, i.e., ZrO2 grains, and some of the large grains, i.e., MgAl2O4 grains. We observed both plastic and elastic deformations in different sample regions in these multi-phase ceramic nanocomposites at room temperature.

Both *ex situ* (conventional) and *in situ* nanoindentation were conducted to reveal the deformation of YBCO films from the directions perpendicular and parallel to the twin interfaces. Hardness measured perpendicular to twin interfaces is ~50% and 40% higher than that measured parallel to twin interfaces, by *ex situ* and *in situ*, respectively.

By using an *in situ* nanoindentation tool inside TEM, dynamic work hardening event in nanocrystalline nickel was directly observed. During stain hardening stage, abundant Lomer-Cottrell (L-C) locks formed both within nanograins and against twin boundaries. Two major mechanisms were identified during interactions between L-C locks and twin boundaries. Quantitative nanoindentation experiments recorded during *in situ* experiments show an increase of yield strength from 1.64 to 2.29 GPa during multiple loading-unloading cycles.

In situ TEM nanoindentation has been conducted to explore the size dependent deformation behavior of two different types (type I: ~ 0.51 of width/length ratio and type II: ~ 088 ratio) of AZO nanorods. During the indentation on type I nanord structure, annihilation of defects has been observed which is caused by limitation of the defect activities by relatively small size of the width. On the other hand, type II nanorod shows dislocation activities which enhanced the grain rotation under the external force applied on more isotropic direction through type II nanorod.

DEDICATION

To my beloved parents and sisters, to my teachers, and to my friends

ACKNOWLEDGEMENTS

I would like to express my deepest gratitude to my graduate advisor Prof. Haiyan Wang for her invaluable advice, financial support, and, especially, her academic guidance. She helped, stimulated, and encouraged me all the way through research and the dissertation writing. She is one of the best professors that I have met in my life. Dr. Wang sets high standards for her students and she encourages and guides us to meet those standards. Her teachings greatly inspired me during my graduate study.

I would like to thank Prof. Xinghang Zhang, Prof. Lin Shao and Prof. Jun Kameoka as my committee members and their guidance and support throughout the course of my graduate study. I also want to thank my friends and labmates in the thin film characterization group, Chen-Fong Tsai, Michelle Myers, Qing Su, Aiping Chen, Li Chen and Fauzia Khatkatay, and the former graduates, Roy Araujo, Jongsik Yoon, Zhenxing Bi, Ickchan Kim, Tianlin Lu and Sungmee Cho for making my graduate years enjoyable and memorable. The facilities and resources provided by the Electrical and Computer Engineering Department, Texas A&M University, are greatly acknowledged.

Finally, I would like to thank to my father, mother and sisters for their encouragement and their supports during my entire study at Texas A&M University.

TABLE OF CONTENTS

Page

ABSTRACT..ii

DEDICATION..iv

ACKNOWLEDGEMENTS..v

TABLE OF CONTENTS..vi

LIST OF FIGURES..ix

LIST OF TABLES..xviii

CHAPTER I INTRODUCTION...1

- 1.1. Overview 1
- 1.2. Nanomaterials..4
  - 1.2.1. Bulk nanostructured materials...5
  - 1.2.2. Thin film materials 12
- 1.3. Material systems studied 24
  - 1.3.1. Al_2O_3-ZrO_2-$MgAl_2O_4$ ceramic nanocomposites 24
  - 1.3.2. Nanocrystalline nickel 26
  - 1.3.3. $YBa_2Cu_3O_{7-x}$ thin films...29
  - 1.3.4. Al doped ZnO 32
- 1.4. In situ TEM characterization 35
  - 1.4.1. In situ TEM nanoindentation...38
- 1.5. Summary...43

CHAPTER II RESEARCH METHODOLOGY 45

- 2.1. Transmission electron microscopy 45
  - 2.1.1. Resolution..46
  - 2.1.2. Depth of field and depth of focus 49
  - 2.1.3. Image and diffraction modes 50
  - 2.1.4. High resolution TEM (HRTEM) 52
- 2.2. Nanoindentation 53
- 2.3. In situ TEM nanoindentation system...57
  - 2.3.1. Major components of in situ nanoindentation system 58
  - 2.3.2. Nanoindentation tip and alignment with specimen under TEM 60
  - 2.3.3. Electronic control 63

2.3.4. Contact mechanics 64
2.4. X-ray diffraction 66
2.5. Pulsed laser deposition system 71
2.5.1. Interaction between the laser beam and target 75
2.5.2. Interaction of the laser beam with evaporated materials 77
2.5.3. Adiabatic plasma expansion and film deposition 79

CHAPTER III GRAIN AND GRAIN BOUNDARY ACTIVITIES OBSERVED IN ALUMINA-ZIRCONIA-MAGNESIA SPINEL NANOCOMPOSITES BY IN SITU NANOINDENTATION IN TRANSMISSION ELECTRON MICROSCOPE 81

3.1. Overview 81
3.2. Introduction 82
3.3. Experimental 84
3.4. Results and discussion 86
3.5. Conclusions 100

CHAPTER IV DIRECT OBSERVATION OF TWIN DEFORMATION IN YBCO THIN FILMS BY IN SITU NANOINDENTATION IN TEM 102

4.1. Overview 102
4.2. Introduction 103
4.3. Experimental 105
4.4. Results and discussion 107
4.5. Conclusions 120

CHAPTER V DIRECT OBSERVATION OF LOMER-COTTRELL LOCKS DURING STRAIN HARDENING IN NANOCRYSTALLINE NICKEL BY IN SITU TEM 121

5.1. Overview 121
5.2. Introduction 122
5.3. Experimental 124
5.4. Results and discussion 125
5.5. Conclusions 138

CHAPTER VI GROWTH-CONTROLLED SURFACE ROUGHNESS IN AL-DOPED ZNO AS TRANSPARENT CONDUCTING OXIDE 140

6.1. Overview 140
6.2. Introduction 141
6.3. Experimental 142
6.4. Results and discussion 143

        6.4.1. Microstructure and surface morphology 143
        6.4.2. Optical and electrical properties 153
    6.5. Conclusions 155

CHAPTER VII GROWTH OF AL-DOPED ZNO FILMS WITH TILTED NANO-COLUMNS ON R-CUT SAPPHIRE SUBSTRATES BY PULSED LASER DEPOSITION 156

    7.1. Overview 156
    7.2. Introduction 157
    7.3. Experimental details 158
    7.4. Results and discussion 160
        7.4.1. Microstructure and surface morphology 160
        7.4.2. Electrical properties 172
    7.5. Conclusions 174

CHAPTER VIII DIRECT OBSERVATION OF DEFORMATION BEHAVIOR OF AL DOPED ZNO NANORODS GROWN WITH DIFFERENT WIDTH/LENGTH RATIOS 176

    8.1. Overview 176
    8.2. Introduction 177
    8.3. Experimental details 179
    8.4. Results and discussion 181
    8.5. Conclusions 187

CHAPTER IX SUMMARY 189

REFERENCES 192

LIST OF FIGURES

Page

Figure 1.1. Reduction of transistor size based on physical gate length under Moore's Law [1]. 1

Figure 1.2. a) Influence of the pressure on the density of the ZrO_2 under 1200 °C with holding time of 5mins, b) effect of size of grain of alumina (Al_2O_3) by the holding time [29, 30]. 6

Figure 1.3. Schematic diagram showing different types of nanostructured ceramic materials: a) two-phased nanocomposite material b) inter/intra-granular nanocomposite material c) micro/nanostructured material d) inter-granular nanocomposite material and e) intra-granular nanocomposite material [6]. 9

Figure 1.4. Plots show clearly the increase of the stress as the grain sizes of nanocrystalline copper decreased from ~ 50 to ~12 nm [33]. 11

Figure 1.5. Plot shows increment of hardness of nickel based alloys along reduction of size of the twin spacing during the indentation test [36]. 11

Figure 1.6. Diagram illustrates the different gas flow regimes based on variation of the system dimensions and pressure [37]. 14

Figure 1.7. Schematic diagrams illustrate a) RF magnetron and b) DC sputtering systems. 16

Figure 1.8. Schematic diagram illustrate experiment set up for electrochemical deposition. 17

Figure 1.9. Schematic diagram illustrates the CVD process under the laminar flow based on the following steps: 1) transport of reactant by the convention of main stream, 2) diffuse of the reactant on the surface of substrate, 3) absorption of reactant, 4) surface process, 5) desorption of by-product, 6) diffuse to the main stream, 7) transport of the by-product. 19

Figure 1.10. Plot shows growth rate of film in mass transfer and reaction regimes based on deposition temperature variation during CVD process. 20

Figure 1.11. a) Schematic diagram illustrates the nucleation of solid particle as spherical formation. And during this process, b) plot shows the variation of the free energy. 22

Figure 1.12. Schematic diagram illustrates the different surface tensions acted between the film and substrate, film and vapor, and vapor and substrate while the film nucleated on substrate. 23

Figure 1.13. Schematic diagram illustrates YBCO perovskite crystal structure with copper (orange), oxygen (green) and barium (purple) atoms. 30

Figure 1.14. Schematic diagram illustrates ZnO hexagonal wurtzite crystal structure with zinc (red) and oxygen (purple) atoms [71]..32

Figure 2.1. Diagrams illustrate the objective aberrations: a) spherical b) chromatic, c) astigmatism [104]...47

Figure 2.2. Schematic diagrams illustrate depth of field and depth of focus [105]. 49

Figure 2.3. Schematic diagrams illustrate the basic operation of TEM imaging system under a) diffraction mode and b) imaging mode [105]..................51

Figure 2.4. Diagram shows signal transmission system in TEM. 53

Figure 2.5. Load displacement plots show different material responses (different properties) during the indentation process: a) Elastic, b) brittle, c) ductile, d) phase transform, e) cracking, f) creep [106]. 54

Figure 2.6. a) Schematic diagram illustrates indentation with standard spherical indenter and related parameters from measurements. b) Load displacement plot is resulted from the indentation [106]. 55

Figure 2.7. Schematic diagram illustrates the experimental set-up for *in situ* nanoindentation. 58

Figure 2.8. Three major component of *in situ* TEM nanoindentation system is decribed: a) *in situ* nanoindentation holder, b) enlarged image of front piece of the holder with TEM specimen loaded, c) control system and computer...59

Figure 2.9. Graphical user interface (GUI) program shows a) main control window and b) motion control window. The motion control can be performed based on c) the specimen movements 62

Figure 2.10. A schematic diagram illustrating projection image of the nanoindenter tip along cross-sectioned view. 65

Figure 2.11. A schematic diagram illustrates alignment of TEM specimen and nanoindenter tip, including the positions of the specimen, the electron beam, and the (conical) nanoindenter tip and the specimen moving direction [108, 109]. 66

Figure 2.12. Schematic diagram of X-ray spectrometer [110]. 67

Figure 2.13. Plots show effect of particle size on the peak width [110]. 68

Figure 2.14. Plots describe the effect of lattice strain on the peak width, intensity and position [111]. 70

Figure 2.15. Schematic diagram illustrates the laser physical vapor deposition system [113]. 73

Figure 2.16. Schematic diagram illustrates different steps of laser target interactions during laser pulse along time variation (ns) [114]. 75

Figure 2.17. Schematic diagram shows presentation of different phases during the interaction of laser beam with the target surface [114]. 79

Figure 3.1. A schematic diagram illustrates *in situ* nanoindentation experimental setup, including the sample, electron beam and naoindenter tip (a conical-shape tip) positions, and sample moving direction. 86

Figure 3.2. a) Low magnification TEM image and b) enlarged image of a specimen cut from the compressive region. c) Low magnification TEM image and d) enlarged image for a specimen cut from the shear region. Insert shows a SPS processed AZM bulk sample where “a” and “b” regions were under shear and compressive stress, respectively, during SPS process. e) Grain size distribution of Al_2O_3 and $MgAl_2O_4$, and ZrO_2 grains (AZM) shows a clear bi-modal distribution. 88

Figure 3.3. EDX mapping indicates a hexagonal $MgAl_2O_4$ grain is surrounded by small YSZ grains. Grain boundaries are quite clean and obvious without any obvious grain boundary intermixing. 89

Figure 3.4. a) Force-displacement and b) force-time plots show elastic deformation. A series of movie frames shows an elastic deformation regime with a detailed analysis in grain boundary activities shown in: c) before indentation; d) during loading; e) at maximum load; f) after indentation, and the schematic comparison for; g) between before indentation and right before the maximum load and h) between before and after

indentation. (Based on instrument specifications, the estimated measurement error of force is ± 5%.) 90

Figure 3.5. a) Force-displacement and b) force-time plots show a clear step and the corresponding TEM images at point a and point b. This clearly indicates a plastic deformation regime resulted by grain rotation and realignment. (Based on instrument specifications, the estimated measurement error of force is ± 5%.) 93

Figure 3.6. During indentation obvious grain rotation, grain-boundary sliding and plastic deformation were observed. A detailed grain boundary study has been performed to analyze the grain activities during deformation as shown in: a) before indentation; b) during loading; c) during unloading; d) after indentation, and schematic comparison for; e) between before indentation and after the maximum load and f) between before and after indentation. 96

Figure 4.1. A schematic diagram describes the two different indentation directions (indentations have been performed on parallel with and perpendicular to the twin interfaces). The inset plan-view TEM image shows that YBCO twin interfaces have two orientations orthogonal to each other. 104

Figure 4.2. A schematic diagram illustrating the *in situ* nanoindentation experimental setup, including the positions of sample, the electron beam and the (conical) naoindenter tip and sample moving direction. 107

Figure 4.3. a) For the conventional indentation on YBCO (110) plane, hardness measurements are plotted along different indentation depths and different indentation positions from the interface between the film and the substrate. b) After indentation on YBCO (001) plane with different thicknesses, various hardness values are plotted relative to different film thickness. Insets illustrate different indentation directions with regard to film structure. 109

Figure 4.4. Two force-displacement plots are compared for indentation on YBCO (110) plane (solid symbols) and indentation on YBCO (001) plane (open symbols). Insets illustrate different indentation directions along film. (Based on instrument specifications, the estimated measurement error of force is ± 5%.) 111

Figure 4.5. A series of movie frames during indentation on YBCO (001) plane is shown in a) before indentation, b) during loading, c) near maximum load, and d) after unloading. 113

Figure 4.6. After indentation on YBCO (110) planes, the corresponding movie frames are shown a) before indentation, b) during loading, c) at maximum load, and d) after unloading. 115

Figure 4.7. During indenting on YBCO (110) plane, obvious deformation of twin structures was observed. A series of movie frames shows the deformation region with a detailed analysis a)-b) during loading and c)-f) during unloading. 117

Figure 4.8. A detailed study on deformation mechanisms was carried out by correlating the force-displacement plot with the movie snapshots for indenting on YBCO (110) plane. The movie snapshots are a) before indentation, b) and c) during loading, d) right before maximum load, e) during unloading, and f) after unloading. The corresponding image letters are labelled on h) force-displacement and g) force-time plots. (Based on instrument specifications, the estimated measurement error of force is ± 5%.) 119

Figure 5.1. a) TEM image shows the area where *in situ* nanoindentation experiments were conducted. It shows very obvious grain and twin structures. From the top to bottom, grains, G2 and G1, and twin, T1, are marked. The arrows point the boundaries between G1, G2 and T1. The inserted SAD diffraction patterns were taken from the area of b) grain, G1, c) twin, T1, and d) grain, G2. 126

Figure 5.2. Three sets of movie frames during indentation on nc nickel are shown in a1) before and a2) after yield point during the first cycle; b1) before and b2) after yield point during the second cycle; and c1) before and c2) after yield point during the third cycle. 127

Figure 5.3. a) force-displacement plot was measured during the first *in situ* nanoindentation cycle. During the second cycle, b) force-displacement plot show the yield point increases compared to that in the first cycle. Finally, c) force-displacement plot was measured during the third cycle...129

Figure 5.4. Three force-displacement plots only with the loading regime show the nature of work hardening after sequential indentation. Increment of the force at the yield point from ~ 4.9 to 7.0 μN during the three loading cycles is shown. A small regime of softening during the third cycle is observed due to the dislocations exhausted in G1. 130

Figure 5.5. During the first indentation cycle, evident activity of dislocations (mainly screw or mixed dislocations) at the twin boundary was observed with formation of L-C lock. a) A snap shot taken shows the area of

interest marked by a white box near TB1. And enlarged series of movie frames show the interaction between dislocations and twin boundary b) at yield point and c-h) after yield point, with the corresponding i) force-displacement plot. 131

Figure 5.6. Schematic diagrams illustrate the interaction of L-C locks with twin boundaries from series of movie snap shot in Figure 5.5. a) Two full dislocations, (possibly screw or mixed dislocations), A_0 and B, on different set of {111} planes intercept at TB1. b) As dislocation A_0 glides toward dislocation B, an L-C lock is formed at the twin boundary. c) Dislocation A_0 dissociates into two partial dislocations, A_1 and A_2 as separated by ~15 nm. d) As the separation is constricted to ~4.5 nm, another dislocation A_3 is emitted from the dislocation A_1. 134

Figure 5.7. a) A snap shot taken during the second indentation cycle shows the area of interest marked by a white box near TB1. And enlarged series of movie frames show interaction between two specific dislocations, A_0 and B (likely to be screw or mixed dislocations), resulting in the transmission from L-C locks across twin boundaries, with a detailed analysis as shown in b), c) and d) before yield point and e), f), g) and h) after yield point, with the corresponding i) force-displacement plot. 136

Figure 5.8. Schematic diagrams illustrate process of dislocation transmission across TB1 from series of movie snap shot in Figure 5.7. a) Two full dislocations, A_0 and B, on different set of {111} planes form an L-C lock at the twin boundary. b) Dislocation A_0 dissociates into two partial dislocations, A_1 and A_2. Meanwhile, c) dislocation B penetrates through the twin boundary and glides on the (100) plane in T1 as the dislocation B' as released from the back stress at the L-C lock. d) Dislocation B completely penetrates through the twin boundary. Then, dislocation A_1 and A_2 also pass through the twin boundary. 137

Figure 6.1. (a) XRD $\theta \sim 2\theta$ scans of AZO single layer films grown under different oxygen pressures: 250 mTorr, 100 mTorr, 50 mTorr and vacuum, and (b) XRD pattern of a bilayer grown at vacuum and 250 mTorr sequentially. Inset in b is the enlarged ZnO (0002) peak showing an obvious peak splitting for the bi-layers in the sample 144

Figure 6.2. Cross-sectional TEM micrographs show a nanorod structure of AZO single layer epitaxially grown on sapphire substrate at oxygen pressures of (a) 250 mTorr (b) 100 mTorr while continuous layers grow at oxygen pressures of (c) 50 mTorr and (d) Vacuum. 145

Figure 6.3. A cross-sectional TEM micrograph shows AZO bilayer epitaxially grown on sapphire substrate with sequential deposition at oxygen pressures of vacuum and 250 mTorr. The first AZO layer is grown with uniform layer structure under vacuum. The second layer is structured with nanorods under oxygen pressure of 250 mTorr. 147

Figure 6.4. A plot of out-of-plane d-spacing change as a function of oxygen pressure. As oxygen pressure increases, (a) in-plane d-spacing increases while (b) out-of-plane d-spacing decreases...148

Figure 6.5. AFM images of AZO films grown at oxygen pressures of (a) 250 mTorr, (b) 50 mTorr, (c) vacuum and (d) bilayer of 250 mTorr and vacuum. SEM images of AZO films grown at oxygen pressures of e) 250 mTorr and f) bilayer of 250 mTorr and vacuum. Both the single layers grown at 250 mTorr and the bilayer have high surface roughness with nanorods. Films grown at low pressure regime (50 mTorr and vacuum) have a smooth film surface. 149

Figure 6.6. Line scans ((a) and (c)) and 3D surface plots ((b) and (d)) for single layer deposited under 250 mTorr ((a) and (b)) and bilayer AZO film ((c) and (d)). The bilayer film shows a more ordered nanorod distribution than the single layer deposited under 250 mTorr......................................152

Figure 6.7. Optical transmittance spectra for single layers grown under different oxygen pressures at 250 mTorr, 100 mTorr, 50 mTorr and vacuum. The spectra for film grown at 50 mTorr and vacuum show a sharp absorption edge; instead, wider absorption edges are found with spectra for film grown at 250 and 100 mTorr..154

Figure 7.1. (a) XRD $\theta \sim 2\theta$ scans of AZO single layer films grown on α-Al$_2$O$_3$ ($01\bar{1}2$) (r-cut) substrate under 33.3 Pa oxygen pressure and vacuum, and (b) XRD pattern of a bilayer films grown at vacuum and 33.3 Pa sequentially on α-Al$_2$O$_3$ ($01\bar{1}2$) (r-cut) and at 3.3 and 33.3 Pa on (0001) (c-cut) substrates. 161

Figure 7.2. Cross-sectional TEM micrographs show the AZO single layers epitaxially grown on α-Al$_2$O$_3$ ($01\bar{1}2$) (r-cut) substrate at the oxygen pressure of (a) 33.3 Pa and (b) vacuum, and the AZO bilayer grown with sequential deposition at oxygen pressures of vacuum and 33.3 Pa on (c) α-Al$_2$O$_3$ ($01\bar{1}2$) (r-cut) substrate and 3.3 and 33.3 Pa on (d) α-Al$_2$O$_3$ (0001) (c-cut) substrate..162

Figure 7.3. Schematic diagrams describe the orientation relationship between the film and the substrate for (a) single layer and (b) bilayer AZO films grown on α-Al_2O_3 ($01\bar{1}2$) (r-cut) substrate. 164

Figure 7.4. Plots show variation in d-spacing along AZO [0002] and $[11\bar{2}0]$ as a function of oxygen pressure and effect of different substrates. 165

Figure 7.5. HRTEM images show the single layer AZO films grown on α-Al_2O_3 ($01\bar{1}2$) (r-cut) substrate. (a) is for the film/substrate interface area and (b) is the area near the tilted grain boundary, both for 33.3 Pa sample. (c) is the film/substrate interface area for the vacuum sample, and (d) is the film/substrate interface region for the bilayer film grown on α-Al_2O_3 (0001) (c-cut) substrate. The insets are corresponding FFT diffraction patterns for each image. 166

Figure 7.6. HRTEM images from the different areas of bilayer deposited on α-Al_2O_3 ($01\bar{1}2$) (r-cut) substrate under different oxygen pressures: (a) the vacuum layer and (b) the interface area between the vacuum and 33.3 Pa layers, and (c) the 33.3 Pa layer. The insets are the corresponding FFT diffraction patterns. The in-plane d-spacing variation is calculated on the areas along the film growth direction and plotted in (d), i.e., i) NL(B): the area right above the film/substrate interface, ii) NL(T): the area of film right below the nanolayer/nano-columns interface, iii) NC(B): the area right above the nanolayer/nano-columns interface and iv) NC(T): the area from the tip portion of the nano-columns. 167

Figure 7.7. SEM images show the different surface morphologies of AZO films grown at (a) 33.3 Pa, (b) vacuum and (c) the bilayer of vacuum and 33.3 Pa on r-cut substrate, and (d) the bilayer of 3.3 and 33.3 Pa on c-cut substrate. 171

Figure 7.8. Plots show the electrical resistivity values of AZO films grown at a) 33.3 Pa and b) vacuum on r-cut substrate. The values are measured along the variation of the temperature in the range of 200~400K. 172

Figure 8.1. A schematic diagram illustrates *in situ* nanoindentation experimental setup, including the sample, electron beam and naoindenter tip (a wedge shape tip) positions, and sample moving direction. 179

Figure 8.2. (a) Cross-sectional TEM micrograph shows the AZO single layer epitaxially grown on α-Al_2O_3 (0001) (c-cut) substrate at the oxygen pressure of 250mTorr. (b) Schematic diagrams describe two different types of nanorod structures with different ratios of width/length (*w/l*), e.g. (i) for type I size of length is much larger than that of width with *w/l*

ratio of ~0.51 and (ii) for type II size of width and length are on similar range with *w/l* ratio of ~0.88, selected for *in situ* TEM nanoindetation. 181

Figure 8.3. A detailed study of deformation mechanism was carried out by correlating the force–displacement plot with the movie snapshots for indentation on type I AZO nanorod. A set of movie frames during indentation on AZO (0001) is shown in (a) before indentation, (b), (c) and (d) during loading process, (e) right after maximum load, and (f) after indentation. The corresponding image letters are labelled on the (h) force–displacement and (g) force–time plots. (Based on instrument specifications, the estimated measurement error of force is ±5 %.) 184

Figure 8.4. During indentation on type II AZO nanorod, a set of movie frames was captured in (a) before indentation, (b), (c), (d) and (e) during loading process, (f) after indentation. The corresponding image letters are labelled on the (h) force–displacement and (g) force–time plots. (Based on instrument specifications, the estimated measurement error of force is ±5 %.) 185

LIST OF TABLES

Page

Table 1.1. Recent research progress with *in- situ* TEM characterization on various nanomaterials. 37

Table 1.1. Continued 38

Table 2.1. Calibrated indenter sensor data 61

Table 6.1. List of samples and electrical resistivity values. 155

Table 7.1. List of the samples and their electrical resistivity values. 174

CHAPTER I

INTRODUCTION

1.1. Overview

Emergence of the nanomaterials has led to remarkable developments in the field of nanotechnology owing to their extraordinary properties under their reduced sizes in nanoscale from micro or mesoscale. Significant advances in the area of microelectronic devices have been achieved by the discoveries of new nanomaterials and new nanoscale processing techniques. For example, every two years the number of transistors in an integrated circuit is supposed to be doubled based on Moore's law. Maintaining the law was largely contributed by nanotechnology as indicated by the diagram in figure 1.1 [1].

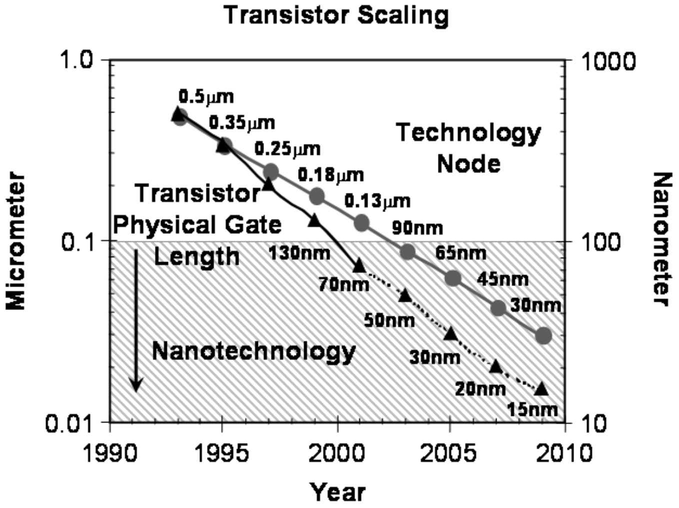

Figure 1.1. Reduction of transistor size based on physical gate length under Moore's Law [1].

Especially, recently numerous new properties in nanostructured metals and ceramics have been introduced. The field of nanostructured materials has brought significant research interest to develop more advanced materials to overcome the limitation of materials' intrinsic properties. For example, with the recent introduction of nanostrctured metals, it is possible to have ultrahigh strength and high ductility of the metals. For instance, as nanostructured copper employing nanotwined structures shows 10 times increased tensile strength compared to the coarse grained copper sample [2]. Remarkably, it has been noticed that the yield strength has been significantly increased with the reduction of the twin thickness up to 15 nm, which obeys the Hall-Petch relationship [3]. Additionally, as nanocrystalline copper composed of micro sized grains in matrix of the nanocrystalline grain, the bimodal grain size distribution enhances the high tensile ductility with significant elongation rate [4]. In the case of nanostructured ceramic, with recent development of new structures in nanocomposite ceramic materials by incorporating nanosize dispersions within the matrix grains and at the grain boundaries [5, 6], mechanical property of ceramic material has been significantly enhanced. Especially, based on recent research finding, it is possible for the nanocrystalline ceramic to have plastic deformation based on the grain boundary sliding and grain rotation while the grain boundary interacting with dislocations [7-9]. The discoveries of new nanomaterials such as carbon nanotubes, nanowires and graphene have shown large potential impacts in the developments of future microelectronic devices [10-12]. Moreover, with the recent advances of high resolution imaging and physical property measurement techniques, discovering new nanomaterials with further enhanced physical properties is possible [13-15]. Particularly, because of the development of the high resolution of electron microscopy as companied with energy dispersive x-ray spectroscopy, it is possible to analysis the lattice structure of a material and composition of constituent at atomic scale.

However, despite the fact that significant advance has been made in the characterization techniques, most of the research still focus on conventional characterization methods such as *ex situ* nanoindentation, four point probe system, and etc.. Especially, for the measurement of mechanical property, much work still heavily relies on the *ex situ* nanoindentation method. Using scanning electron microscopy (SEM) or atomic force microscopy (AFM) after *ex situ* nanoindentation, the surface of deformed area in the materials can be analyzed. Furthermore, in order to fully understand the deformation mechanism of the materials during indentation, it is necessary to study the microstructure evolution of the materials under the TEM column. However, it might be difficult for the preparation of the TEM specimen, maintaining the original deformed condition. Therefore, for the post-analysis data with TEM, SEM and AFM, it sometimes can be in doubt whether deformed condition observed in the microstructural analysis can be directly corresponded to that during the deformation processing. Thus, it is lack of the reliability for a specific phenomenon observed from the post-mortem data to be generalized. In order to overcome the obstacle of the post-mortem observation, *in situ* TEM nanoindentation system has been developed at Lawrence Berkeley National Laboratory in 1997 [16] for more dynamic and real-time observation which brings direct correlation between property and structural evolution.

1.2. Nanomaterials

Nanomaterials are usually defined as materials whose structural morphologies become nanometer scale in the range of 1~100 nm. And such morphologies can be differentiated with different structures in different dimensions. For example, as a zero dimensional nanostructured material, nanoparticle or nanocluster can be introduced, whose size of diameter is on nanometer scale [17]. And nanotube, nanowire or nanofiber can be categorized to one dimensional nanostructured material with nanometer sized width [18]. Next, graphene nanosheet or thin film can be explained as a two dimensional nanostructured material with nanosized thickness [12, 19]. And finally, bulk nanostructed material can be exampled as a three dimensional nanostructured material, in which usually grain size is less than 100 nm [20]. Therefore, with such small scale of structure, minimum variation of atomic arrangement during the synthesis can give large impact on the property. Generally, nanomaterial can be processed on either bottom-up or top-down processing method. For example, lithography etching belongs to top-down methods, under which radiation such as ultraviolet light or X-ray can design the nanostructure form as bombarding the top surface of the material [21]. And several thin film processing methods such as pulsed laser deposition (PLD), sputtering, molecular beam epitaxy method, and etc. can be introduced as bottom-up processing method on which adatoms evaporated from a target material lie down on a substrate and grow up from bottom to top to form a nanomaterial.

1.2.1. Bulk nanostructured materials

1.2.1.1. Material Processing

Bulk nanostructured materials have brought a lot of attention due to their excellent performance and capability of their unique structures, which can be useful for broad range of applications [22]. Additionally, as integrating with multi-properties from mix of different constituents, nanostructured materials can show outstanding combination of physical properties [23-25]. In order to maintain such potential characteristics of nanostructured materials, most challenging part to demonstrate the materials is to control the structural morphology with small-size grains during the sintering processing. Currently, there are several processing methods to consolidate materials, i.e. spark plasma sintering, pulsed electric current sintering, electric pulse assisted consolidation, etc. [26-28]. Among them, most broadly used technique is the spark plasma sintering (SPS) system because of its more efficient sintering processing approach. The processing of sintering powder within SPS is composed of three major factors which are pressure, heat and holding time. Once the powder of the material loaded in the system, external pressure has been applied by punch along uniaxial direction. Usually the rearrangement, diffusion and finally growth of the particle during the sintering process can be controlled by the pressure and holding time. Figure 1.2a illustrates the influence of the pressure on the density of the ZrO_2 while it was sintering at1200 °C under holding time of 5mins [29]. It shows clearly that the overall density of the ZrO_2 is logarithmically proportional to the applied pressure. Similarly, in figure 1.2b size of grain of alumina (Al_2O_3) can be significantly affected by the holding time which controls the duration of inter-diffusion between grains [30].

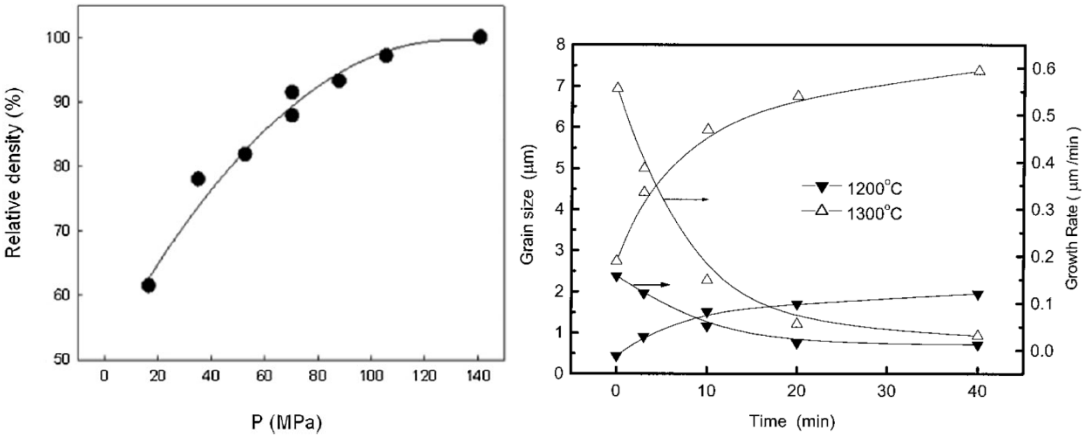

Figure 1.2. a) Influence of the pressure on the density of the ZrO_2 under 1200 °C with holding time of 5mins, b) effect of size of grain of alumina (Al_2O_3) by the holding time [29, 30].

Usually during the processing, the heat (Joule heating) can be applied with the sparked discharge caused internally between materials induced by pulsed DC voltage and current [31]. Therefore, it can ramp up significantly as fast as 1000K/min. Then material can be sintered at a lower sintering temperature and for a shorter time than other conventional sintering techniques. During such rapid sintering process, increasing the heating rate can shorten the period of surface diffusion; hence, growth of the grain can be limited and material shows reduced size of grain [30].

1.2.1.2. Nanostructured ceramic

Ceramic material is usually very hard and brittle under external force applied due to its directional ionic or covalent bonding. Thus, owing to the low fracture toughness and poor machinability, its industrial applications are limited. However, as new types of the ceramic material introduced, it is possible to overcome the poor mechanical property of the material. Ever since last decade, a lot of research efforts have been given to enhance the strength and fracture toughness of ceramic materials. And the pioneering work by Niihara implies that as nano-sized particle incorporating within the matrix grains and at the grain boundaries, the mechanical properties can be significantly enhanced at both room temperature and high temperatures [5]. For example, more than 50% increase of the toughness of ceramic material has been reported primarily by crack deflection by nano-sized particle within matrix grains.

It has been demonstrated that there could be three different types of nanostructured ceramic materials as composite materials (figure 1.3) [6]. The first type (type I) is the two-phased nanostructured material in figure 1.3a. And the second type (type II) is nanostructured material with nano-sized particle dispersed within matrix grains in figure 1.3b, d and e. Finally the third type (type III) is two-phased micro/nanostructured material in figure 1.3c. For the second type, as the nano-sized particle reinforced the matrix grains, the nanostructured material can be divided into three more different groups (figure 1.3b, d and e). First, the nanoparticles have been incorporated along the grain boundary of the matrix grains, which is known as intergranular structure (figure 1.3d). Next group of structure is the intragranular structure, which is formed as nanoparticles dispersed in interior of the matrix grains (figure 1.3e). And last group of the type II is the mixed form of the first and second groups of the structures in type II material (figure 1.3b). Each different nanostructure in the material can be benefited with achievement of increase fracture toughness as enhancing the plasticity during the deformation processing. During the deformation of ceramics, major microstructural evolution has occurred by grain and grain boundary activities. And depending on the different nanostructures aforementioned and size of grain, the deformation behavior of the material could be different. Usually for the type I, deformation behavior can be dominated by grain boundary sliding which can enhance the superplasticity. For the type II, nanoparticles dispersed along the grain boundary from the first group of the nanostructured material can play to pin the grain boundary; therefore, it can enhance the threshold stress which is the maximum stress to produce the creep, based on the relationship of $\sigma_{\mathrm{thres}} \sim \mathrm{Gb/D}$, where G is shear modulus, b is burgers vector and D is the spacing between dispersed particles along grain boundary. Whereas, for the second group of the type II nanostructured material, once the size of the dispersed particle in the matrix grain becomes small enough compared to the threshold size to induce the crack propagation, deformation behavior of the material may show the enhancement of the property with crack reflection by the particles. Therefore, with such specialties given to different types of nanostructured ceramic materials, during the deformation, finally, the materials can show the significant enhancement of the toughness, compared to the conventional ceramic materials.

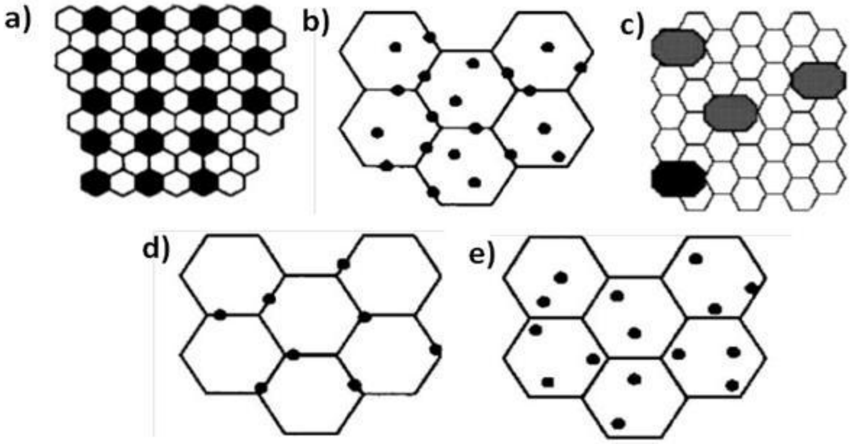

Figure 1.3. Schematic diagram showing different types of nanostructured ceramic materials: a) two-phased nanocomposite material b) inter/intra-granular nanocomposite material c) micro/nanostructured material d) inter-granular nanocomposite material and e) intra-granular nanocomposite material [6].

1.2.1.3. Nanostructured Metal

Different from the ceramics which are usually hard and brittle, metallic systems are usually ductile due to their metallic bonds in which free electrons glue non-valence electrons and nucleus of atoms. Therefore, conventionally metal shows relatively low mechanical strength. However, with recent demonstration of nanostructured metals, it has shown significant increase of the mechanical property. The plastic deformation of the metal is mainly driven by the dislocation activities. Therefore, retarding the dislocation motions during the deformation processing can be the key factor to increase the yield strength. Usually at the temperature less than half of the material melting point, mobile dislocation can be hindered by the grain boundaries [32]. Therefore, based on

Hall-Petch relationship in equation (1.1), it has been explained that slip path of the dislocation can be limited by frequent presence of misaligned slip plane along the grains which is due to reduction of grain size; thus the yield stress of material is inversely proportional to size of grains.

$$\sigma_y = \sigma_0 + \frac{k}{\sqrt{d}} \qquad (1.1),$$

where σ_y is the yield stress, σ_0 is a fractional stress needed for initial movement of the dislocation, k is the strengthening coefficient and d is the size of the grain. In order to materialize the relationship of size-dependent strengthening, nanostructured metals have employed the nano-sized grain or twin structure. Figure 1.4 shows clearly the increase of the stress as the grain sizes of nanocrystalline copper decrease from ~50 to ~12 nm [33]. Under the stress applied, a maximum number of dislocations could be piled up at the grain boundary at around 2.5 ~ 3% of the strain (Figure 1.4a). However, after the maximum stress as the dislocations moved in the interior of grains, the curve shows the plastic deformation regime with decreasing stress. Figure 1.4b also shows obviously variation of yield stress of the materials highly depending on the grain size. Although reverse Hall-Petch relationship has been observed with grain size less than 12 nm, which might be occurred as the grain size is significantly reduced more than stable distance maintaining the elastic interaction between dislocations [34, 35], in the range of 15 ~ 50 nm of grain size change of the yield stress well obeys Hall-Petch relationship.

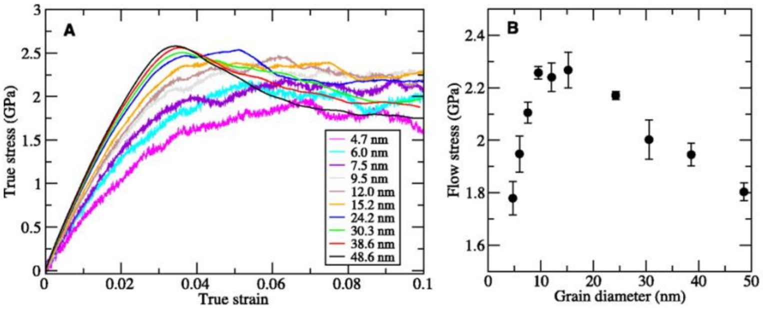

Figure 1.4. Plots show clearly the increase of the stress as the grain sizes of nanocrystalline copper decreased from ~ 50 to ~12 nm [33].

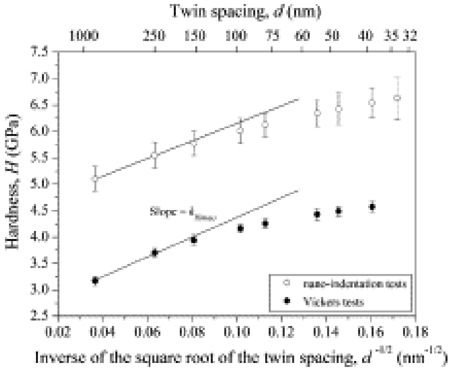

Figure 1.5. Plot shows increment of hardness of nickel based alloys along reduction of size of the twin spacing during the indentation test [36].

Additional to grain size dependent hardening effect, nickel based alloys employing the nanotwined structures show comparable result depending on different size of the twin spacing during the indentation test (figure 1.5) [36]. In the report, it has been suggested that nonlinearly increase hardness with the reduction of twin spacing could be from the different deformation mechanisms through the different the twin spacing. The main driving force to enhance the hardness is the increasing stress acting between the dislocations as the dislocation density is getting higher when the twin spacing becomes greater than 150 nm. On the other hand, as the twin spacing gets smaller than 100 nm, the hardness can be determined by the amount of the energy needed for expansion of dislocation through the glide planes. Therefore, it can be explained by the suggestion that the stress flowed during hardening highly depends on the dislocation density. And in this term, the Hall-Petch relationship can be rewritten based on Taylor relationship in equation (1.2)

$$\sigma_y = \sigma_0 + \alpha M G b \sqrt{\rho} \qquad (1.2),$$

where the α is the geometrical constant, M is Taylor factor, G is the shear modulus, b is the magnitude of burgers vector and ρ is the density of dislocations involved in the increase of yield strength. Therefore, in the nanostructured metal, how to control the dislocation activity could be the main key factor to improve the property of the material system.

1.2.2. Thin film materials

Although a lot of ceramic and metal are employed by various applications in bulk form, thin film material has been introduced with several advantages over the bulk material owing to its flexibility in processing nanostructured metals and ceramics. First of all, as the thin film material has increased ratio of surface area to volume, it can cover the large surface area. Usually, thin film can be deposited with thickness in nano or micro-scale. Therefore, contrast to the bulk material which has relatively small ratio of surface area to volume with thickness on macro scale, small amount of materials can be used during the processing of the thin films. Another reason for the preferred thin film material is because it is usually processed by different deposition techniques which could sometimes be simpler than the approaches to manufacture the bulk materials. For example, while manufacturing solar cell modules based on bulk silicon solar cell, bulk silicon should be processed with about nine different steps while the thin film solar cell only has about four steps required. Especially, the process to make different layers i.e. n-type and p-type layers, on the substrate for the bulk silicon solar cell shows at least four steps required, including diffusion of phosphorus, screen printing for metal contact, wiring the contact, arraying on glass substrate. However, during the thin film solar cell process, these four steps can be conducted only with a thin film deposition process. Moreover, depending on the deposition parameters, the property of thin film material can be more easily variable and reproducible. Finally, thin film material can be lighter, smaller and more flexible potentially with its lower cost.

1.2.2.1. Processing of thin film materials

It has been mentioned in previous section that the property of the thin film can be easily changeable with different parameters during the process of the film. It means that for different film functionalities, different deposition methods with various parameters are required. Therefore, over the past decade, various deposition methods have been introduced and extensively used for the industrial applications. Currently, the thin film processing methods can be divided into physical vapor deposition (PVD) and chemical vapor deposition (CVD) methods. Usually, these two deposition methods can be differentiated with its gas regime (figure 1.6) [37].

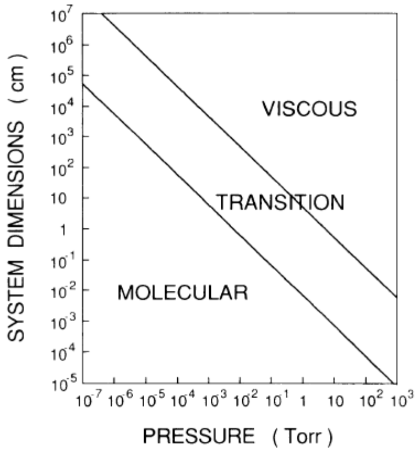

Figure 1.6. Diagram illustrates the different gas flow regimes based on variation of the system dimensions and pressure [37].

PVD can be performed under the molecular flow regime with large mean free path of the adatoms under the low gas pressure. Therefore, under the PVD, the film is usually deposited as the adatoms nucleated on the substrate directly from target material through the gas phase by evaporation or impact of collision. Among PVD methods, currently most widely used techniques are evaporation, magnetron sputtering, electrodeposition etc.. First, for the evaporation method, it can be divided into thermal and electron beam evaporations depending on the heating source. While thermally heating source used in the thermal evaporation process, during e-beam evaporation process heat source is from the tungsten wire which generates the resistive heat. During the evaporation process usually the film is grown by the evaporation rate given by equation 1.3 which can be controlled by heating energy and vapor pressure.

$$\Phi_e = \frac{\alpha_e N_A (P_e - P_h)}{\sqrt{2\pi MRT}} \quad (1.3),$$

where α_e is the coefficient of evaporation, N_A is Avogadro's number, P_e is vapor pressure, P_h is hydrostatic pressure, M is molar mass, R is gas constant, T is the temperature. Therefore, under certain temperature, target material can evaporate into the gas atoms and transfer from a heated target to a substrate. In addition to the evaporation process, another PVD process with good film surface coverage is sputtering method. Usually sputtering can be used to grow metal or non-conductive ceramic thin film materials. Basic principle for this method is that as high energy gas ions bombard surface of target, atoms can be removed from the target surface by the interaction with the incident ions. Then the dislodged atoms from the target can fly to the surface of the substrate to be deposited on. Dependent on power sources, there are usually two different sputtering deposition systems, RF magnetron and DC sputtering systems (Figure 1.7).

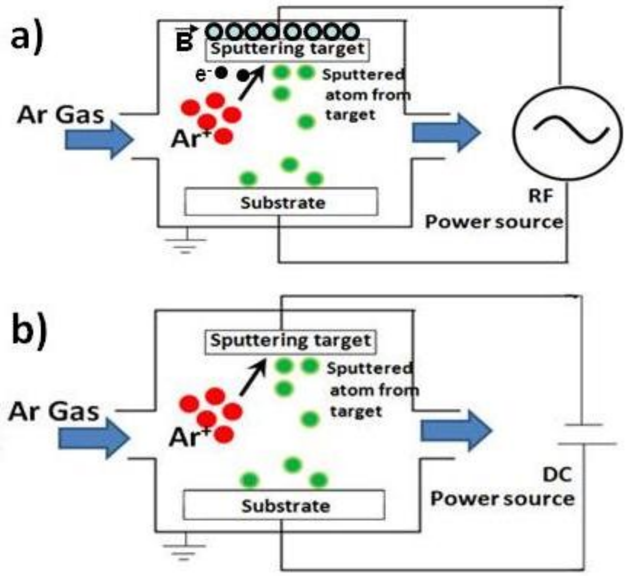

Figure 1.7. Schematic diagrams illustrate a) RF magnetron and b) DC sputtering systems.

Figure 1.7a shows the RF magnetron sputtering system. This system is usually used to deposit non-conductive ceramic materials. Since the ceramic material is not conductive, it requires a force to carry the atoms from the target to the surface of the substrate. This force is usually formed by the magnetic and electric field. On the other hand, with the DC sputtering system the metal samples are usually grown on the substrate (figure 1.7b). Since the metal particles sputtered from the target are conductive, they can fly on the substrate under different potentials formed by the DC power source. Therefore, via this processing method, the thin film can be processed with smooth surface and good surface coverage. Finally, another widely used PVD process is electrochemical deposition. This processing is usually used for deposition of the metal. The processing can be occurred through the electric field applied between anode and cathode plates under which the metal ions (from anode) in the solution bath can be deposited on the substrate material (cathode). Figure 1.8 shows the experiment set up for the electrochemical deposition.

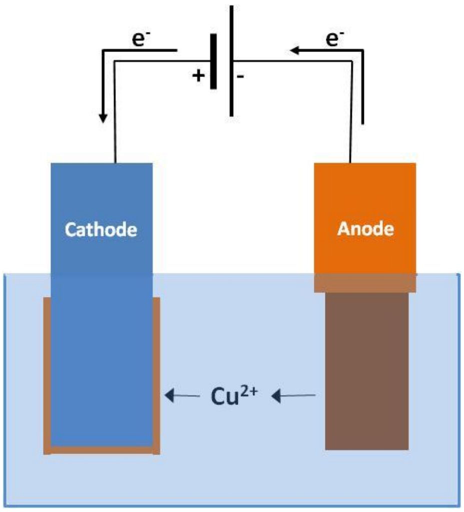

Figure 1.8. Schematic diagram illustrate experiment set up for electrochemical deposition.

For the deposition, both the cathode and anode plates have to be immersed in the solution bath which is electrolyte in which the metal ions can electrically flow. Then as applying the electric field between the anode and cathode plates, the metal elements from the anode plate can be dissolved in solution base with ionized form as losing electrons, e.g. $Cu \rightarrow Cu^{2+} + 2e^{-}$. Then the cation from the anode can be deposited on the cathode substrate through the solution base. Once it attaches on the surface of the cathode, finally, it can be grown as metal form, after gaining electrons which transfer from anode plate, $Cu \leftarrow Cu^{2+} + 2e^{-}$. With such simple equipment setting for the deposition process, it is inexpensive. Besides these processing methods, there are several other PVD methods such as pulsed laser deposition (PLD) and molecular beam epitaxy (MBE) methods. And these methods also show noticeable advantages over other deposition systems. For example, during PLD processing, the film can be deposited stoichiometrically with high energy of pulsed laser, and under MBE system, high quality epitaxial films with good interface and surface morphology due to large mean free path of adatoms can be processed.

In contrast to such simple process of the PVD, during CVD processing, the thin film is deposited by gas chemical reaction near the surface of the substrate through several steps. Therefore, it can have the better film surface coverage and higher throughput than that from PVD. Usually, the CVD deposition can be performed in viscous flow regime in figure 1.6. Therefore, target gas atoms have huge collisions during the process. Figure 1.9 shows the basic steps for the CVD process.

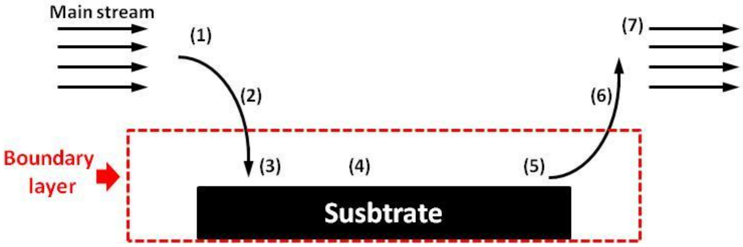

Figure 1.9. Schematic diagram illustrates the CVD process under the laminar flow based on the following steps: 1) transport of reactant by the convention of main stream, 2) diffuse of the reactant on the surface of substrate, 3) absorption of reactant, 4) surface process, 5) desorption of by-product, 6) diffuse to the main stream, 7) transport of the by-product.

While the reactants transport through the main stream, as it passes over the substrate, it diffuses to the surface of the substrate through the boundary layer. Then, during the surface process, chemical reaction, deposition and surface migration has been carried out. After the process, byproducts are desorbed from the surface of the substrate, and then diffuse into the main stream. The overall growth rate can be decided by step 2~5 in figure 1.9 which is mainly performed within the boundary layer. However, as the target gas atoms being consumed along the susceptor with increasing static boundary layer δ(x), and due to limitation of deposition by the mass transfer though the boundary layer, the film growth rate will decrease moving through the susceptor. Therefore, susceptor with substrate should be tilted to increase the gas flow rate.

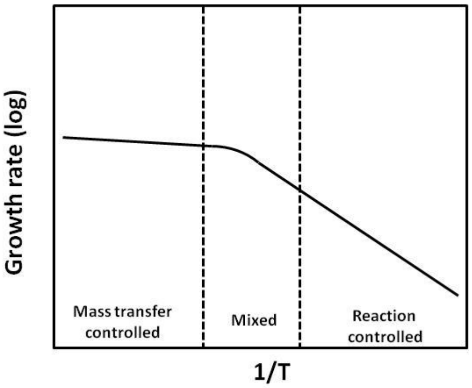

Figure 1.10. Plot shows growth rate of film in mass transfer and reaction regimes based on deposition temperature variation during CVD process.

Usually, the deposition rate of the film during the CVD can be explained based on the growth velocity in mass transfer regime and reaction regime depending on the deposition temperature (Figure 1.10). Under high temperature, chemical surface reaction rate goes beyond the mass transfer rate; thus mass transfer can control the growth rate (equation 1.4 and 1.5). And due to h_G which is insensitive to the temperature while k_S is sensitive, relatively constant deposition rate has been show in this regime.

$$v = \frac{k_S h_G}{k_S + h_G} \frac{C_T}{N} N \qquad (1.4),$$

$$v = k_S \frac{C_T}{N} N \quad \text{when } k_S \ll h_G \qquad (1.5),$$

$$v = h_G \frac{C_T}{N} N \quad \text{when } k_S \gg h_G \qquad (1.6),$$

where v is the growth rate of the film, k_S is the chemical surface reaction rate, h_G is the mass transfer coefficient, C_T is the concentration of all molecules in gas phase, N is atomic density of the film and Y is the partial pressure of the incorporating species. However, under low temperature, the mass transfer rate can exceed the surface reaction rate. Therefore, based on the equation (1.4) and (1.6), the deposition rate will be determined by the surface reaction.

1.2.2.2. Growth mechanism of thin film materials

Once the adatoms from target material lie on the substrate, they diffuse and find right position to reduce the surface energy and nucleate. During the nucleation of solid phase, the mechanism should be considered in terms of the change of free energy, ΔG. Equation 1.7 shows the change of the total free energy during the nucleation of the solid phase as spherical shape in the liquid phase in Figure 1.11a.

$$\Delta G = \frac{4}{3}\pi r^3 \Delta G_v + 4\pi r^2 \gamma \qquad (1.7),$$

Once the particle formed in the liquid phase, the free energy increases until stable state of the nucleation formation exists as the nucleation size exceeds the critical radius of r* (figure 1.11b). And the energy barrier of ΔG* would be overcome. Finally, the thin film can be grown up.

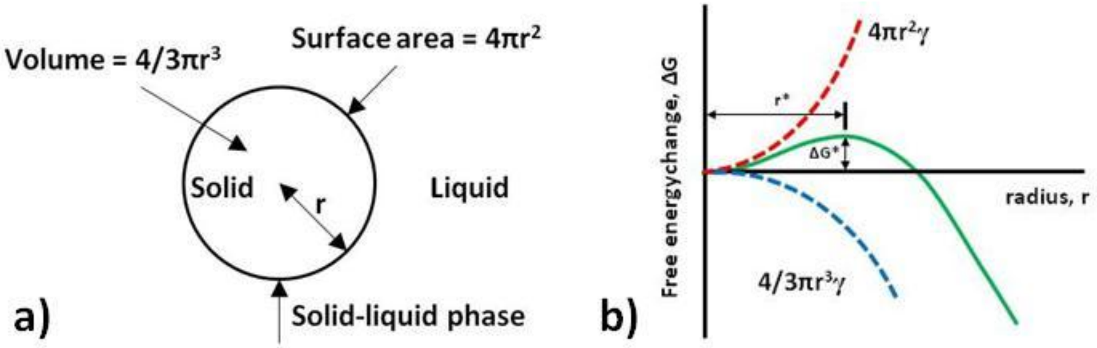

Figure 1.11. a) Schematic diagram illustrates the nucleation of solid particle as spherical formation. And during this process, b) plot shows the variation of the free energy.

Usually, when the films are deposited on the substrate, they are formed on three different growth modes. The first mode is the Frank-Van der Merwe mode which is well known as layer by layer mode. Usually, as the film grown on this mode, the adatoms are widely spread out over the substrate, showing larger growth rate of the film along lateral direction than the vertical one, under which film looks like two-dimensional sheet shape. The second mode is Volmer-Weber mode which is also known as island growth mode. Unlike the first mode, as the film grown on this mode, surface tension between the adatoms of the film is stronger than that between substrate and vapor. Thus, the film can grow more like three-dimensional island shape. Finally, last mode is the mixed case of the first and second modes. The reason why the film should be formed on one of these three growth modes is because as a film grown on a substrate, different surface tensions could be acted between the film and substrate, film and vapor, and substrate and vapor, depending on the kinds of material of the film and substrate (figure 1.12). And as the surface tensions between the film, substrate and vapor driven along lateral direction, it can result in the equation 1.8 which can be used to determine the growth mode of the film.

$$\cos\theta = \frac{\gamma_{sv} - \gamma_{fs}}{\gamma_{fv}} \qquad (1.8)$$

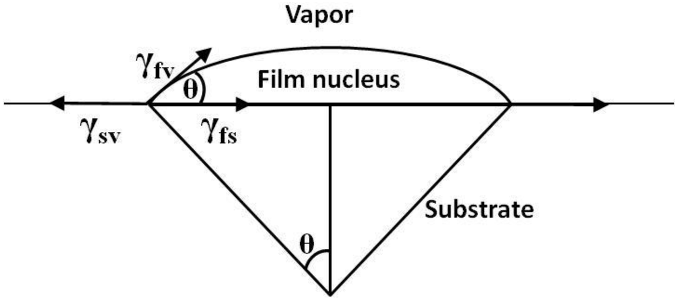

Figure 1.12. Schematic diagram illustrates the different surface tensions acted between the film and substrate, film and vapor, and vapor and substrate while the film nucleated on substrate.

Based on this equation, the first growth mode (layer by layer) can be enhanced as the surface tension between the substrate and vapor exceeds or equal to sum of those between the film and substrate, and the film and vapor (equation 1.9). Usually, when growth of oxide materials on metal substrates, or growth of silicon or germanium film on silicon substrate, the growth of the films can be controlled with this mode.

$\gamma_{sv} \geq \gamma_{fs} + \gamma_{fv}$ for layer by layer growth, (1.9)

$\gamma_{sv} < \gamma_{fs} + \gamma_{fv}$ for island growth, (1.10)

$\gamma_{sv} > \gamma_{fs} + \gamma_{fv}$ for island and layer growth, (1.11)

However, in the reversed case with equation 1.10, the island structure of the film can be formed. And the growth mode of the metal films on oxide materials of the substrate belongs to this mode.

1.3. Material systems studied

1.3.1. Al_2O_3-ZrO_2-$MgAl_2O_4$ ceramic nanocomposites

As starting with Niihara's suggestion of incorporating nanosize dispersions within the matrix grains and at the grain boundaries [5], significant achievement has been made in the field of nanostructured ceramic materials to further enhance the strength and fracture toughness. Especially, recently as Kim et al showed that alumina–zirconia–magnesia spinel (Al_2O_3–ZrO_2–$MgAl_2O_4$, AZM) nanocomposites exhibits high strain rates up to 1 s^{-1} at temperature of 1650 °C due to its unique multiphase structure [20], high strain rate superplasticity (HSRS) with high ductility could be demonstrated by the nanostructured ceramic material, which can be explained by the Mukherjee–Bird–Dorn equation 1.12 as follows.

$$\dot{\varepsilon} = A\frac{D_0 G b}{kT}\left(\frac{b}{d}\right)^p \left(\frac{\sigma}{G}\right)^n e^{-Q/RT} \qquad (1.12)$$

where *G* is the elastic shear modulus, *b* is the Burgers vector, *k* is the Boltzmann's constant, *T* is the absolute temperature, *d* is the grain size, *p* is the grain-size dependence coefficient, *n* is the stress exponent, *Q* is the activation energy, D_0 is the diffusion coefficient and *R* is the gas constant. An alumina zirconia magnesia spinel (Al_2O_3–ZrO_2–$MgAl_2O_4$, AZM) nanocomposite is typically composed of tetragonal zirconium oxide, magnesium aluminate spinel and α-alumina phases. Magnesium aluminate ($MgAl_2O_4$) spinel usually shows high melting point, low thermal expansion coefficient, good corrosion resistance and excellent optical transmission [38-41]. Therefore, it can be employed by various applications [42, 43]. Recently with incorporation with zirconia (ZrO_2), the mechanical property of $MgAl_2O_4$ spinel could be improved. Based on Morita et al's report [44], it has been explained that as 3 mol% Y_2O_3 stabilized tetragonal ZrO_2 mixed with 30 vol% of $MgAl_2O_4$, tensile ductility has been increased more than six times at 1823K, showing the elongation of soft spinel, which provides the evidence of the superplasticity. Especially, as Al_2O_3 becomes rich in $MgAl_2O_4$ spinel, the density of the material could be increased with increase in grain size [45]. Recently, Jiang et al. processed the AZM with 30-40-30 mol% mixture under different steps of procedure, i. e. ball milling, drying, sieving, powder mixture, and spark plasma sintering (SPS) and forming [46]. During the SPS sintering and forming processes, different heating temperature and pressure were applied. First, for sintering process, 63MPa of pressure was applied; then temperature rose up to 600 °C for 3-5 min. After this, the temperature was significantly ramped up to 1150 °C for 2 min and this temperature was maintained for 3 min. During the forming process following the sintering, initially relatively low pressure of 18 MPa was applied and same procedure as the sintering process was repeated. Then pressure was increased up to 105 MPa for ~30 sec. During the forming process, as graphite punch was used, which was composed of two 45° inclined teeth with 4mm between teeth, and 1mm tooth depth, both compressive and shear stress could be applied. Then based on the equation 1.12, under the constant temperature, high strain rate with ~1.4×10^{-2} S^{-1} could be enhanced due to the small grain size. Compared to the structure of as-sintered material, through the forming process, the grain has been significantly grown up to 1μm. This can be possibly induced difference of dissolving elements which move through grain boundary during the grain boundary diffusion under high pressure applied which has been explained by Kim et al. [47].

1.3.2. Nanocrystalline nickel

Since Axel Fredrik Cronstedt classified nickel (Ni) as one of the chemical elements in 1751, this metal has been broadly used due to its unique properties such as high oxidation resistance, thermal conductivity, ferromagnetism, etc. [48-50]. As one of transition metals, it has face centered cubic structure with lattice parameter of 3.52 Å. Nickel is one of room temperature magnetic materials with Curie temperature of 335 °C. More potentially, mixing with cobalt or iron, it has been more widely used as alloy form, as performing high strength, high temperature creep resistance and corrosion resistance. Additionally, with development of processing technique, as the grain size in the metal has been reduced to nano-meter range, mechanically superior performance of the material is expected with grain refinement. Since the size dependent hardening mechanism has demonstrated based on Hall-Patch relation, reduction of the slip length based on decrease in the grain size has been considered as one of key factor to enhance the mechanical property of the metal. Additionally, nanoscale twin structure embedded in the material is also counted to effectively enhance the mechanical property as hindering the dislocation movements. Therefore, to demonstrate such property of the nanocrystalline (nc) nickel, recently various deposition methods have been performed. First, Kumar et al. has conducted electrochemical deposition to grow fully densed nc nickels with mean grain sizes of about 30 nm [51]. In order to explore deformation behavior of nc nickel, cold rolling test, uniaxial compression and nanoindentation tests were conducted as parallel with *in situ* tensile test under TEM column. During the cold rolling test, grain coarsening, round shaped grain boundaries at the triple junction and several clear evidences of dislocation activity such as semi circular shaped contrast and slip traces in the grain were noticed. On the other hand, existence of dislocation in the interior of grain, dislocation array in low angle grain boundary and nanovoid at the triple junction which has crack formation were observed after uniaxial compression test. More interestingly, during the *in situ* tensile test, growth of grain boundary crack and triple junction void, and dislocation emission from the crack tip were noticed, which enhanced the facture. During the test, severe plastic deformation was occurred with separation of grains under increment of load proceeding to necking of a ligament as accompanying with the formation of twin. Finally, surface morphology after fracture showed dimple shaped rupture which was 6~10 times larger than the grain size. Such deformation process can be summarized by following steps. First, under stress increased, dislocations emitted from grain boundary with formation of voids at the boundary and triple junction during the grain boundary sliding, which was possibly caused by the grain boundary shear after the dislocation piled up at the grain boundary [52,53]. Eventually, dimple was nucleated from the void and grain boundary.

Holland et al. also conducted the tensile test to explore deformation behavior of nc nickel with bimodal grain distribution (mixture of 50% of 20 nm and 50% of 200 nm grains, and mixture of 20% of 20 nm and 80% 200 nm grains) processed by the spark plasma sintering (SPS) system [54]. After the test, twin deformation and shear band were mainly observed with which partial dislocation emission by the grain rotation was accompanied. Usually, twin deformation in the metal is explained in terms of the stacking fault energy (SFE) and twining stress (a critical resolved stress to nucleate twin structure) based on the relation of $\sigma \propto \sqrt{E_{sf}/(S \cdot b)}$, where σ is twinning stress, E_{sf} is SFE, S is the shear modulus and b is the burgers vector. Additionally, the interaction between dislocation and twin structure should be taken into account for explanation of the twin deformation under which twin boundary migration is led by twin dislocation gliding. Recently Zhu et al. explained various cases of interaction between dislocation and twin boundary [55]. For example, while a shockley partial dislocation (Bα) gliding from matrix plane interacts with the twin boundary, based on the Thompson tetrahedron model, the dislocation (Bα) can be dissociated into another shockley partial (Bδ) and immobile stair-rod dislocation (δα). Once the partial dislocation, Bδ, glides along the twin boundary, leaving the immobile δα dislocation, the distorted lattice plane leads detwinning with reduced twin thickness to stabilize the total energy. Similarly, as a partial dislocation gliding from the interior of the twin interacts with the twin boundary, the twin dislocation dissociated gliding along the twin boundary could lead the twin nucleation.

1.3.3. $YBa_2Cu_3O_{7-x}$ thin films

Since Karl Muller and George Bednoz discovered a high temperature superconducting (HTS) materials in 1986 [56], enormous of research has been carried out to optimize the operation condition. Especially, with the discovery of yttrium barium copper oxide (YBCO) ($T_c > 77K$) in 1987 by Maw-Kuen Wu and Paul Chu, it has brought extensive research interest in terms of both fundamental physics and potential applications. Therefore, HTS YBCO thin film coated conductors have recently became one of the main research directions for YBCO-related research because of their many envisioned applications, including superconducting generators, motors, power cables, and other devices [57-59].

In order to maintain or improve superconducting property of such novel material, processing technique should be very crucial. Specifically, controlling the oxygen contents during the deposition of the thin film is the key factor to manipulate the superconducting property. Usually, HTS YBCO can be formulated with $YBa_2Cu_3O_{7-x}$. And during non stoichiometry growth of YBCO thin film, amount of the oxygen contents changes the structure of the unit cell and its superconducting property. Typically, YBCO can be crystallized as perovskite structure which is made of different composition of layers (CuO, CuO_2 BaO, Y in figure 1.13).

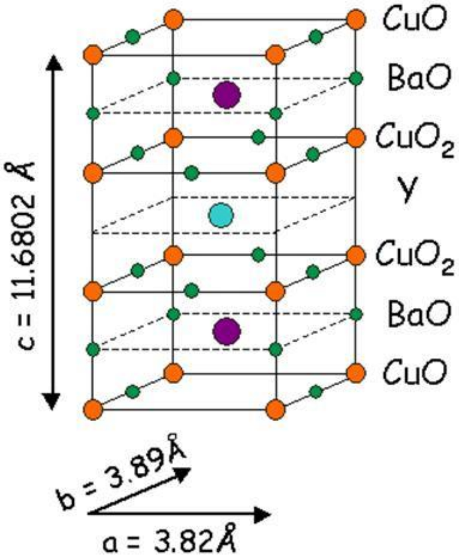

Figure 1.13. Schematic diagram illustrates YBCO perovskite crystal structure with copper (orange), oxygen (green) and barium (purple) atoms.

As less oxygen presents during the processing (x~1), in the layer of CuO the oxygen sites could be vacant. Then tetragonal structure can be formed in the unit cell with lattice constant of a = 3.86Å. Once YBCO formed in tetragonal structure, this material is no longer superconductor but insulator. However, as the oxygen contents have been increased, the layer of CuO has more oxygen. Then tetragonal structure can be transited to orthorhombic structure with lattice constant of a = 3.82 Å, b = 3.89 Å and c = 11.68 Å. Then YBCO could function as a HTS material. During the phase transition from tetragonal to orthorhombic structure, another noticeable phenomenon to enhance the superconductivity is formation of defect which can act as effective pinning centers in YBCO thin film. Flux pinning is to stop motion of the magnetic flux lines under Lorentz force applied to avoid the flux creep. Usually such pinning event can be occurred only with defect formed in the superconducting materials such as grain boundary, embedded impurity particles, etc.. Especially, several recent researches reported that the twin structure formed during YBCO thin film process significantly enhances the superconducting property. For example, Shi et al. has showed increase of critical current density (J_c) with increasing twin spacing [60]. And Safar et al. has reported that J_c has been increased as the twin structure rotated with 45° about current flow while the samples with twin boundary oriented parallel or orthogonal to current direction reduced J_c [61].

Usually twin structure can be formed along (110) planes in YBCO thin film as the stress released during phase transition by oxygen diffusion along a-b plane. The oxygen diffusion is usually occurred along the a-b plane of YBCO rather than c-axis. This is because the activation energy for the oxygen diffusion along a-b plane is lower than that along c-axis [62]. Therefore, the diffusivity of oxygen along a-b plane can be more active. During the diffusion of oxygen along CuO layer, cluster formation along Cu-O chain causes another nucleation of cluster which is oriented orthogonal direction as reducing stress along [110] direction; then during relaxation from the stress, coherent twin boundary can be formed along (110) plane as boundary of the cluster meet each other [63].

With such intrinsic defect in YBCO thin film, additionally to improvement of superconductivity, another possible capability is to enhance the overall mechanical performance. Raynes et al. has demonstrated that during the indentation on twinned and detwinned single crystal YBCO, ~25% of fracture toughness has been increased with twined structure while no significant change of hardness has been observed [64]. And this can be explained by the increase in fracture energy with twin nucleation and twin boundary motion relaxing stress at the crack tip; thus limit the growth of crack while it interacting with twin structures [65].

1.3.4. Al doped ZnO

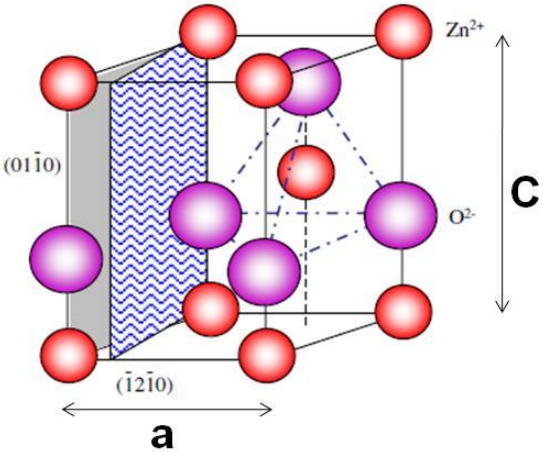

Figure 1.14. Schematic diagram illustrates ZnO hexagonal wurtzite crystal structure with zinc (red) and oxygen (purple) atoms [71].

Transparent conducting oxide (TCO) thin films have a large variety of applications, such as transparent interconnects for optoelectronic devices including liquid crystal displays (LCDs), organic light emitting diodes (OLEDs) and solar cells [66-68]. Among all of the TCO materials researched, recently ZnO (II-VI compound) has brought extensive research interests because of its unique optical and electrical properties and its tunable nanostructures as nanorods, nanotubes, nanowires and nanobelts. In addition, as a direct bandgap semiconductor with a bandgap of 3.4 eV, ZnO can be used for optoelectronic devices operating in the blue to UV regime. Therefore, with such potential properties, it can be excellent candidate as a TCO material over others. Especially, due to low cost and non-toxicity compared to other conventional TCO materials such as GaN, Indium Tin Oxide (ITO), ect., ZnO has promise to be replaceable with the conventional materials [69, 70].

Typically as thermodynamically stable structure ZnO shows hexagonal wurtzite structure with lattice constant of a = 3.296 Å and c = 5.206 Å as tetragonally coordinated Zn^{2+} and O^{2-} ions with *sp*3 covalent bonding compose alternative plane along c-axis (figure 1.14 [71]). However, once high pressure (~9 GPa) has been applied or thin film has been grown on cubic structured substrate such as ZnS, GaAs or etc., possibly cubic structure, i. e. zinc-blende or rocksalt (NaCl), can be formed as metastable structure.

To increase its electrical conductivity, ZnO is usually doped with B, Al, Ga or In (group III elements) as n-type or Na, K, P or N (group I or group V elements) as p-type semiconductors. Among those, Al-doped ZnO (AZO) is one of the most widely studied n-type ZnO films because presence of Al ionic content in Zn site can increase the electrical conductivity as it reduces the grain impedance caused in the grain boundary of ZnO. Recently Matsubara et al. processed Al-doped ZnO thin film at room temperature under oxygen radical-assisted PLD, whose minimum resistivity reached down to 5×10^{-4} Ωcm while it showed about 86~92% of optical transmittance [72]. Additionally, Agura et al. also conducted PLD deposition to deposit Al doped ZnO film on glass substrate and it recorded the lowest resistivity of 8.54×10^{-5} Ωcm with over 88% optical transmittance in the visible wavelength region [73].

AZO thin films with the high transmittance and electrical conductivity have been grown by various deposition techniques such as molecular beam epitaxy, plasma enhanced chemical vapor deposition, sol-gel, sputtering and pulsed laser deposition (PLD). Usually during the deposition AZO tends to grow with different size columnar grains such as nanorods with [0001] direction normal to surface of substrate to minimize the surface energy [74]. While the film grows, it tends to reduce the surface free energy. Therefore, film prefers to grow along plane whose surface energy is lowest. For ZnO the density of surface energy decreases in the order of $(10\bar{1}0)$, $(11\bar{2}0)$ and (0001); thus, it has strong tendency to grow with (0001) plane.

During the deposition, different processing methods and deposition parameters highly affect the physical property of the AZO films. Especially, presence of oxygen contents during the processing increase the collisions between the adatoms from the target and gas molecules; thus it can reduce the mean free path of the adatoms and limit the nucleation size of the films on the substrate. Therefore, the density of grain boundary can be increased as the oxygen pressure increases, which highly affects grain boundary scattering of charge carriers. As a result, controlling the grain size of AZO is very important to have different surface morphologies. For example, Zhu et al. demonstrated variation of the resistivity along increase of oxygen partial pressure based on film surface morphologies [75]. During the deposition of ZnO film by PLD on the glass substrate at 350°C under the different partial oxygen pressures, i.e. 0.003, 0.2, 24 and 150 Pa, the surface roughness has been increased from 0.5 to 6 nm with root mean square (RMS) value along the increasing oxygen pressure, as a result of increase of grain size, which was due to enhancement of collision between flux of adatom and oxygen gas content. Finally, electrical resistivity increased from 1.3×10^{-2} Ω·cm to 1.17×10^{-1} Ω·cm with increase of oxygen pressure. On the other hand, the AZO film grown by the magnetron sputtering showed the electrical resistivity in the range of $3\times10^{-4} \sim 6\times10^{-4}$ Ω·cm at 350 °C while a AZO film grown by the chemical vapor deposition (CVD) has resistivity values ranging from 4.6×10^{-3} to 1×10^{-1} Ω·cm [76, 77]. As the oxygen partial pressure increased from 1 to 100 mTorr, the resistivity increased drastically from 5.1×10^{-4} to 5.2 Ω·cm [78].

1.4. *In situ* TEM characterization

After processing the materials as either bulk or thin film material, various characterization methods have been employed to examine the materials properties. Among them, transmission electron microscope (TEM) has been introduced as the most essential tool to identify the micro/nanostructure within the materials. Especially, with recent development of the *in situ* TEM characterization technique, it provides the opportunity of observing the microstructural evolution during the physical property measurements such as mechanical test with nanoindentation or tensile test, electrical property measurement, etc. in the TEM column. Therefore, the real time observation allows more reliable study with correlation between variation of the physical properties and structural responses than the conventional static TEM analysis approach. Since the last decade, several *in situ* TEM characterization methods have been introduced. For example, *in situ* nanoindentation and straining tests have been developed for analysis of microstructural response of a material under the external stress applied with real time observation. Additionally, *in situ* scanning tunnelling microscopy (STM) has been introduced for direct observation of microstructural evolution under electrical potential applied on a material. Table 1.1 summarizes various results from recent researches on different kinds of nanomaterials characterized with various *in situ* TEM techniques. It shows that depending on the materials, different *in situ* characterization methods are required to reveal concealed properties. For the metal regardless of its size dimension, most of the studies introduced microstructural evolution such as dislocation, grain and, grain and twin boundary activities during deformation behavior. On the other hand, for the ceramic, it can be noticed that the most of the ceramic materials employed for the *in situ* test are one dimensional material such as nanowire or nanotube. And either electrical or mechanical test has been performed on them. This can be because once the three dimensional bulk ceramic, which is mechanically very hard and brittle, and electrically insulating without dopant, reduces its dimension, it can expose any hidden properties with active reaction about small variation of atomic rearrangement under the external impact. Besides these, *in situ* TEM tests on newly discovered material such as carbon nanotube or graphene have also been conducted to reveal its unknown physical properties. Therefore, as such a useful tool, more dynamically approaching to analyze a material, *in situ* TEM characterization methods could be very potential as having advantages over conventional TEM analysis.

Table 1.1. Recent research progress with *in- situ* TEM characterization on various nanomaterials.

***In situ* TEM characterization**			
Material		**Major observation (Type of *in situ* test)**	**reference**
Metal	Nanocrystalline Al thin film	- Grain rotation and coarsening, grain boundary migration and grain growth **(Nanoindentation)**	[79]
	Single crystal Al	- Increment of strain rate with dislocation nucleation **(Tensile test)**	[80]
	Nanocrystalline Ni pillar	- Strain hardening based on annihilation of dislocation **(Nanoindentation)**	[81]
	Al/Nb multilayer thin film	- Dislocation climbing at the Al/Nb interface **(Nanoindentation)**	[82]
	Nanotwined Cu thin film	- Dislocation multiplication at Twin boundary resulting in migration of coherent twin boundary **(Nanoindentation)**	[83]
	Au nanowire	- Dislocation mediated plasticity and phase transition through the necking process **(Tensile test)** - Cold welding by atomic surface diffusion and structure relaxation **(Contacting and pulling)**	[84, 85]
	Ni thin fim	- Grain boundary deformation mediated by porosity **(Tensile test)**	[86]
	Martensitic steel	- Grain boundary deformations after dislocation activities at low and high angle grain boundaries **(Nanoindentation)**	[87]

Table 1.1. Continued

***In situ* TEM characterization**			
Material		**Major observation (Type of *in situ* test)**	**reference**
Ceramic	GaN nanowire	• Dislocation nucleation and propagation leading fracture **(Uniaxial compression)**	[88]
	ZnO nanowire	• Phase transition from crystalline to amorphous **(Nanoindentation)** • Size dependent young's modulus through fracture test **(Tensile test)**	[89, 90]
	Bi_2S_3 Nanowires	• *In situ* I-V measurement **(I-V measurement)**	[91]
	SnO_2 nanowire	• Volume expansion of SnO_2 nanowire while lithiation with charging up to -3.5V **(Electrochemical charging)**	[92]
	BN nanotube	• Fracture induced by electric current heat **(Electric heating)**	[93]
	TiN thin film	• Grain boundary diffusion comprised of dislocation activities **(Nanoindentation)**	[94]
Others	Carbon nanotube (CNT)	• $\frac{1}{2}$<0001> sessile dislocation motion (glide and climbing) under increment of temperature from room temperature to 2000°C **(Electric heating)** • Kink motion under high temperature of 2000°C during tensile test **(Tensile test)**	[95, 96]
	Graphene	• Multilayer reconstruction and sublimation **(Electric heating)**	[97]
	Si nanowire	• Anisotropic expantion along [110] and [111] of Si nanowire during lithiation **(Electrochemical charging)**	[98]

1.4.1. *In situ* TEM nanoindentation

Since nanoindentation has been developed in the mid of 1970s, this method is the most mainly used technique to measure the mechanical properties of small volume of materials such as hardness, stiffness and young's modulus as accompanying the force-displacement plot. More potentially, this tool cannot just be used to measure the mechanical values, but it can also estimate different phenomenon during deformation events of the materials as combined with several different postmortem experiments. Recently, several research studies have reported the interesting results of deformation event during the nanoindentation process. During the nanoindentation on (001) GaAs wafer, the force-displacement plot shows obvious pop-in effect occurred at around 45 mN on the wafer [99]. And as correlating with TEM analysis, it has been conclude that this pop-in effect could be occurred with nucleation and extension of dislocation loops, which possibly enhance the plastic deformation. In addition of pop-in effect by the dislocation activity, another interesting feature which could be observed during the indentation is phase transformation. During the indentation on p-type (001) Si wafer, the force-displacement plot shows the pop-out effect around 10 mN during unloading process, which has been induced by the phase transition from single crystal to amorphous structure [100]. However, in spite of such enormous efforts, direct observation of the deformation events during the microstructural evolution under indentation has still been desirable. Finally, such eager to have more advanced technique for material characterizion enables *in situ* TEM nanoindentation system to be developed. And it has become currently one of widely used system to explore microstructural evolution in the nanomaterials during the deformation under real time observation. For the *in situ* TEM nanoindentation, as diamond nanoindenter tip, indenter sensor and piezoelectric motion controller have been equipped in conventional TEM holder, under the TEM column, indentation can be conducted with fine motion of TEM specimen, approaching to the nanoindenter tip. More potentially, during the indentation, the indenter sensor can detect the pressure sensed by tip and generate the force-displacement plot just like the conventional *ex situ* nanoindentation system. Therefore, it can provide chance of more quantitative study.

With such novel technique, lately several research studies have demonstrated impressive property-structure correlations of nanomaterials with *in situ* TEM nanoindentation. Jin et al. has demonstrated that the different deformation behaviors of aluminium (Al) thin film depending on the size of grains during the *in situ* TEM nanoindentation [79]. When the grain size is on submicrometer range, grain boundary migration and grain coalescence have been observed, which is mainly driven by dislocation interaction at the grain boundary. Meanwhile, nanocrystalline Al thin film shows rapid change of deformation behavior with grain growth and grain rotation. Similarly, Ohmura et al. also introduced the novel result of grain boundary and dislocation interactions during *in situ* TEM nanoindentation on martensitic steel [87]. During the indentation near the low-angle grain boundary, significant dislocation pilling up event at the boundary was observed, following with emission of the dislocations through the boundary under further indentation. Meanwhile, as indentation conducted near high-angle grain boundary, the dislocations generated disappeared, as absorbed by the boundary. Finally, after the indentation, for the low-angle grain boundary, significant shift of the grain boundary was noticed, while the high-angle grain boundary was very static but only the grain showed severe deformation. Even though Conrad's analysis has explained that kinetically stress flow in the material could be driven by the dislocations piled up at the grain boundary which can enhance the grain boundary shear when the grain size of the material is within range of 10 nm ~ 1 μm [53], with such novel experiment under TEM column, size dependent grain boundary mediated plastic deformation could be verified based on the real time observation. Additionally, Li et al. also shows novel deformation behavior of nanotwined Cu thin film during the *in situ* nanoindentation [83]. In this report, it has been demonstrated that under the high resolution TEM column, dislocation multiplication at the twin boundary results in migration of coherent twin boundary based on the following steps. 1) A lattice dislocation glides toward the twin boundary under stress applied during the indentation. 2) As the lattice dislocation going through the boundary, it can be dissociated into a sessile partial dislocation and mobile twin dislocation. 3) As the twin dislocation gliding along the twin boundary, lattices can be rearranged and finally, twin boundary could be migrated. 4) Then as the sessile dislocation dissociated into another full dislocation and twin dislocation, the deformation procedure could be repeated. Although theoretical approach of this phenomenon has been introduced based dislocation activities on Thompson tetrahedron model [55,101], the conventional theory can be confirmed with such practical result from the direct observation during the *in situ* TEM nanoindentation. Besides the *in situ* mechanical tests on thin film and bulk materials, Shan et al. demonstrated the strain hardening based on annihilation of dislocation in one dimensional single crystal nickel (Ni) pillar [81]. During the *in situ* test, Ni pillar which initially had high defect density becomes defect free after the external force applied. Simultaneously, the maximum stress applied on the pillar was increased with ~60%, compared to that loaded on the initial state based on the load-displacement plot. It could be possible based on Greer et al.'s report which explained that before defects interact or multiply with other defects, they could leave from the free surface of the crystal as the size of width in the nanomaterial becomes relatively smaller than that of length [102], and after all, nucleation of the new dislocations requires higher stress for plastic deformation. Finally, with such novel experiments in the metal samples, the direct observation of deformation behavior can provide the clear evidence to support the conventional theory, or disclose a hidden deformation mechanism.

However, compared to research on the deformation behavior of the metal samples, there were only few *in situ* studies introduced on the ceramics during the indentation process. This is because during the deformation of the ceramic at room temperature, it usually becomes fractured as skipping plastic deformation zone. In spite of the fact, the recent *in situ* tests on several ceramic materials provide the possibility of being the plastic deformation zone in the ceramics. For the ceramics, most of the *in situ* nanoindentation tests are conducted on the one dimensional semiconductor materials. This is because as the dimension of a ceramic reduces from 3D bulk to 1D nanowire or nanotube, the enhanced mechanical properties could be exposed, i.e. ultimate strength of the 1D ZnO nanowire could be significantly increased with about 40 times greater than the bulk value [103]. Recently, Huang et al. showed the deformation behavior of GaN nanowires under which fracture mechanism was explained, following with local plastic deformation based on dislocation activities [88]. Under compressive stress, dislocation nucleation and piling up was observed in the surface of the nanowire right under the punch, which induced the lattice distortion and finally local plastic deformation. However, in this report, the nanowire never showed any global plastic deformation which could be observed in the metallic systems. And it seemed difficult for such ceramic materials to have broader plastic deformation regime. Nevertheless, Minor et al. demonstrated that dislocation activity enhanced plastic deformation in TiN, a metallic ceramic, during the *in situ* nanoindentation [94], which is similar to deformation behavior in the metallic system in which dislocation activity mainly dominates the plastic deformation. During the indentation on TiN thin film grown on MgO substrate, the relatively soft substrate (with hardness 9 GPa of MgO) led the banding of the hard thin film (with hardness 20 GPa of TiN). During the bending of the film, hemispherical shaped area with dark contrast was observed which indicated distribution of high defect density. Finally, 8° grain boundary tilt was noticed within in this area, which could possibly induced by dislocation activity, accompanying with grain boundary diffusion. And this provides clear evidence of possibility of being plastic deformation in hard ceramic materials.

1.5. Summary

Remarkable development in the field of nanotechnology has been driven by the discoveries of various nanostructured materials. With the recent advances of high resolution imaging and physical property measurement techniques, developing the nanostructured materials with further enhanced physical properties is possible. Especially, the development of the *in situ* TEM characterization technique has brought the possibility of direct observation during real-time experiments as providing new approaches to characterize a material in the more reliable idea. Among the approaches, the *in situ* TEM nanoindentation is one of the most broadly used technique to characterize the mechanical property of materials. The direct observation in the deformation behavior of the nanomaterials can provide the clear evidence to support the conventional theory and disclose a hidden deformation mechanism. However, since most of the *in situ* works have been apparently focused on metallic and nanowire systems, the work on nanostructured ceramic using *in situ* tools is still scare. Additionally, the works highly rely on the qualitative study. Therefore, *in situ* TEM characterization on ceramic materials such as ceramic nanocomposite and ceramic thin film material could be required for future research with a comparison study on nanocrystalline metal as combined with more quantitative study.

CHAPTER II

RESEARCH METHODOLOGY

2.1. Transmission electron microscopy

Transmission electron microscopy (TEM) is one of the most widely used methods to obtain the structural morphology of a material. Especially with the capability to identify the internal structure underneath of the surface while the electrons transmit through the TEM specimens, this system can be clearly distinguishable with other microscopes. Additionally, as providing projection of microstructure in atomic level, it can lead us to comprehend the material systems. As a result of such potentiality of the technique, these days it cannot be just employed by field of material science research but other areas such as microelectronic device technology, biotechnology, and other material related field also require its application. For instance, during the microelectronic device fabrication, thin film surface uniformity and structural morphology can be inspected under the TEM column. Although large portion of the film quality analysis still highly relies on surface analysis tools such as atomic force microscopy (AFM) and scanning electron microscopy (SEM), the analysis ability on the internal microstructure of a material along with the cross-section view is entitled by TEM technique to exceed the capability of such surface analysis systems. And this capacity of TEM has also provided clear evidence of interfacial reaction and surface diffusion after the device processing. Therefore, TEM has become the most crucial technique which can explore structural and defect analysis. Within such remarkable system, as other analytical techniques, such as STEM, EELS, and EDX have been combined together, this system could become even more powerful to characterize a material as integrating chemical composition analysis technique within single atomic scale. Currently, JEOL JEM-2010 and Tecnai F20 super-twin (at TAMU) have 0.23 and 0.24 nm respectively for the point resolution. For this section, many parameters of TEM are explained. And several important techniques such as imaging and diffraction are presented.

2.1.1. Resolution

Resolution and magnification can be introduced as the main parameter of TEM. Although the magnification can be readily adjustable by change of acceleration voltage, there are several parameters considerable for enhancement of the resolution. When no aberration effect considered, the maximum resolution of the microscope can be theoretically variable mainly by wavelength of the electrons and aperture angle of lens, which can be explained based on Rayleigh criterion as shown below:

$$\mathrm{r} = \frac{0.612}{\mathrm{n}\,(\sin\alpha)} \qquad (2.1),$$

where   is the wavelength of the electrons, n is refractive index (usually, for vacuum, n = 1) and α is aperture angle of lens. Usually, in TEM, as the electron accelerates to generate more coherent beam, the wavelength of beam could be shortened in the order of hundredth of 1 Å. Then the resolution value could be smaller.

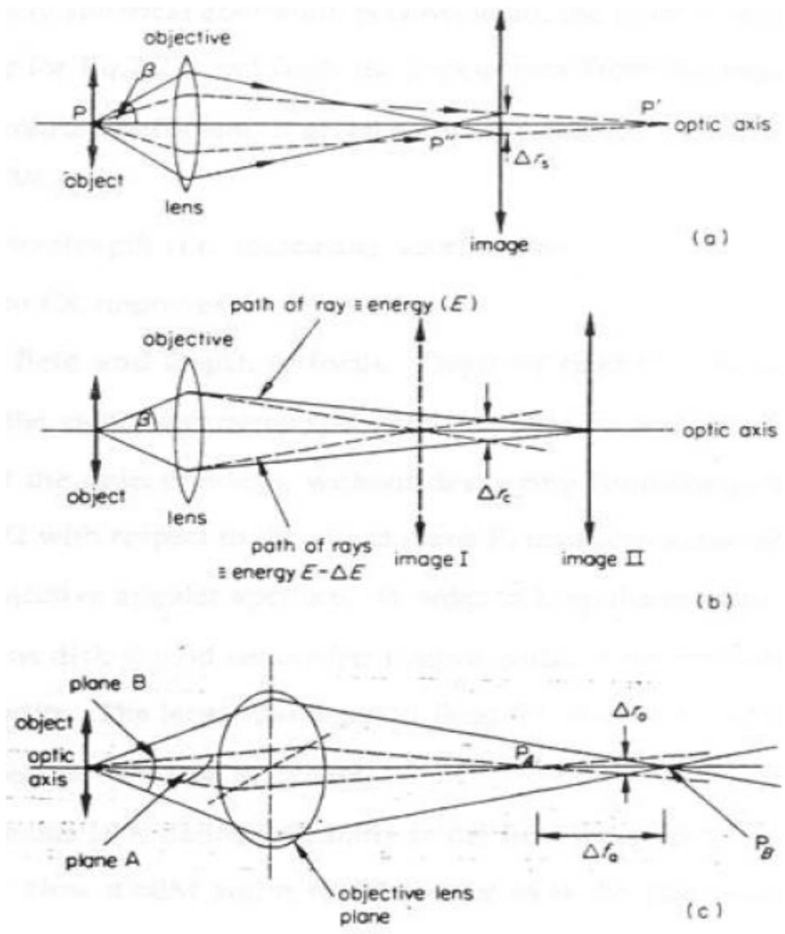

Figure 2.1. Diagrams illustrate the objective aberrations: a) spherical b) chromatic, c) astigmatism [104].

Besides these parameters from the criterion, there are additional factors to affect the resolution of the microscope. First, spherical aberration can be explained. Spherical aberration is one of main lens defects caused by more refraction when the incident electron beam going through near edge of the lens compared to that passing through the centre of the lens (Figure 2.1a). Therefore, the electron beam near from edge of the lens could be focused before the image plane while the beam going through the centre of the lens is focused on the plane. And finally, for such non-paraxiality of the electron beam, the spherical aberration disk with radius r_s can be made with relation of $r_s = C_s\beta^3$, where β is angular aperture of the lens.

Following the spherical aberration, next introducible factor is chromatic aberration. Usually, the chromatic aberration is occurred due to the energy difference (ΔE) from incident electrons. Once the electrons have different energy, less refraction through the objective lens could be expected from fast electrons while the slow electrons cause high angle refraction. Therefore, the focal lengths between these two groups of electrons can be different (Figure 2.1b). Usually, the chromatic aberration can be worse when TEM specimen thickness becomes thicker. Thus to avoid the aberration, preparation of the thin specimen is essential.

Finally, astigmatism can be introduced as the last factor to affect the resolution. Astigmatism usually comes from non-uniform magnetic field which results in different focal length (Figure 2.1c). There are several reasons causing this problem. It can be caused by the vibration of the electromagnetic field due to non-uniform surface of cylindrical polepieces and contamination charging up the electron beam. Then projected TEM image can be deformed with radius r_{ast} as shown below:

$$r_{ast} = \beta\Delta f \qquad (2.2),$$

where Δf is the maximum difference in focal length coming from astigmatism. And it can be easily fixed as adjusting the field.

2.1.2. Depth of field and depth of focus

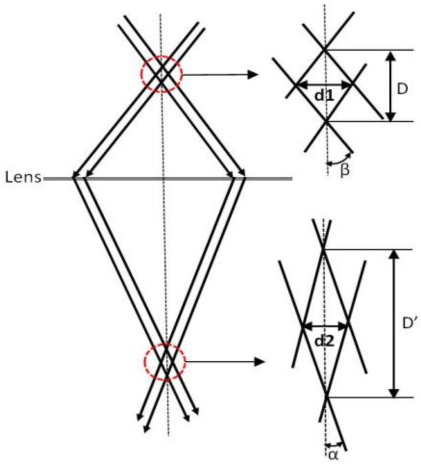

Figure 2.2. Schematic diagrams illustrate depth of field and depth of focus [105].

Once a beam with multiple rays going through the specimen, depth of field, D, is vertical distance between points at which the rays cross over along the central axis on objective plane, maintaining the resolution (Figure 2.2). And it can be defined as the equation (2.3)

$$D = \frac{d1}{\beta} \qquad (2.3),$$

Similarly, depth of focus, D’ can be described another vertical distance between points at which rays cross over along the central axis, but on image plane instead of object plane. And D’ can be defined as the equation (2.4)

$$D' = \frac{d1}{\beta}\left(\frac{d1}{d2}\right)^2 = \frac{d1}{\beta}\left(\frac{\beta}{\alpha}\right)^2 \qquad (2.4),$$

Therefore, it can be noticeable that as β becomes decreased with selecting small size of aperture, the depth of field, D, and depth of focus, D', can be increased. For example, when the d1 is 1Å and β is 5×10^{-3} radius, depth of the focus can be 20 nm. Then any region of the specimen which thickness less than or equal to 20 nm can be focused. Usually, for the thick specimen with a lot of electron beam scattering, β can be 10^{-2} rad, while the thin specimen can have β with $\sim10^{-4}$ rad. Eventually, preparation of thin specimen can be very essential to have broader range of the D and D'.

2.1.3. Image and diffraction modes

Once the coherent electron beam transmits through the specimen, it can be dispersed and refocus on the image plane by the objective lens. Once the beam dispersed by the lens, in the back focal plane the diffraction pattern can be generated. At this moment, as size of the beam gets smaller and selected area diffraction (SAD) aperture is inserted in the image plane, beam coming from the specimen outside will travel through the SAD diaphragm (Figure 2.3a). Then on the viewing screen, the diffraction pattern can be projected.

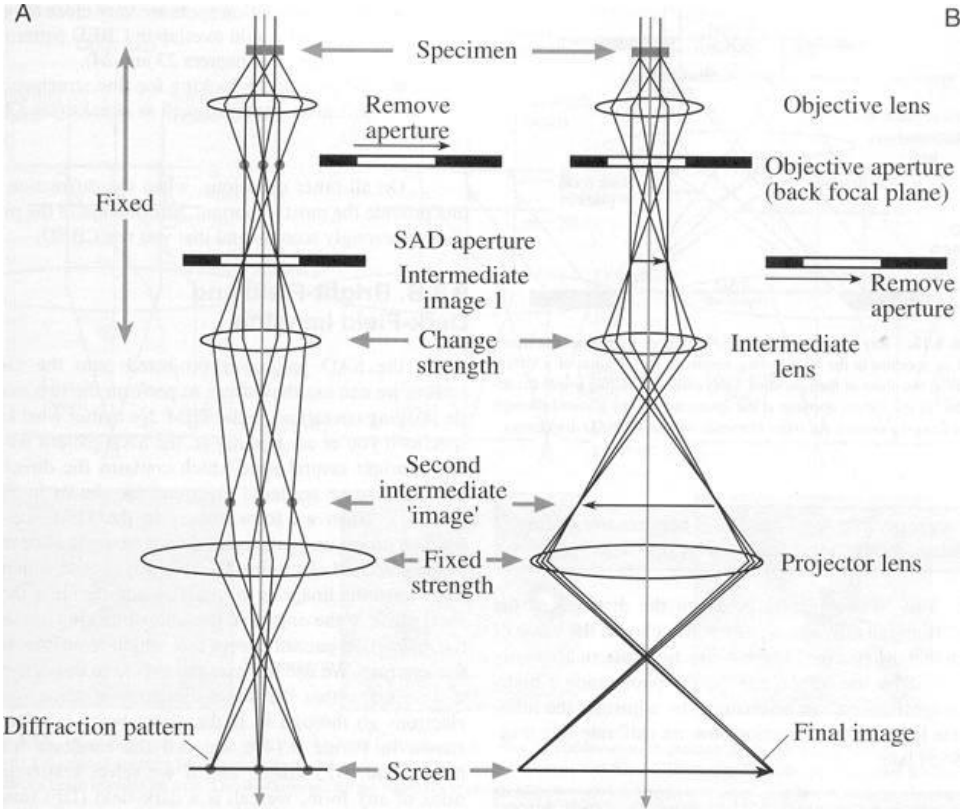

Figure 2.3. Schematic diagrams illustrate the basic operation of TEM imaging system under a) diffraction mode and b) imaging mode [105].

The generation of the electron diffraction can be explained based on two features. First, as the wavelength of the electron beam is smaller than the lattice distance, the diffraction angle can be smaller. Then Bragg's law defined as $2\mathrm{d} \cdot \sin\theta = \mathrm{n}\lambda$ becomes $2\mathrm{d} \cdot \theta = \mathrm{n}\lambda$ since $\sin\theta \sim \theta$ with $\theta \sim 0.5°$. Second, as the specimen becomes very thin, the projected diffraction can be in the rod form of the domain especially for single crystal. Then Ewald reflection sphere could overlap the diffraction domain for active state of hkl reflection. Finally, based the relation of the reflection indices, hu+kv+lw=0, the reflection on the (hkl) lattice planes can have the incident direction with [uvw] along the zone axis, which can be explained in reciprocal plane (uvw) including the lattice point hkl.

For the image mode, as the object plane becomes the image plane of the objective lens with adjustment of the intermediate lens, image can be projected on the viewing screen (Figure 2.3b).

2.1.4. High resolution TEM (HRTEM)

As detailed analysis of structure of a material within range of atomic scale under higher resolution, such as atomic structure, position of atom and any defects emergence in the structure, is desirable, it can be possible with high resolution TEM (HRTEM). And it can be approached as consider the microscope as a linear system. Under the linear system based on the relation of $\alpha S_0 + \beta S_0 \rightarrow \alpha S_1 + \beta S_1$, transmission of the input signal, $\alpha S_0 + \beta S_0$, is linear related with the output signal of $\alpha S_1 + \beta S_1$. Then through the signal processing system of the microscope in figure 2.4, the input signal of the object phase shift induced by the specimen is processed by the function of the fourier transform; then after processing with phase contrast transfer function, final output signal can be gained by the inverse fourier transform function, generation of TEM contrast can be explained.

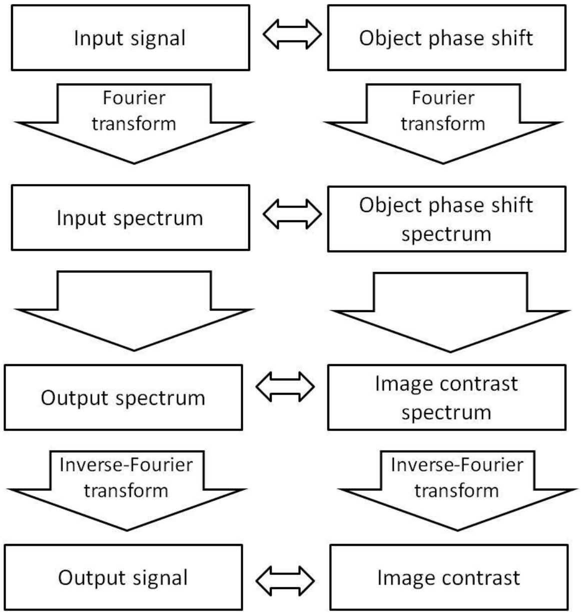

Figure 2.4. Diagram shows signal transmission system in TEM.

2.2. Nanoindentation

Since nanoindentation has been developed in the mid of 1970s, this method is the most mainly used technique to measure the mechanical properties of materia, such as hardness, stiffness, elastic modulus, etc., of small volume of material like thin film materials. Especially, with analysis based on the load-displacement plot, any concealed mechanical property of the material can be revealed during the indentation process. Figure 2.5 shows several material responses with different properties during the indentation process, i.e. high ductility from steel, brittleness from fused silica, phase transition from crystalline silicon, cracking from sapphire evidenced with pop-in event and creep event from polymer.

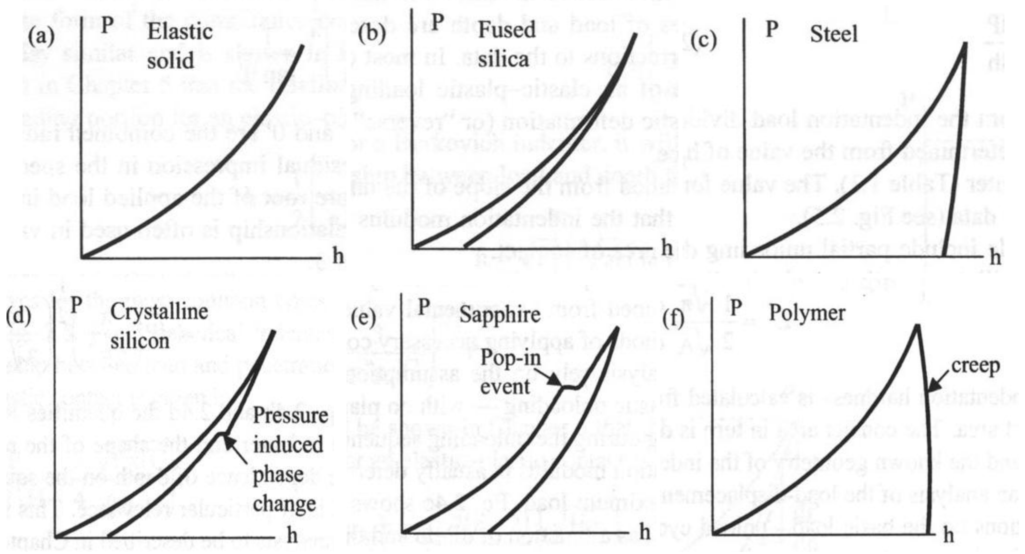

Figure 2.5. Load displacement plots show different material responses (different properties) during the indentation process: a) Elastic, b) brittle, c) ductile, d) phase transform, e) cracking, f) creep [106].

Conventionally, indentation technique has been used to measure the hardness of a material as a hard tip with known mechanical property compresses down into the surface of a material with unknown property. At this point, the hardness can be simply defined with the relationship as shown below:

$$H = \frac{P_{max}}{A} \qquad (2.5),$$

where P_{max} is the maximum pressure applied by the tip on the surface of the material and A is the projected area of the tip on the surface of the material.

Due to the various geometries of the tips employed for the indentation test, the hardness values can be changeable as the projected area in the relationship can be varied by the shape of the tip. As simply considering about the contact of a hard sphere on a flat surface of a material with its elastic modulus E (Figure 2.6a), radius of the contacted sphere circle, a, can have relationship in equation (2.6) show below:

$$a^3 = \frac{3}{4}\frac{PR}{E^*} \qquad (2.6),$$

where E^* is reduced modulus which can be given by $1/E = (1-\upsilon^2)/E + (1-\upsilon'^2)/E'$ with which the first term of $(1-\upsilon^2)/E$ is for the indenter tip and the second term of $(1-\upsilon'^2)/E'$ for the sample (υ: Poissons's ratio), and R is relative radius. Figure 2.6b also illustrates the load-displacement plot after the nanoindentation process in figure 2.6a. Based on the following calculations, the values of hardness H and elastic modulus E^* can be estimated.

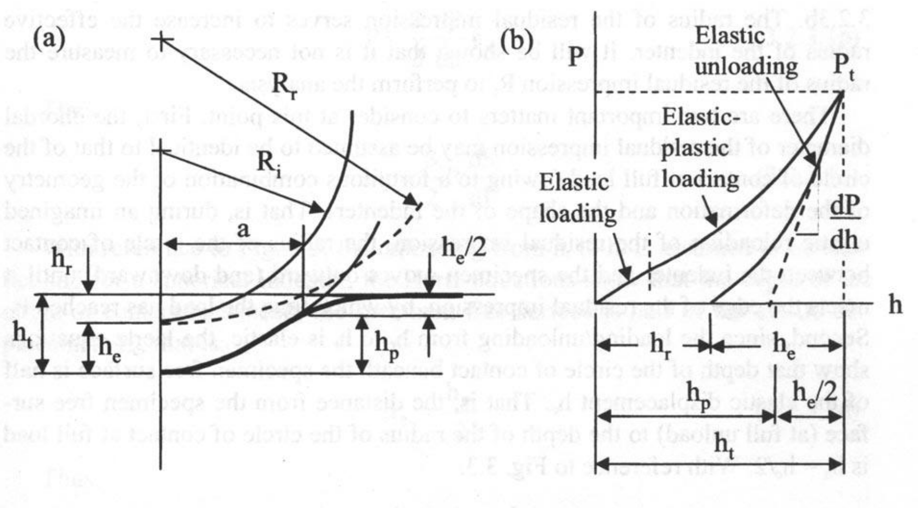

Figure 2.6. a) Schematic diagram illustrates indentation with standard spherical indenter and related parameters from measurements. b) Load displacement plot is resulted from the indentation [106].

As starting with $P = \frac{4}{3}E^{*}R^{1/2}h_e^{3/2}$,

$\frac{dP}{dh} = 2E^{*}R^{1/2}h_e^{1/2}$ (2.7),

Then $E^{*}R^{1/2} = \frac{3P}{4h_e^{3/2}}$. (2.8),

After plugging (2.8) into (2.7),

$P = \frac{2}{3}\frac{dP}{dh}h_e$ or $h_e = \frac{3}{2}P\frac{dh}{dP}$

Since $h_a = \frac{h_e}{2}$, $h_a = \frac{3}{4}P\frac{dh}{dP}$

Based on Hertz' model, $h_e = \frac{a^2}{R}$, where a is the radius of the contact area.

Then from equation (2.6), $h_e = \frac{a^2}{R} = \frac{3}{4}\frac{P}{E^{*}a}$

Then, $h_a = \frac{3}{8}\frac{P}{E^{*}a} = \frac{3}{4}P\frac{dh}{dP}$,

Finally, elastic modulus E^{*} can be estimated with $E^{*} = \frac{1}{2}\frac{1}{a}\frac{dP}{dh}$.

Then the hardness H can be expressed as $H = \frac{P}{A}$, where A is the contact area with $A = \pi a^2$.

As a certain amount of load from the indenter is applied on the surface of sample with a contact area A, the depth of penetration can be measured. The contact area under maximum load can be decided by the penetration depth of the tip and either known angle or radius of the indenter tip. And then desirable properties of the materials can be estimated such as the elastic modulus and hardness.

Finally, for the data analysis based on the load-displacement plot, multiple point measurement and single point measurement can be introducible. For the single point method, Hertz contact equations can be directly applied with two data points. On the other hand, for the multiple point method with which several data points are selected, derivative between the points are necessary. Thus, the single point method can be processed faster while the multiple point method generates finer elastic response, taking a longer time.

2.3. *In situ* TEM nanoindentation system

Since Wall and Dahmen developed *in situ* TEM nanoindnetation system in 1997, it has been widely used characterization technique, especially for mechanical property of materials, allowing direct observation of the deformation behavior during the indentation process under TEM column. And such dynamic experiment could be possible after sharp diamond tip mounted in the specimen holder and three dimensional motions of either tip or specimen controlled by piezoelectric drives. Especially, as the pressure sensor equipped along the tip permits to plot load-displacement just like the conventional nanoindentation system, it has brought a chance of quantitative study. Therefore, with such potential technique, by this time, a lot of valuable research achievements have been made in the field of the material science research. Among them, observation of dislocation activity and its correlation with grain and twin activities in the metallic system could provide clear evidence to support the conventional theories [79, 81, 82, 83, 87]. Additionally, discovery of new phenomenon via the *in situ* test could expose possibility for development of advanced materials. For this section, the components composing the *in situ* TEM nanoindentation system are introduced as combined with explanation for several required parameters.

2.3.1. Major components of *in situ* nanoindentation system

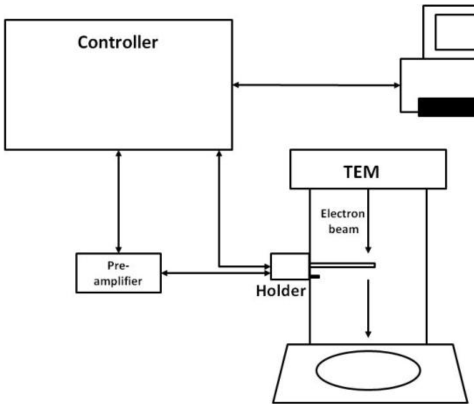

Figure 2.7. Schematic diagram illustrates the experimental set-up for *in situ* nanoindentation.

In situ TEM nanoindentation system manufactured by Nanofactory inc. is composed of two main components, *in situ* specimen holder and control system, with several peripherals as shown in figure 2.7. *In situ* holder is the major part to hold the TEM specimen and indenter sensor which are directly observable under TEM column. The *in situ* holder is mainly composed of three parts. Starting with front-piece which is mainly under electron beam transmission in the TEM column, rod and end-piece can be introduced next as illustrated in figure 2.8a. Unlike the conventional TEM specimen holder, the front and end pieces from the *in situ* holder could require different design as considering the piezoelectric motion of the sample and indentation procedure. As a result, the enlarged image of the front-piece in figure 2.8b shows that a small hat holding the TEM specimen on half grid should be mounted on the sapphire ball which is connected to piezo tube for smoother motion of the specimen. And as the indenter sensor (indenter tip) installed in the very front area of the holder, it allows the direct contact with the specimen under the electron beam transmission in TEM.

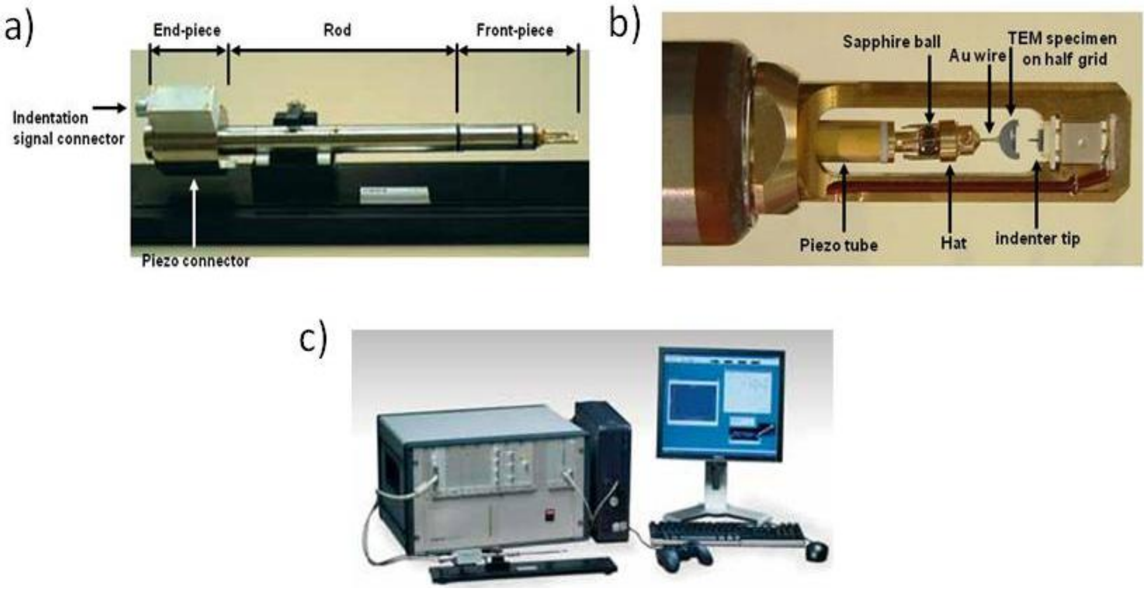

Figure 2.8. Three major component of *in situ* TEM nanoindentation system is decribed: a) *in situ* nanoindentation holder, b) enlarged image of front piece of the holder with TEM specimen loaded, c) control system and computer.

Finally, the end-piece of the holder has several wire connectors for indentation signal and piezoelectric signal which are transferred through the control system as shown in figure 2.8c. Once the indentation process is initiated, the indentation tip is fixed while the sample moves toward the tip by a piezoelectric stage. For the movement of the sample, several parameters can be changeable depending on different settings on the specimen motion control program (software from nanofactory inc.) such as motion speed in unit of nm/step, maximum indentation depth and force, and holding time at the maximum depth. During the indentation, the loading process between the tip and specimen can be captured by a built-in CCD camera in the microscope. After the indentation, based on data detected by the control system, force-displacement plot can be displayed on the computer in figure 2.8c.

2.3.2. Nanoindentation tip and alignment with specimen under TEM

Similar with the conventional nanoindentation system, *in situ* system also requires various kinds of indentation tips such as Berkovich, Conical and Vickers. Unlike the conventional nanoindentation which is conducted on large dimension of surface, for the *in situ* nanoindetation which is conducted on very small surface area of the thin foil, a defect such as slip between the tip and specimen during loading should be considered. And in order to solve the problem, wedge and punch shaped tips are currently widely used, with which contact area between the tip and surface of the specimen is broader. Because of the different geometries of the tips, different parameters are required for calibrations of the tips. The table 2.1 shows the sensor data for each tip after calibration by nanofactory instrument Inc.

Table 2.1. Calibrated indenter sensor data

Tip type	k [N/m]	P_0[μN]	P_1[NpF]
Berkovich	450	1500 ± 300	-5200 ± 1500
Conical	450	1400 ± 300	-5500 ± 1500
Vickers	900	3950 ± 300	-15550 ± 1500
Wedge	1400	2840	-5735
Punch	3400	5825	-13245

where k is mechanical spring constant, P_0 and P_1 are force calibration coefficient with accuracy ± 5%. Based on these data, the control system could tune sensor parameters to identify the tip type. Then indentation could be initialized.

Once the specimen and sensor of indenter tip is installed in the holder, next step before conducting the indentation is for alignment between the tip and thin specimen. Unlike the conventional indentation procedure which is conducted on large surface area of the sample, as the *in situ* nanoindentation conducted on the thin foil, the alignment of the specimen along the same eucentric height as the tip positioned is very critical for the right amount of the force applied between the tip and specimen. Typically, the alignment of the tip and specimen can be carried out based on adjusting their eucentric heights (z-height). As starting with setting the eucentric height of the tip by control panel from TEM system, the z-height of the specimen can be adjustable by the piezoelectric motion control from the motion control program.

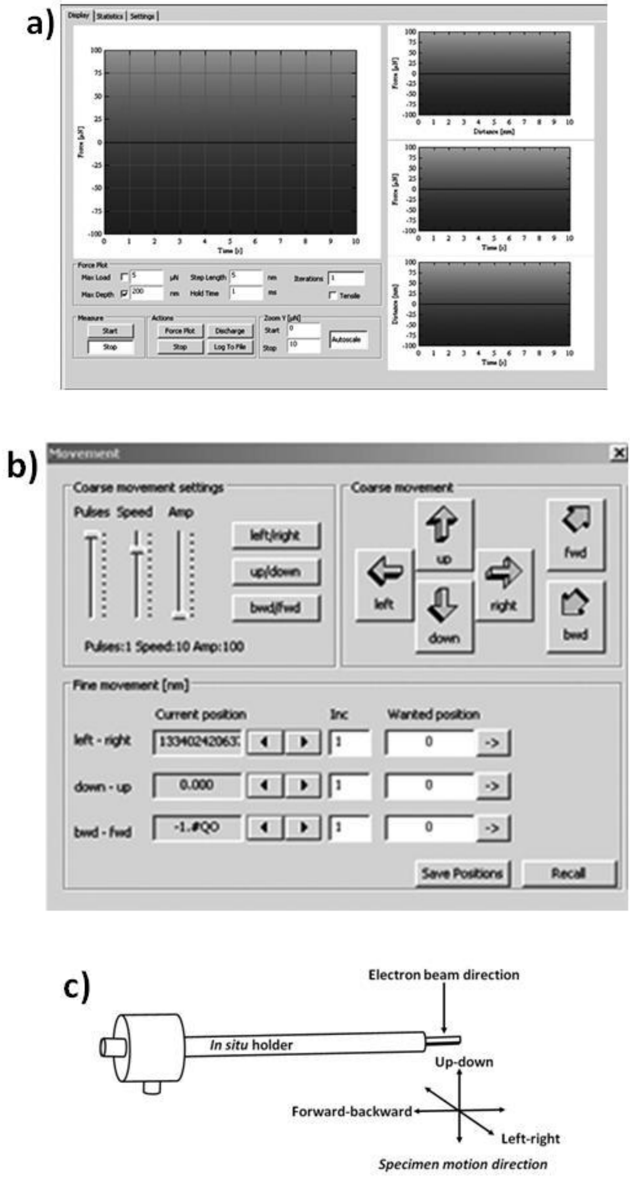

Max Load ☐ 5 µN
Step Length 5 nm
Iterations 1
Max Depth ☑ 200 nm
Hold Time 1 ms
☐ Tensile
Zoom Y [µN] Start 0 Stop 10

Pulses:1 Speed:10 Amp:100

	Current position	Inc	Wanted position
left - right	13340242063;	1	0
down - up	0.000	1	0
bwd - fwd	-1.#QO	1	0

Figure 2.9. Graphical user interface (GUI) program shows a) main control window and b) motion control window. The motion control can be performed based on c) the specimen movements

2.3.3. Electronic control

The piezoelectric motion control can be performed in the graphical user interface (GUI) program provided by Nanofactory inc. Once the program is open, the control window, shown in figure 2.9a, is popped up. The motion control during the tip alignment with the specimen can be carried out in GUI window in figure 2.9b. During the coarse movement setting, the pulse, speed and amplitude can be adjustable from the coarse movement setting section. The pulses slider can change the maximum number of steps per a click of the button in the coarse movement section. The speed slider can adjust the step frequency up to 50 pulse/sec. And the amplitude slider can be used to set the different amplitude applied by voltage pulse which controls the piezoelectric tube. Then actual motion control can be performed with key button in the coarse and fine movement sections. Figure 2.9c shows the specimen movement direction based on six different buttons, i.e. up, down, right, left, fwd and bwd, displayed in figure 2.9b. Once the button clicked, the number of pulse can be generated and the specimen can be moved to preferred direction. For the fine movement, the different directional motion can be controlled by clicking the arrows in the fine movement section. During the fine motion, change of the step size can be possible with input of different number in "**Inc**" boxes. After aligned the specimen along the height of the tip, next step is to conduct the indentation process.

To initiate indentation, several steps are required for customized outcomes. For the section of the force plot from the window in figure 2.9a, the maximum load and depth, step length and hold time can be set up. Maximum load the sensor can reach is up to 3000 μN. Step length in unit of step/nm controls the fine motion of the sample during loading process. And holding time can be set up for time period held during the maximum load. After every desired parameter is input, the indentation process can be initiated as clicking the "**starting**" button in measure section. Once the measurement is started, the main force-time diagram shows fluctuation of electrical signal. Then as clicking the button of "**force plot**", a cycle of indentation can be performed based on the parameter set up in the section of force plot. Once the indentation initiated, force-time plot is generated in the diagram. Simultaneously, the *in situ* experiment can be recorded by a real-time movie using a built-in CCD camera in the microscope. After the cycle of indentation finished, three different plots (Force-distance, Force-time and Distance-time) can be generated in the diagrams from right column of the window in figure 2.9a.

2.3.4. Contact mechanics

For the conventional indentation test, based on Hertz contact model [107], **t**he maximum instantaneous pressure can be estimated from equation 2.9.

$$p = \frac{1.817}{\pi} F^{1/3} (\mathrm{E}^*/\mathrm{R})^{2/3} \qquad (2.9)$$

where F is the load, E* is the reduced modulus, and R is the radius of curvature of the indenter. However, this estimation did not concern about geometrical factors such as TEM foil thickness, which might result in an overestimation of the pressure value. Therefore, after considering the geometric parameters of the specimen, the calculation of the actual stress applied could be possible. Figure 2.10 shows the projection image of the nanoindenter tip along cross-sectioning view.

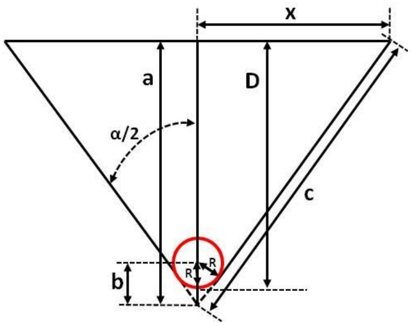

Figure 2.10. A schematic diagram illustrating projection image of the nanoindenter tip along cross-sectioned view.

In the figure, $x = c \cdot \sin\frac{\alpha}{2}$ and $c = \frac{a}{\cos\frac{\alpha}{2}}$

Then, $x = a \cdot \left(\frac{\sin\frac{\alpha}{2}}{\cos\frac{\alpha}{2}}\right) = a \cdot \tan\frac{\alpha}{2}$, where $a = \frac{R}{\sin\frac{\alpha}{2}} + (D - R)$, since $\frac{R}{b} = \sin\frac{\alpha}{2}$

And the project area of the tip on top surface of the specimen will be

$$A \approx 2t\left[\frac{R}{\cos(\frac{\alpha}{2})} + (D - R)\tan(\frac{\alpha}{2})\right], \qquad (2.10),$$

where t is the thickness of the TEM specimen as illustrated in figure 2.11.

Therefore, once the specimen foil thickness t and indentation depth D are taken into account, the mean stress, σ, can be calculated by plugging equation (2.10) into (2.11) as illustrated in equation (2.12)

$$\sigma = \frac{F}{A} \qquad (2.11),$$

$$\sigma = \frac{F}{2t\left[\frac{R}{\cos(\frac{\alpha}{2})} + (D-R)\tan(\frac{\alpha}{2})\right]} \qquad (2.12)$$

Finally, maximum stress could be calculated in equation (2.13)

$$\sigma_{\max} = \frac{F}{2t\left[\frac{R}{\cos(\frac{\alpha}{2})} + (D-R)\tan(\frac{\alpha}{2})\right]} \times \frac{3}{2} \tag{2.13}$$

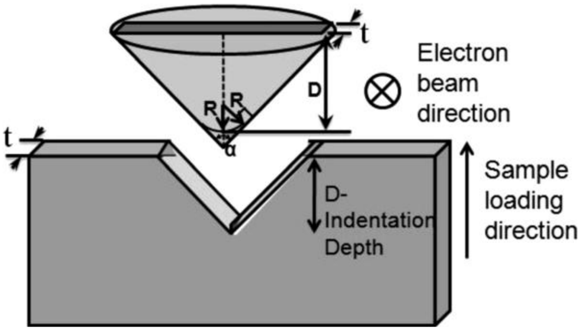

Figure 2.11. A schematic diagram illustrates alignment of TEM specimen and nanoindenter tip, including the positions of the specimen, the electron beam, and the (conical) nanoindenter tip and the specimen moving direction [108, 109].

2.4. X-ray diffraction

X-ray diffraction (XRD) is one of the most widely used nondestructive crystal structure analysis technique as providing the lattice constant and orientation of the crystal. Especially, application for the thin film materials can help to identify the strain effect along the interface between the film and substrate, which may suggest more detailed study of the defects in the the film. Figure 2.12 shows the schematic set up of X-ray spectrometer. For the operation, there are couples of factor to be noted. First, incident direction of the x-ray beam should be orthogonal to the surface of the reflecting plane. Second, the incident beam and diffracted beam should form angle 2θ. In the schematic, once the incident beam diffracted by the plane surface, the diffracted beam could be measured by the detector D as rotating with a certain angle respect to sample position C.

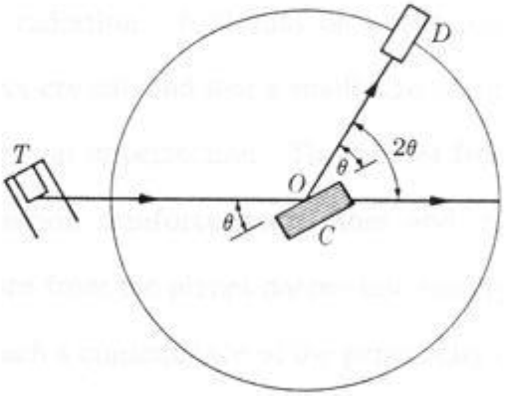

Figure 2.12. Schematic diagram of X-ray spectrometer [110].

Basic operation mechanism of this technique can be explained based on the Bragg's law as shown below:

$2d \cdot \sin\theta = n\lambda$ (2.14)

Once the parallel and monochromatic X-ray beam presents on the surface of material with a certain wavelength (~ 1.540Å) along variation of angle of incident beam, the incident beam is diffracted by a set of crystal planes spaced with d along a certain direction. And high intensity of a peak for the plane could be resulted at a corresponding angle θ based on the Bragg's law. Finally, based on the peak value, the crystal structure of the material could be characterized. Particularly, the information from the width and degree of the intensity peak could be essential enough to determine the crystallinity of the material based on the size of its unit cell.

There are several factors introducible affecting on the variance of peak width. First, due to the wave destructive interference resulted from periodicity of atomic arrangement, the width of the diffraction peak could increase as the reduction of crystal thickness. Figure 2.13 shows effect of particle size on the width of the peak. Based on this diagram, size of the particle can be estimated by $\mathrm{t} = \frac{0.9\lambda}{\mathrm{B}\cos\theta_{\mathrm{B}}}$ since the width of the peak, B, is defined as the difference between $2\theta_1$ and $2\theta_2$.

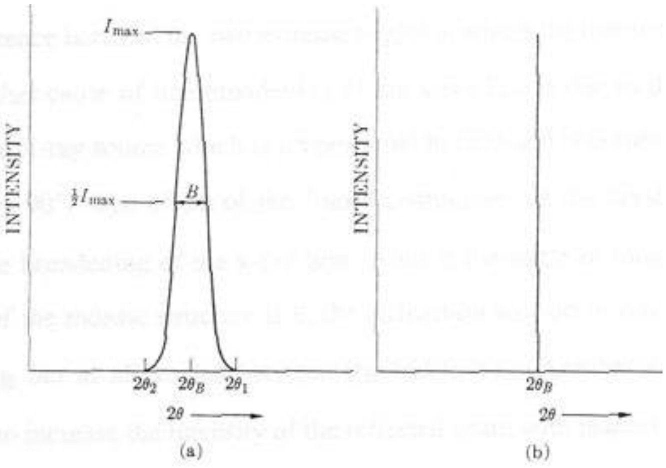

Figure 2.13. Plots show effect of particle size on the peak width [110].

Another possible reason for the variance of the peak width is from the relationship between the spectral width of the x-ray source and diffracted angle θ. The term of “spectral width” can be rephrased as the wavelength width or wavelength interval. And because such wavelength width from the source is proportional to tanθ, as the θ is closer to 90°, increase of the peak width can be caused by misorientation of “checker” structured crystal of a material. For example, once the angle for misorientation between the crystal blocks is defined as ε, the diffracted peak at θ for the single crystal will be broadened up to $\theta + \varepsilon$. Additional to the variance of the peak width, the intensity of the peak could also be affected by the “checker” structured crystal. In other words, the peak intensity is highly affected by the crystallinity of the material. Once the atomic arrangement is irregular, the constructive and destructive interference won’t be come out due to random phase. And then, the intensity of the x-ray beam can be estimated by the summation of all the x-ray intensities scattered. For example, the intensity of the refracted beam as scattered can be formulated with NA^2, where N is the number of scattered rays and A is amplitude of the rays. However, once the beam hits the well-oriented crystal, and the refracted beam could be explained based on Bragg’s law, the intensity of the beam could be reformulated with N^2A^2, where NA is the amplitude of the rays instead of A. Therefore, a material with high crystallinity can have higher intensity than that with low crystallinity or amorphous state.

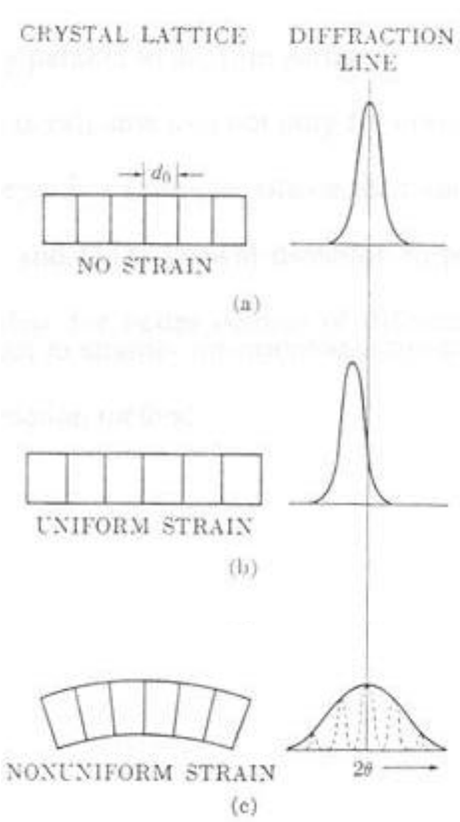

Figure 2.14. Plots describe the effect of lattice strain on the peak width, intensity and position [111].

Additional to the information about the size of grain and crystallinity of materials, X-ray diffraction technique can also analyze the strain effect of the grain or thin film based on the peak position along with the crystallinity as illustrated in Figure 2.14. Once a uniform tensile strain is felt by the film or grain, the d-spacing of the material can be larger than its bulk value. On the other hand, the materials are under a uniform compressive strain, the d-spacing can become smaller. Therefore, the corresponding peak position could be shifted to the lower angle under the tensile strain and the higher angle under compressive strain (Figure 2.14b). However, as the thin film is under non uniform strain with which the top area of the film is under the tensile strain and the bottom area near the interface between the film and substrate is under the compressive strain, XRD peak shows the increase of the width with lower intensity caused by the imperfect crystal orientation (Figure 2.14c). Then only preferred orientation which is perpendicular to the beam direction can contribute the peak intensity.

2.5. Pulsed laser deposition system

Since laser assisted thin film deposition was initially carried out in 1960s, and Dijkkamp and Venkatesan demonstrated deposition of $YBa_2Cu_3O_7$ as a high temperature superconducting material by laser deposition method in 1987 [112], currently pulsed laser deposition (PLD) system is applied for high quality thin film fabrication. PLD is one of the physical vapor deposition systems for thin film processing. Basic operational mechanism for this system is mainly depending on the laser ablation after the pulsed laser hits the surface of the target material inside of vacuum chamber. Once the pulsed laser strikes the target material, the evaporated materials from the target can fly through the plasma plum and deposit on the surface of the substrate. Thus, because the film deposition is carried out directly by the laser process, this technique is relatively simpler than other methods. For the film processing, high vacuum condition in the chamber is required. Before the deposition, backing pressure of the chamber should be reduced up to 10^{-7} mbarr range. And the pressure can be controlled by the mechanical and turbo molecular pumps. Once the laser is on operation, the high spatial coherent beam of the lasers allows extreme focusing and directional irradiation with high energy densities. With such a monochromatic laser light, it can be possible to have narrow band excitation of the laser. And the pulsed excitation of the laser maintains the transient resolution. Then, based on these capabilities, PLD system shows several advantages over other deposition techniques such as evaporation or chemical vapor deposition methods. First, PLD can produce the high quality stoichiometric films with complex composites, maintaining the low contamination levels. And almost all metals and complex ceramic materials can be processed. Multi-targets can be used to grow single or multi layer thin films. During the deposition, extra gases such as O_2 or N_2 can be introduced as maintaining the film stoichiometry of oxides and nitrides. Finally, the film property can be variable by the *in situ* control. Therefore, based on these advantages, different thin film properties can be achieved.

The schematic diagram of the PLD experimental setup is illustrated by the figure 2.15. In the chamber, multiple target holders are located face to face with the substrate holder. The targets could be mounted on the target holders at which the surface of the target is 45° tilted respect to the incident direction of the excimer laser beam. Once a high power laser strikes the target through the optical focusing lens, it can generate the heat energy to vaporize the target materials. Under the laser ablation, through the plasma plum, the evaporated materials can travel onto the surface of the substrate attached on the substrate holder positioned about 3~5 cm away from the surface of the target. During the thin film deposition, the substrate temperature can be changeable in the range between room temperature and 800 °C.

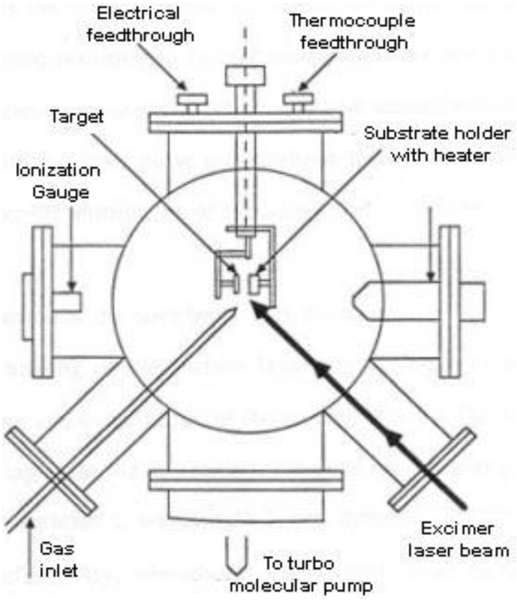

Figure 2.15. Schematic diagram illustrates the laser physical vapor deposition system [113].

There are several parameters to affect the quality of the thin films such as repetition rate of the laser pulse, substrate temperature, laser energy density, distance between the target and substrate and partial gas pressure of the chamber. Especially, presence of the partial gas in the chamber highly affects the surface coverage of the plume. For example, under high partial gas pressure, the mean free path of adatom from the plume can be reduced after it collides with the partial gas atoms. Then the plum can cover the relatively small area of the substrate. Meanwhile, as the mean free path of the adatom increases under high vacuum condition, the plume can cover the larger area of the substrate. Therefore, under such various deposition conditions of PLD system, growth of different structures of the thin films is possible. However, in spite of the fact, in order to comprehend the mechanism of PLD processing, study of interaction between the laser and target is inevitable. And the interaction during the laser ablation should be explained based on physical phenomenon with equilibrium and non-equilibrium processes which can be decided by the physical properties of laser and target materials. Once the pulsed laser beam strikes the target, laser radiation can be absorbed by the target surface. Then, as electromagnetic energy transferred from the laser to target, it can be converted to different forms of energy source, such as electronic excitation, thermal, chemical and mechanical energies, to evaporate the target material. During the evaporation, usually other processes such as ablation, excitation, plasma formation and exfoliation are accompanied. Eventually, these processes generates a plasma plume resulted from a mixture of energetic atoms, molecules, electrons, ions, clusters, micron-sized solid particulates and molten globules. The short mean free path after the collision between the species results in the rapid expansion of the plum from the target surface.

To further understand the mechanism of the plum formation, detailed descriptions of the formation of the plume during the laser-target interaction is shown in figure 2.16. Once a laser pulse initiated on the target surface with its intensity of $I_0 \cdot \exp(-\alpha)$, the interaction process can be explained with three different steps until a plum formed within a few nanosecond. On the first step, as starting with the laser pulse, the target materials can be evaporated as resulted from the interaction between the laser and target. During the second step, further interaction between the evaporated materials and laser enhances the formation and expansion of the isothermal plasma. Finally, during the third step, the plasma can expand anisotropically under adiabatic condition. This step is initiated at the end of the pulse.

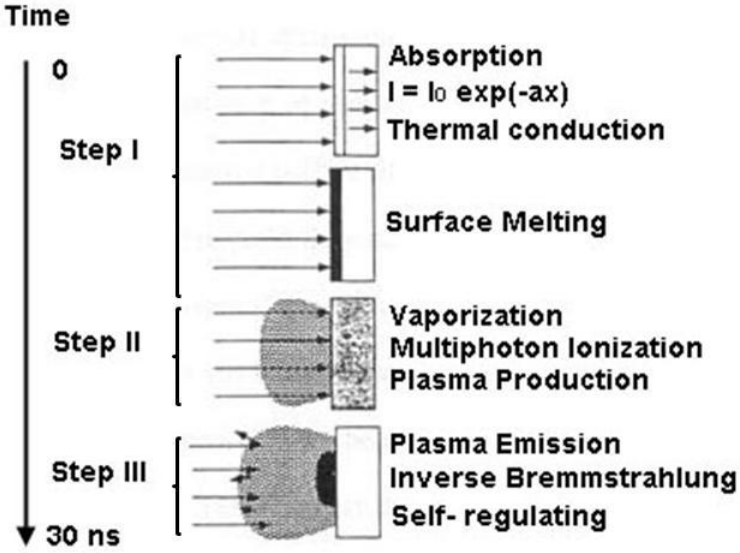

Figure 2.16. Schematic diagram illustrates different steps of laser target interactions during laser pulse along time variation (ns) [114].

2.5.1. Interaction between the laser beam and target

As the laser–target interaction initiated, the beam with intensity of $I_0 \cdot \exp(-\alpha)$ can be absorbed by the target up to the depth of x. Then, the high electromagnetic energy of the laser pulse is transferred to the different energy forms to generate the heat to melt and evaporate the materials from the target surface layer. Usually, the heating, melting and evaporation rate with the pulsed laser rely on the parameters of the laser and properties of the target materials. The laser parameters include the laser energy density, pulse duration (frequency of the pulse), wavelength of the laser and shape of the laser pulse. For material properties, optical reflectivity, absorption coefficient, heat capacity, thermal conductivity, density, etc. can be explained. Such heating and melting effects of the laser beam govern the heat flow through the target. Thermal diffusion distance defined as $2(Kt)^{1/2}$ explains how far the heat can transfer with the spreading time of t and diffusivity, K. And during PLD processing, heat flow through the target can be explained by the equation (2.15) shown below:

$$\rho_{i(T)} c_{p(T)} \frac{\partial T(x,t)}{\partial t} = \frac{\partial}{\partial t}\left[K_i(T)\frac{\partial T(x,t)}{\partial x}\right] + I_0(t)[1 - R(T)]e^{-a(T)x} \qquad (2.15),$$

where x and t are the distance normal to the surface of the sample and the time. $P_i(T)$ is density, $C_p(T)$ is thermal heat capacity, R(t) is the reflectivity, and a(T) is the absorption coefficient and I0(t). $P_i(T)$, $C_p(T)$, R(t) and a(T) are all temperature dependent functions. $I_0(t)$ is the intensity of the incident laser. The term of $K_i(T)$ is for the thermal conductivity. Depending on the values of subscript, i, which stand for solid (when i=1) and liquid (when i=2) phases, the K value can be varied by the state of the different material phases. Based on this equation, the prediction of the heat transfer through the target material is possible.

As the evaporation after the melting of the target material proceeding, the position of the target surface can be changeable. Therefore, based on the energy balance approach, it can be possible to calculate the amount of the evaporated material by the laser pulse which can be considered similarly as the amount of the energy needed for the film deposition without any energy loss between two procedures. The balance equation can be explained with the equation (2.16) given by:

$$\Delta x_i = \frac{(1-R)(E-E_{th})}{(\Delta H+C_v\Delta T)} \qquad (2.16),$$

where Δx_i is change of thickness of the target after evaporation, R is the reflectivity, ΔH is the amount of the heat absorbed by unit mass, C_v is heat capacity under constant volume, and ΔT is the change of the temperature. And the threshold energy E_{th} stand for the minimum energy required for the evaporation. This equation can be only applied for the case with shorter absorption length than that of the thermal diffusion within in the target material.

2.5.2. Interaction of the laser beam with evaporated materials

After the materials from the target are evaporated, as the evaporated materials still on the way of the laser path, further interaction of these species with the laser could be expected. Once the laser beam strikes the target surface, the temperature of the surface layer can be significantly increased (> 2000K). Then positive ions and electrons can be emitted from the surface. Such phenomenon of these species emissions could exponentially increase about the increasing temperature. And it can be estimated by Langmuir-Saha equation (2.17) shown below:

$$\frac{i_+}{i_0} = \frac{g_+}{g_0} e^{[(\phi-I)KT]} \qquad (2.17),$$

where i_+ and i_0 are fluxes of positive and neutral ions emitted from the surface at a certain temperature of T. g_+ and g_0 are the weights of the ions which are on the ionic and neutral states. *f* is the work function of the electron. And *I* is the material ionization potential. Based on the equation, under condition of $I > \phi$, the flux of the neutral ions will exponentially increase with increase of the temperature. Such higher temperature can be achieved after interaction of the evaporated species with the laser resulting in the plasma formation. Electron-ion density, temperature and wavelength of the laser can decide how laser beam can penetrate and be absorbed by the plasma. And the plasma frequency can decide whether the incident laser can be reflected or penetrate the plasma. This frequency can be formulated as $f_p = 8.9 \times 10^3 n_e^{0.5}$, where n_e is the concentration of the electrons in the plasma. For the transmission and further absorption process of the laser beam, the plasma frequency should be lower than that of the laser beam.

The primary absorption mechanism for plasma is based on the electron-ion collisions. Once a photon is absorbed by the free electron, the absorption process can occur under which the absorption coefficient is expressed by the following equation (2.18):

$$\alpha_p = 3.69 \times 10^8 \left(\frac{z^3 n_i^2}{T^{0.5} f^3}\right)\left(1 - e^{\left(-\frac{hf}{kT}\right)}\right) \qquad (2.18),$$

where z, n_i and T are the parameters of the plasma, i.e. average charge, ion density and temperature. h is the Plank constant, f is the frequency of the laser and k is Boltzmann constant. The term of $\left(1 - e^{\left(-\frac{hf}{kT}\right)}\right)$ stands for decay of the processing due to the emission. Therefore, based on the equation (2.18), it can be explained that the heating of the evaporated materials by the absorption of laser radiation is highly relying on the concentration of ion, temperature of plasma, wavelength with the frequency of the laser.

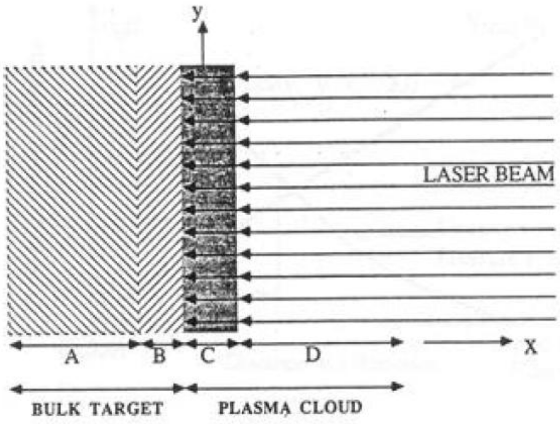

Figure 2.17. Schematic diagram shows presentation of different phases during the interaction of laser beam with the target surface [114].

Figure 2.17 shows a schematic diagram of the interaction of laser beam with the target surface. In the diagram, it is shown that the four different regimes exist during the laser processing by the separation with different phases. The first regime marked by 'A' illustrates the area of the bulk target which has not been affected by the laser beam. The second regime 'B' stands for the target surface area in which laser can penetrate and materials can evaporate. The next regime of 'C' shows the area adjacent to the target surface in which the dense plasma can absorb the laser radiation. Finally, in the regime 'D', expansion of the plasma plum can exist, which is transparent to the laser beam.

2.5.3. Adiabatic plasma expansion and film deposition

After the pulse of laser, no more laser energy absorption by the target transfers particles from the target to the plasma plum. Then under adiabatic condition, anisotropic expansion of the plasma plume can be enhanced, which can be explained by the relation as shown below:

$T[X(t)Y(t)Z(t)]\gamma^{-1} = const$ (2.19),

where γ is the ratio of the specific heat capacities at constant pressure and volume. During the adiabatic regime, the conversion of the thermal energy into the kinetic energy can occur as the plasma expanded under high velocity. Therefore, the dimension of the plasma which initially has larger size along X and Y direction than Z direction can be expanded along the Z direction with increase of the velocity under adiabatic condition.

CHAPTER III

GRAIN AND GRAIN BOUNDARY ACTIVITIES OBSERVED IN ALUMINA-ZIRCONIA-MAGNESIA SPINEL NANOCOMPOSITES BY *IN SITU* NANOINDENTATION IN TRANSMISSION ELECTRON MICROSCOPE*

3.1. Overview

At room temperature, *in situ* nanoindentation experiments in a transmission electron microscope reveal the grain and grain boundary activities in fully dense ceramic nanocomposites composed of Al_2O_3 : ZrO_2 : $MgAl_2O_4$ (AZM) processed by spark plasma sintering (SPS). The composites have a bi-modal grain size distribution, where the larger grains (500 nm – 1 μm in diameter) consist of Al_2O_3 and $MgAl_2O_4$ grains, and the smaller grains (100 – 300 nm in diameter) are primarily ZrO_2. *In situ* dynamic deformation studies show that the AZM nanocomposites undergo the deformation mainly through the grain-boundary sliding and rotation of small grains, i.e., ZrO_2 grains, and some of the large grains, i.e., $MgAl_2O_4$ grains. We observed both plastic and elastic deformations in different sample regions in these multi-phase ceramic nanocomposites at room temperature.

---

*Reprinted from "Grain and grain boundary activities observed in alumina–zirconia–magnesia spinel nanocomposites by *in situ* nanoindentation using transmission electron microscopy" by J. H. Lee, I. Kim, D. M. Hulbert, D. Jiang, A. K. Mukherjee, X. Zhang, H. Wang, Acta Materialia 14 (2010) 4891. Copyright (2010), with permission from Elsevier.

3.2. Introduction

Nanostructured ceramic materials have demonstrated superior performance and are capable of meeting requirements of structural materials in wide applications [115-117]. More importantly, ceramic nanocomposites that combine multi-functionalities from different constituents demonstrate an outstanding combination of physical properties [23-25]. Although ceramics usually have very high hardness, they exhibit low fracture toughness and poor machinability. In the past decade, a significant amount of work has been done to further enhance the strength and fracture toughness of ceramic materials. Initial work by Niihara suggests that, by incorporating nanosize dispersions within the matrix grains and at the grain boundaries, significant enhancement in mechanical properties can be achieved at both room temperature and high temperatures [7]. The ceramic nanocomposites show significantly improved toughness by 50-100% or higher, and an increase in hardness of three to five times depending on systems at room temperature. It was reported that these composites are toughened primarily by crack deflection due to nanosize particles within the matrix grains. Following this pioneering work, several other ceramic nanocomposites with enhanced fracture toughness and hardness have been demonstrated [118-120]. Recently spark plasma sintering (SPS) has been introduced to produce ceramic nanocomposites with enhanced fracture toughness at a lower sintering temperature and for a shorter time than conventional sintering techniques [121, 122, 28]. As the grain size decreases at lower sintering temperature and shorter sintering time, the strain rate during plastic deformation can be enhanced based on the Mukherjee-Bird-Dorn Equation as follows [123].

$$\dot{\varepsilon} = A\frac{D_0 G b}{kT}\left(\frac{b}{d}\right)^p\left(\frac{\sigma}{G}\right)^n e^{-Q/RT} \qquad (3.1)$$

where G is the elastic shear modulus, b is the Burgers vector, k is the Boltzmann's constant, T is the absolute temperature, d is the grain size, p is the grain-size dependence coefficient, n is the stress exponent, Q is the activation energy, D_0 is the diffusion coefficient, and R is the gas constant.

Several conventional methods such as high temperature tensile testing, X-ray diffraction (XRD) analysis, and scanning electron microscopy (SEM) have been used to analyze the deformation mechanisms of ceramic nanocomposites [20, 124, 125]. However it is quite difficult to determine the deformation mechanism(s) explicitly without a direct observation of the microstructural evolution during deformation. Recently, *in situ* nanoindentation in the column of transmission electron microscope (TEM) has been developed to examine material deformation mechanisms, mainly in metallic samples including Al [126] and Ni [127]. *In situ* nanoindentation on ceramic materials is rare [94].

In this study, we have conducted an *in situ* nanoindentation study on alumina-zirconia-magnesia spinel (Al_2O_3-ZrO_2-MgO, AZM) nanocomposites prepared by SPS to explore the deformation behavior of ceramics nanocomposites. This system has been previously shown with high-strain-rate superplasticity at high temperatures because of its unique multiphase structure [20]. Later, fully dense and porosity-free AZM nanocomposites were demonstrated by using SPS technique [128, 46]. It is important to further understand the deformation and energy-dissipation mechanisms through the grain and grain boundary activities in the multi-phase structures. Detailed conventional TEM analyses and *ex situ* nanoindentation studies were performed prior to the *in situ* TEM work.

3.3. Experimental

Fully dense AZM nanocrystalline ceramics consisting of four parts ZrO_2, three parts Al_2O_3, and three parts $MgAl_2O_4$ by volume were processed by SPS. The superplastic forming was carried out at a temperature of 1150 ºC and a strain rate of 10^{-2} s^{-1}. During SPS, the samples were superplastically deformed to a special form by a die set. Shear (area a) and compressive (area b) stress regions were created and cut for TEM specimens as illustrated with inset in Figure 3.2b. Multiple TEM specimens from both regimes were prepared through a conventional method including cutting, grinding, polishing, and ion milling. Conventional TEM and energy-dispersive X-ray spectroscopy (EDX) mapping were conducted on the samples to resolve the microstructure and composition of the nanocomposites. *In situ* nanoindentation was conducted using an *in situ* nanoindentation holder manufactured by NanoFactory, Inc. The samples were controlled in three dimensions (3D) by a piezoelectric actuator. Both conventional TEM and *in situ* TEM analyses were conducted within a JEOL2010 analytical electron microscope with a point-to-point resolution of 0.23 nm. Images and movies during indentation events were captured using a built-in CCD camera in the microscope. Within the TEM column, the indentation experiments were performed using the nanoindentation tips made of diamond in both conical (tip radius ~100 nm and tip angle ~ 70°) and standard Berkovich (tip radius ~100 nm and tip angle ~ 142.3°) geometries. The sharp conical shape tip was used for performing nanoindentation on specific grains or positions in the sample and both the conical- and the standard Berkovich-shape tips were used for standard load-displacement measurements. *In situ* movies and TEM images were taken during the nanoindentation experiment. The detailed indentation experiment set-up (with a conical-shape indentation tip) is illustrated in Figure 3.1. During the indentation experiment, the nanoindentation tip was stationary while the sample was driven closer to the tip by a piezoelectric stage in a precision movement as fine as 0.1 nm per step. During the loading process, a constant loading rate of 10 nms^{-1} and a holding time of 15 ms were used for all the indentation experiments. A standard nanoindentation holder manufactured by Nanofactory, Inc. can reach a maximum load of 1000 μN and a maximum loading depth of 700 nm. For most of the experiments in this study, a maximum depth of 250 nm and a maximum load of 200 μN were set to avoid tip damage. Prior to the *in situ* nanoindentation work, a detailed conventional nanoindentation study was performed by a Hysitron nanoindentor at a constant load mode.

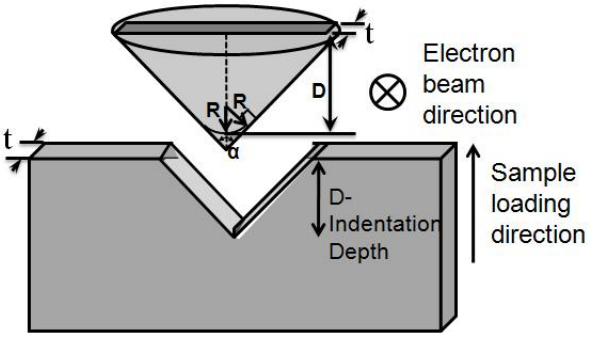

Figure 3.1. A schematic diagram illustrates *in situ* nanoindentation experimental setup, including the sample, electron beam and naoindenter tip (a conical-shape tip) positions, and sample moving direction.

3.4. Results and discussion

Figures 3.2a, b, and c, d, show the bright field TEM images of AZM samples cut from the compressive and the shear regions, respectively. In the low magnification TEM images (a, c), it is clear that, in both cases, all of the grains are elongated along a certain direction, which is identified as the deformation direction during the SPS process (marked by arrows in the figures). More interestingly, these samples show an obvious bi-modal grain size distribution, as shown in Figure 3.2e. The large white grains (grains with bright contrast in the images), further identified to be either Al_2O_3 or $MgAl_2O_4$ with grain size ranging from 290 nm to 1.1 μm (an average grain size of 830 nm), are aligned along the elongation direction and are surrounded by the small black grains (grains with dark contrast in the images), ZrO_2 with an average grain size of 220 nm (Figure 3.2e). Figures 3.2 b and d are taken at higher magnification to resolve the grain boundary structure between the white/large and black/small grains. An important nature of the samples is that very little or no porosity is observed at the grain boundaries from either region; which resulted from its unique grain arrangement and multi-phases. This also suggests that the samples are fully dense, ideal for conducting *in situ* nanoindentation studies. The ZrO_2 grains are arranged as a "necklace" pattern surrounding several elongated large Al_2O_3 and $MgAl_2O_4$ grains. It is likely that, during SPS process at elevated temperatures, the small ZrO_2 grains undergo sliding and rotation to facilitate the deformation and realignment of the large Al_2O_3 and $MgAl_2O_4$ grains.

To confirm the composition of the grains, EDX mapping studies were performed on AZM composites cut from the compressed regions and an example is given in Figure 3.3. The image covers a grain boundary area between several small black (Yttria-stabilized ZrO_2, YSZ) grains and a large white ($MgAl_2O_4$) grain (Figure 3.3). Each map corresponds to one element of interest. Based on the EDX scans, it is clear that the large hexagonal shaped grain corresponds to the Al- (3a), Mg- (3b) and O- (3c) rich area which is identified as a $MgAl_2O_4$ grain. The surrounding grains are Zr- (3d), Y- (3e) and O- (3c) rich and identified as ZrO_2 grains. Most of the elements are uniformly distributed in the grains without any grain boundary segregation. The overall composition analysis is consistent with the above microstructural analysis.

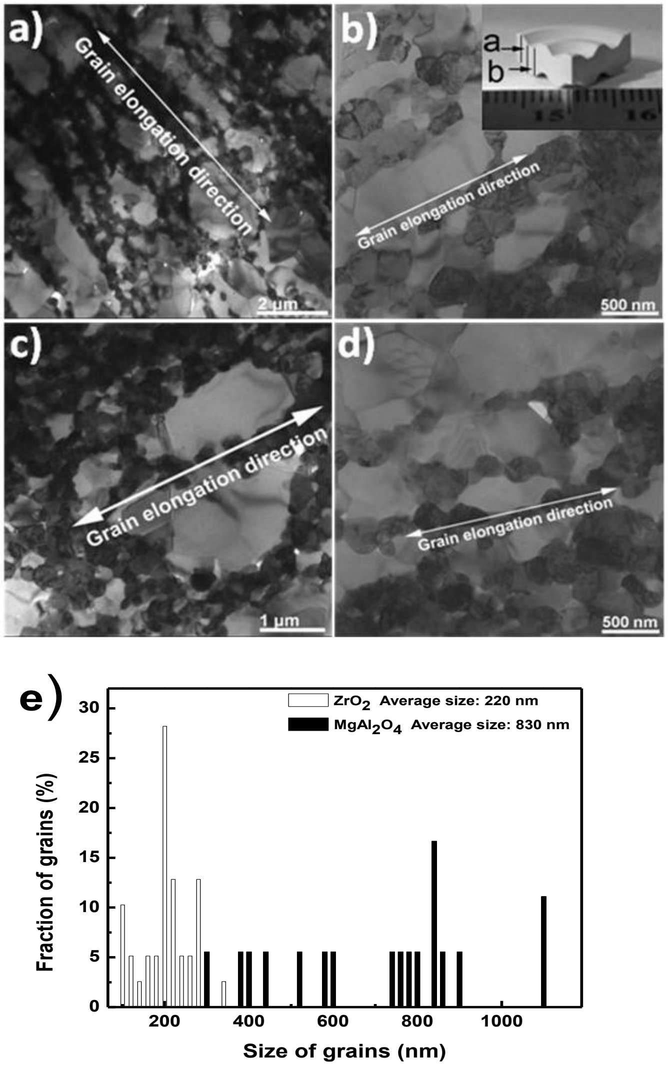

Figure 3.2. a) Low magnification TEM image and b) enlarged image of a specimen cut from the compressive region. c) Low magnification TEM image and d) enlarged image for a specimen cut from the shear region. Insert shows a SPS processed AZM bulk sample where "a" and "b" regions were under shear and compressive stress, respectively, during SPS process. e) Grain size distribution of Al_2O_3 and $MgAl_2O_4$, and ZrO_2 grains (AZM) shows a clear bi-modal distribution.

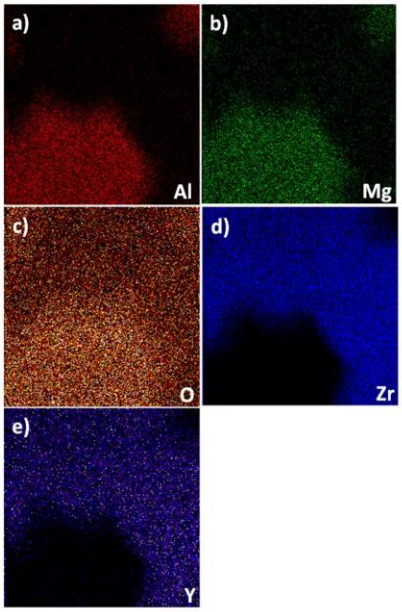

Figure 3.3. EDX mapping indicates a hexagonal $MgAl_2O_4$ grain is surrounded by small YSZ grains. Grain boundaries are quite clean and obvious without any obvious grain boundary intermixing.

Conventional nanoindentation was first performed on the samples from both the compressive and the shear regions. The nanoindentation experiments were performed under constant loads at 3000 and 5000 μN. Under both loads, the hardness of the samples ranges from 16 to 27 GPa. This is mainly due to the intrinsic hardness variation between the different components in the nanocomposite. Pure bulk Al_2O_3 usually has a high hardness ~ 30 GPa. ZrO_2 has a hardness of ~ 19 GPa [129]. The hardness of $MgAl_2O_4$ is around 2~3 GPa [130]. It is highly possible that the soft region (~16 GPa) is composed of a large amount of $MgAl_2O_4$ with other grains while the hard region (~27 GPa) consists of Al_2O_3 and ZrO_2 grains and less $MgAl_2O_4$ grains.

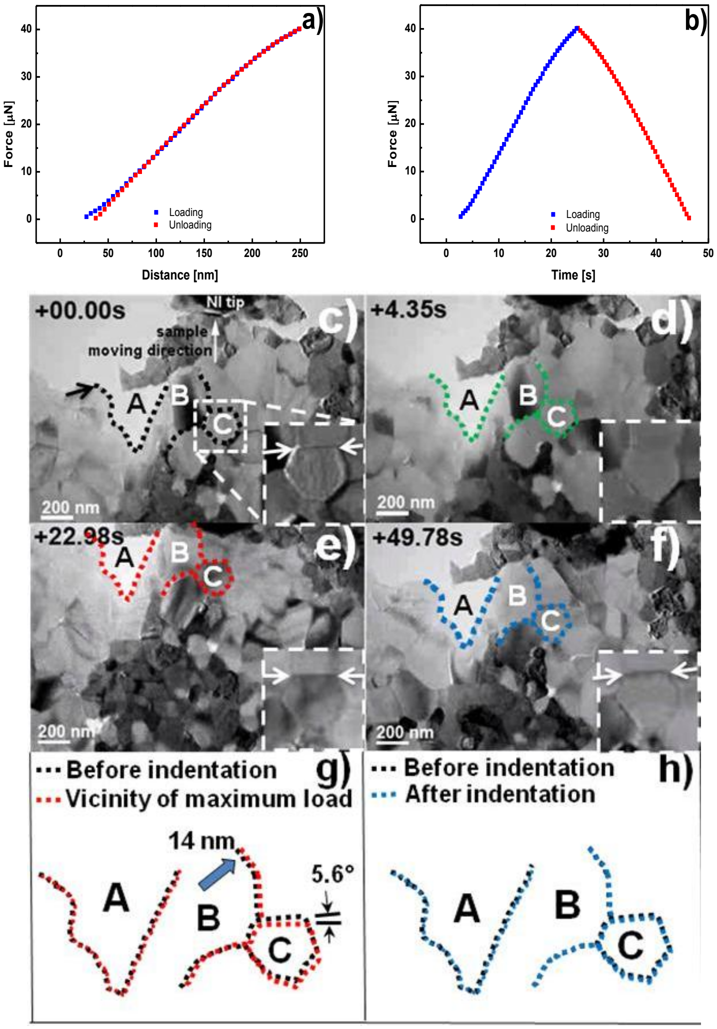

Figure 3.4. a) Force-displacement and b) force-time plots show elastic deformation. A series of movie frames shows an elastic deformation regime with a detailed analysis in grain boundary activities shown in: c) before indentation; d) during loading; e) at maximum load; f) after indentation, and the schematic comparison for; g) between before indentation and right before the maximum load and h) between before and after indentation. (Based on instrument specifications, the estimated measurement error of force is ± 5%.)

To understand the deformation mechanisms in nanocomposites with such bi-modal grain size distribution, *in situ* nanoindentation experiments were conducted in a TEM column using the experimental set-up illustrated in Figure 3.1. Based on the quantitative load-displacement measurement, similar to *ex situ* nanoindentation observations, we clearly identified hard and soft regions in the samples using the conical-shaped diamond tip. The hard regions are mainly associated with the small black grains (ZrO_2) and some of the large white grains (Al_2O_3) (corresponding to a maximum load of 40-45μN at a displacement of 200 nm), while the soft regions are mainly white grains ($MgAl_2O_4$) and some ZrO_2 grains with a lower load in the range of 20-30 μN at a displacement of 200 nm. These observations are consistent with our conventional nanoindentation results and support our hypothesis on the compositions of soft and hard regions.

During nanoindentation experiment, the activities of grains were captured by movies along with the quantitative load-displacement measurements in real time. By comparing the movies and the corresponding load-displacement curve, we can easily identify the deformation regions with either elastic or plastic deformation. We performed many of the indentation experiments at relatively thick regions to eliminate the concerns that thin sample regions could have local sample bending during indentation; which could result in a false interpretation. One typical experiment showing mainly elastic deformation is presented in Figure 3.4. The corresponding force-displacement (F-D) and force-time (F-T) plots are shown in Figure 3.4a and b. The loading process at a constant displacement rate continues up to 25 s with a maximum depth of 250 nm, followed by an unloading process at the same rate. First, the F-D and F-T plots (Figure 3.4a and b) show the nature of elastic deformation without any obvious slope change in this sample region. Figures 3.4c-4f are the selected snapshots during the complete loading-unloading experiment. The nanoindentation tip located near the upper center in the images and the direction of movement of the sample are labeled in Figure 3.4c. No sample bending was observed during the nanoindentation experiment. During the indentation experiment it was difficult to identify the grain boundary activities, which are mostly on the order of nanoscale. Therefore, the grain boundaries were color-traced and compared in each snapshot to identify the grain boundary activities. For example, in Figures 3.4c-h, three grains, A, B and C, are selected for analysis. For clear view, a magnified image of grain B has been inserted in each snapshot. Grain A is identified as a reference grain which shows no obvious change in shape and position during the indentation. Once the sample was in contact with the tip, the loading process started. From 0 to 25 s, 3.4c, d and e are under loading and from 25 to 50 s, 4f is under unloading process. Before indentation, obvious grain boundaries of grains B and C can be identified (Figure 3.4c). During the loading process, grain B slides up ~14 nm and the grain C rotates in clockwise direction about 5.6° from the reference (Figure 3.4c, e and g). The inserts of grain C also show clear grain rotation. Arrows in the inserts mark a particular section of the grain boundary in grain C. Based on the positions of the arrows, it is clear that the grain boundary has shifted and rotated. However after the indentation, the grains completely recovered, i.e. they moved back to their original positions (Figure 3.4c, f and h). This, again, suggests that grain rotation can sometimes recover and result in elastic deformation in certain areas of ceramic nanocomposites. Since the sample is moving during nanoindentation, conducting microdiffraction on a specific small grain or a group of grains becomes very difficult and the results might not be very conclusive, as most of the grains range in size from 100-200 nm. Therefore, we mainly focused on the image analysis for this study.

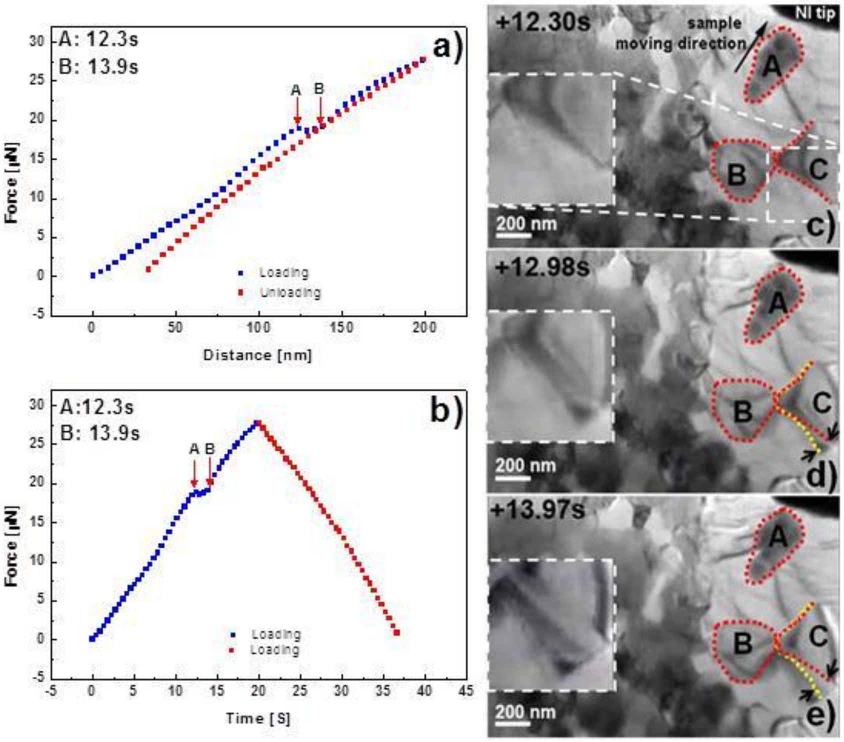

Figure 3.5. a) Force-displacement and b) force-time plots show a clear step and the corresponding TEM images at point a and point b. This clearly indicates a plastic deformation regime resulted by grain rotation and realignment. (Based on instrument specifications, the estimated measurement error of force is ± 5%.)

Similarly, we also identified a few areas with a clear indication of plastic deformation. One such example is shown in Figure 3.5. Here grain A went through little to no change in position. Therefore, grain A is considered a reference grain for the analysis. During loading, the F-D and F-T plots (Figure 3.5a and b) show a clear step from 12.3 s to 13.9 s which corresponds to a displacement at ~125 nm. For this experiment, the conical nanoindenter tip was positioned at the upper right corner in the images (marked in Figure 3.5c). At 12.3 s the snapshot image shows an obvious grain boundary around grain C (Figure 3.5c). Within this step period (Figure 3.5d, at 12.98 s), the width of the grain boundary of grain C increased significantly (the width change marked as arrows in Figure 3.5d and 5e) along with an obvious change in contrast. Enlarged images of the grain boundary of grain C are shown as an inset in Figure 3.5c-e to show the obvious change in grain boundary width. At 13.97 s the grain boundary width reached its maximum at the end of the step. This observation suggests that grain C starts to rotate in order to accommodate the stress induced by the deformation, which results in a local plastic deformation regime (i.e., the step regime) in the loading-unloading curve. The correlated qualitative and quantitative analyses clearly demonstrate that a small plastic deformation regime can exist in ceramic nanocomposites as a result of grain rotation and grain realignment to accommodate the load and deformation.

The maximum instantaneous pressure where the step occurred can be estimated from Equation 3.2 based on the Hertz contact model [107].

$$p = \frac{1.817}{\pi} F^{1/3} (\mathrm{E}^{*}/\mathrm{R})^{2/3} \tag{3.2}$$

Where F is the load, E* is the reduced modulus, and R is the radius of curvature of the indenter. Given the load ~18.0 μN at the step, the value of E* ~200 GPa measured by conventional nanoindentation and the tip radius of 100 nm, the estimated pressure at the step using Equation 3.2 is around 24.0 GPa. However this estimation did not take into consideration geometrical factors such as TEM foil thickness, which might result in an overestimation of the pressure value. If the sample foil thickness t and indentation depth D are taken into consideration, a geometry-based pressure analysis using the schematic illustrated in Figure 3.1 can be performed by applying Equations 3.3 and 3.4 below.

The mean stress, σ, is calculated by using

$$\sigma = \frac{F}{A} \qquad (3.3),$$

where F is the load (force) and A is the projected contact area. For the special geometry of a conical indentation tip and a thin TEM foil as illustrated in Figure 3.1, A is given as below,

$$A \approx 2t[\frac{R}{\cos(\frac{\alpha}{2})} + (D-R)\tan(\frac{\alpha}{2})] \qquad (3.4)$$

Where t is sample foil thickness, D is indentation depth, R is the tip radius, and α is the tip angle. The estimated mean stress is ~ 2.2 GPa with a measured load F of 18.0 μN, a tip radius R of 100nm, indentation depth D around 120 nm, foil thickness t of 30 nm, and a tip angle α of 70°. Using the Hertz theory of elastic contact, the maximum stress is 3/2 times the mean stress, ~ 3.3 GPa. This estimation is much smaller than the value calculated using Equation 3.2, and provides a lower bound for the real stress applied during *in situ* nanoindentation tests. In this analysis, bending of the TEM foil is not considered since bending is not detected in the current *in situ* studies. Our lower bound estimation using the geometrical analysis could be more reliable for the case of *in situ* nanoindentation study as the sample and tip geometry, indeed, play an important role in the overall pressure (stress) calculation.

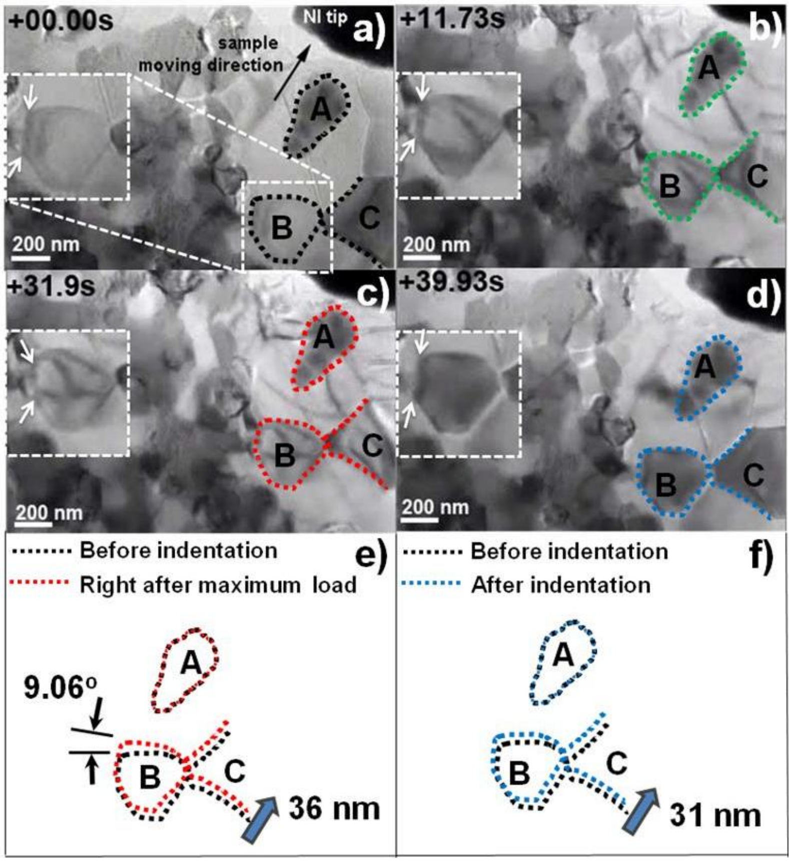

Figure 3.6. During indentation obvious grain rotation, grain-boundary sliding and plastic deformation were observed. A detailed grain boundary study has been performed to analyze the grain activities during deformation as shown in: a) before indentation; b) during loading; c) during unloading; d) after indentation, and schematic comparison for; e) between before indentation and after the maximum load and f) between before and after indentation.

To clearly identify the grain rotation and grain-boundary sliding, more detailed grain boundary analysis has been performed on the TEM movie frames in Figure 3.6. From 0 to 20 s, Figure 3.6a and 6b were taken during loading, and from 20 to 40 s, Figure 3.6c and 6d were recorded during unloading process. Figure 3.6c was taken right after the maximum load. About the reference grain A, the relative position between grain B and C did not change significantly during loading in Figure 3.6a and b. But after the maximum load (Figure 3.6c), grain B rotated by about 9.06^o clock-wise and grain C moved up by ~36 nm from its original position (Figure 3.6c and the corresponding grain diagram in 3.6e). After unloading was complete, as shown in Figure 3.6d and the corresponding grain diagram in 6f, both grains B and C have shifted up ~31 nm from their original position but the rotation of grain B was recovered. The grain boundary shift and grain rotation of grain B are enlarged as insets in Figure 3.6a-d. The arrows mark one particular section of grain boundary for grain B where obvious grain boundary activities were observed. For example, the marked edge of grain B in the inset of 6a became shorter during the loading process (inset in 6b), is the shortest at the maximum load (inset in 6c), and almost recovered to its original length when unloading was complete (inset in 6d). The length and position variation of grain boundary in grain B could be the sum of results from its grain rotation and grain-boundary sliding. This clearly demonstrates the grain boundary activities in ceramic nanocomposites by comparing the images from before (Figure 3.6a) and after indentation (Figure 3.6d) using grain A as a reference. It is noted that the grain rotation is essentially recovered after unloading process, whereas the grain-boundary sliding did not completely recover in this case.

Grain rotation and grain realignment have been previously reported in microcrystalline metals [131, 132] and nanocrystalline metals [133-135]. These grain activities were summarized as cooperative grain-boundary sliding and grain rotation phenomena in superplastic deformation, mainly observed in metals. The above *in situ* nanoindentation experiments suggest that the deformation in these ceramic nanocomposites, especially in certain local and specific sample regions with unique grain arrangements, shows the nature of elastic or plastic deformation at room temperature. The main deformation mechanism is the grain rotation and grain-boundary sliding, which is quite similar to that observed in metals [126, 127]. This is surprising as generally the plastic deformation regimes in ceramics are very short [136] and only observed at relatively high temperatures [20, 137]. However, the *in situ* nanoindentation experiments indicate that both elastic and plastic deformations occur in ceramic nanocomposites at room temperature.

It is noted that the plastic and elastic deformations were observed in different regions in the composites. This suggests that grain morphology and arrangement strongly affect the local deformation and energy dissipation mechanisms. For example, the cases illustrated in Figure 3.5 and 3.6 show a small amount of plastic deformation process and Figure 3.4 shows mainly elastic deformation. By comparing the grain structures in Figure 3.4-6, it is obvious that Figure 3.5 and 6 are in the regions where large white contrast grains (Al_2O_3 and $MgAl_2O_4$) were in direct contact with the indenter and only a few small grains were at the left corner of the images. These regions (Figure 3.5 and 3.6) were softer than the case in Figure 3.4. During indentation, the main contrast change and grain activities were found mainly in the large grains, e.g. grain B in Figure 3.6. It is also interesting to note that a relatively low pressure (~ 3 GPa, estimated by geometrical analysis) can trigger the grain boundary rotation and sliding events in a certain region. This observation of localized plastic deformation suggests that, at a certain location (Figure 3.5), the soft $MgAl_2O_4$ grains, e.g. grain B, may deform plastically and facilitate deformation in the form of grain rotation and sliding with neighboring grains. However, these soft $MgAl_2O_4$ grains are relatively large and the grain boundary activities were not fully recovered. In contrast, the region in Figure 3.4 has a unique "necklace" pattern with several large grains (Al_2O_3 and $MgAl_2O_4$) surrounded by many small grains (ZrO_2). The indenter tip was in direct contact with the small ZrO_2 grains. In Figure 3.4, the contrast variations were mainly observed in the black ZrO_2 grains, which suggests that ZrO_2 grains were highly active during the deformation process. In F-D curves in this region, we mainly observed elastic deformation. This, again, confirms our hypothesis that the unique "necklace" pattern helps in accommodating the load (the same as that during SPS process) and the small black ZrO_2 grains actively assisted in the deformation process and the flow of large Al_2O_3 and $MgAl_2O_4$ grains. More interestingly, this particular grain arrangement can fully recover after the deformation and grain boundary activities. The effect of ZrO_2 was proposed to play a major role in the accommodation of grain-boundary sliding, i.e., stress relaxation during high-strain-rate deformation in AZM nanocomposites [20].

Additionally, after indentation, no obvious crack or void was observed in the specimen. One explanation for this is that the sample is under compression during nanoindentation and, therefore, cracking or voiding is less likely to form in the ceramic nanocomposites. Other factors are the strain-relaxation from soft $MgAl_2O_4$ grains and the active grain boundary activities of ZrO_2 grains. This *in situ* study is direct evidence of the grain activities of the small ZrO_2 grains in the overall deformation process. Further analysis is under way to identify the best geometry and ratio of the AZM nanocomposite in achieving superplasticity.

3.5. Conclusions

Fully dense AZM ceramic nanocomposites were consolidated by SPS and prepared for the *in situ* nanoindentation experiment in a TEM column. Through conventional TEM study, we observed a unique "necklace" grain structure with bi-modal grain size distribution, where all the large white grains (Al_2O_3 and $MgAl_2O_4$) are surrounded by small ZrO_2 grains. Through *in situ* nanoindentation experiment, we monitored the grain activities during deformation. We found that in certain areas where a clear 'necklace' structure exists, the region mainly went through elastic deformation, i.e., the grains recover to their original alignment after indentation by the assistance of the strong grain activities in the small ZrO_2 grains. In other regions where mainly the hard Al_2O_3 and soft $MgAl_2O_4$ grains exist, a certain amount of plastic deformation was observed and the grains undergo a series of grain rotation, grain-boundary sliding, and realignment. This experiment demonstrates elastic and plastic deformation through grain and grain boundary activities in local grain areas of multi-phase ceramic nanocomposites at room temperature. This *in situ* study could provide useful insight for future designs of ceramic nanocomposites with superplasticity.

CHAPTER IV

DIRECT OBSERVATION OF TWIN DEFORMATION IN YBCO THIN FILMS BY *IN SITU* NANOINDENTATION IN TEM*

4.1. Overview

The deformation behaviors of $YBa_2Cu_3O_{7-x}$ (YBCO) thin films with twinning structures were studied by *in situ* nanoindentation experiment in a transmission electron microscope (TEM). The YBCO films were grown on $SrTiO_3$ (001) substrates by pulsed laser deposition. Both *ex situ* (conventional) and *in situ* nanoindentation were conducted to reveal the deformation of YBCO films from the directions perpendicular and parallel to the twin interfaces. Hardness measured perpendicular to twin interfaces is ~50% and 40% higher than that measured parallel to twin interfaces, by *ex situ* and *in situ*, respectively. Detailed *in situ* movie analysis reveals that twin structures play an important role in deformation and strengthening mechanisms in YBCO thin films.

---

*Reprinted from "Direct observation of twin deformation in $YBa_2Cu_3O_{7-x}$ thin films by *in situ* nanoindentation in TEM" by J. H. Lee, X. Zhang, H. Wang, Journal of Applied Physics 109 (2011) 083510. Copyright (2011), with permission from American Institute of Physics

4.2. Introduction

Since high temperature superconducting (HTS) $YBa_2Cu_3O_{7-x}$ (YBCO) was discovered in 1987, it has garnered extensive research interests in terms of both fundamental physics and potential applications [138, 139]. HTS YBCO thin film coated conductors have recently became one of the main research directions for YBCO-related research because of many envisioned applications including superconducting generator, motors, power cables, and other devices [57-59]. Despite their excellent superconducting properties, the poor mechanical property of YBCO thin films limits their industrial applications. Limited work has been done to explore the mechanical strength and toughness of YBCO through tensile and bending tests and *ex situ* nanoindentation measurement [140, 141]. It has been reported that twin structures in YBCO thin films enhance the overall mechanical performance, e.g., they provide a 25% enhancement in toughness [64]. Conventionally twin structures are observed in face centered cubic (FCC) metals with low stacking fault energy, such as Cu and Ag [142, 143]. Previous reports have shown that high density twin structures improve the mechanical strength of Cu [3,144,145] but have little or no impact on its electrical properties [146]. It was reported that the enhanced plastic deformation was observed in bulk Al via dislocation activities at the twin boundaries [147]. Different from monolithic metals, twins in YBCO, one of complex oxides, are formed because of the nature of orthorhombic structure, where $a = 3.82$ Å, $b = 3.89$ Å and $c = 11.68$ Å. The YBCO twins are formed along the (110) planes during the phase transition from tetragonal to orthorhombic phase simply by local oxygen diffusion [148, 63]. It is generally believed that twins, as one type of intrinsic defects in YBCO, act as effective pinning centers in YBCO thin films and enhance the superconducting properties in self-field and applied magnetic field [61, 149, 150, 151].

Although much has been done to study the effects of twins on YBCO's superconducting properties [60, 152], research exploring the effects of twins on its mechanical performance is scarce. Conventional nanoindentation and optical microscopy observation have been performed to show the effect of the twin structure on the mechanical properties in bulk YBCO [153, 154]. However, the strengthening mechanism(s) of twinning structures in YBCO is not yet well understood.

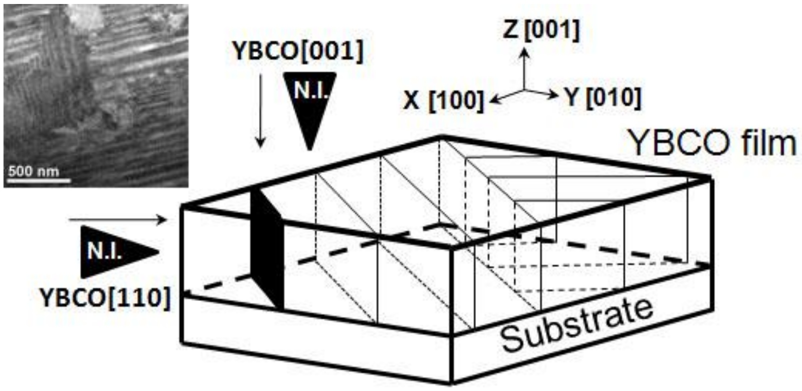

Figure 4.1. A schematic diagram describes the two different indentation directions (indentations have been performed on parallel with and perpendicular to the twin interfaces). The inset plan-view TEM image shows that YBCO twin interfaces have two orientations orthogonal to each other.

In this paper, we combined *ex situ* and *in situ* nanoindentation tools to explore the twin strengthening mechanisms in superconducting YBCO thin films. Both *ex situ* and *in situ* nanoindentation experiments were conducted either along $[001]_{\mathrm{YBCO}}$ (indentation direction parallel to the twin interfaces) or $[110]_{\mathrm{YBCO}}$ (indentation direction perpendicular to 50% of the twin interfaces and parallel to the other 50% of the twin interfaces) as illustrated in Figure 4.1.

4.3. Experimental

Depositions of YBCO films on $SrTiO_3$ (STO) (001) substrates were performed by pulsed laser deposition (PLD) with a KrF excimer laser (Lambda Physik LPX210i, λ= 248 nm, 10 Hz). The laser beam was focused to obtain an energy density of approximately 4 J/ cm^2 at a 45° angle of incidence. The films were grown to about 420 nm for *in situ* nanoindentation and 1 to 5 μm for conventional nanoindentation. The substrate temperature and oxygen pressure were fixed at 790 °C and 200 mTorr for all depositions. No post annealing was performed. The samples were tested for superconducting critical transition temperature (T_c) ranging from 90 to 92 K by ac susceptibility measurement and critical current density (J_c) in the range of 2.5 to 5.5 MA/cm^2 by transport measurement at 77 K to ensure that all the samples had good superconducting properties. Both plan-view and cross-section TEM samples were prepared through a conventional procedure, including mechanical grinding, polishing, and ion milling to be used for conventional TEM and *in situ* TEM studies. The conventional nanoindentation study was performed by a Tribo-nanoindenter manufactured by Hysitron, Inc. under a constant load mode. *In situ* nanoindentation was conducted using an *in situ* nanoindentation holder manufactured by NanoFactory, Inc. The sample is controlled in three dimensions by a piezoelectric actuator. Both conventional TEM and *in situ* TEM analyses were conducted on a JEOL 2010 analytical electron microscope with a point-to-point resolution of 0.23 nm. Images and movies during indentation events were recorded using a built-in CCD camera in the microscope. For *in situ* nanoindentation experiment, indentation experiments were performed with conical diamond tip (tip radius ~100 nm and tip angle ~70°) for standard load-displacement measurements within TEM column. *In situ* movies and image were taken during the loading and unloading processes under the experiment set up described in Figure 4.2. During the indentation experiment, the nanoindentation tip was fixed while the sample was moved toward the tip by a piezoelectric stage in a precision movement as fine as 0.1 nm/step. During the loading process, a constant loading rate of 10 nm/s and a holding time of 15 ms were used for all the indentation experiments. For most of the *in situ* experiments, a maximum depth of 200 nm was used to protect the tip from damage.

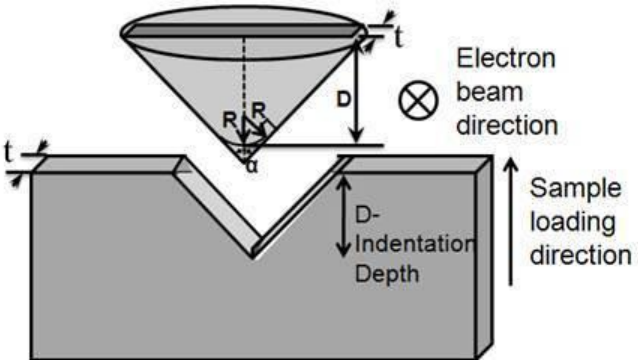

Figure 4.2. A schematic diagram illustrating the *in situ* nanoindentation experimental setup, including the positions of sample, the electron beam and the (conical) naoindenter tip and sample moving direction.

4.4. Results and discussion

The hardness of the YBCO thin films was measured with conventional nanoindentation in the directions perpendicular to [indentation on YBCO (110) plane] and parallel with [indentation on YBCO (001) plane] the twin interfaces. Figure 4.1 illustrates two different indentation directions on YBCO thin film with respect to the YBCO twin interfaces. When indenting on YBCO (001) planes (along $[001]_{\text{YBCO}}$), i.e. parallel to twin interface, there is no or minimal effect from twins. When indenting on YBCO (110) planes (along $[110]_{\text{YBCO}}$), i.e. perpendicular to 50% of the twin interfaces, we expect about 50% of the maximum effect from the twin interfaces. This is because of the two orthogonal orientations of the twins in YBCO, as illustrated in Figure 4.1. The inset is the plan-view TEM image of YBCO which clearly shows the two different orientations of the twin interfaces orthogonal to each other. Figure 4.3a plots the hardness data versus the displacement data for a series of *ex situ* indentation along the cross-section of YBCO film with a thickness of 5 μm, as illustrated in the inset. Despite the indentation depth varied from 50 to 150 nm, the hardness values are consistent for all regions. For region I and II (close to substrate-film interface), the mean hardness is around 11.9 GPa and 10.2 GPa, respectively. For region III and IV (film surface), where we begin to enter the thick YBCO film regime, the mean hardness drops to 7.9 GPa and 6.3 GPa, respectively. The softening effect is possibly occurs because (1) the porosity of the film starts to play a rule as the film gets thicker, and (2) the effect of twin interfaces become less dominant. To avoid potential substrate interference, the hardness of region II (around 10.2 GPa) is considered as the mean hardness of YBCO film when indenting on YBCO (110) planes. Figure 4.3b plots the hardness data of YBCO samples with different film thicknesses varing from 1.5 to 5 μm. The indentation direction is perpendicular to the film top surface, i.e. along $[001]_{\mathrm{YBCO}}$, as illustrated in the inset. The hardness was varied from 6.2 GPa for film with a thickness of 1.5 μm to 4.25 GPa with a thickness of 5 μm. The slight hardness reduction is possibly due to the surface porosity in the 5 μm film. However, for most of the films the hardness is about 6.2 to 6.5 GPa. Clearly the mean hardness value of 10.2 GPa with the indentation on YBCO (110) planes is much larger than that for the cases of indentation on the YBCO (001) planes (6.2 GPa). This significant hardness enhancement when loading along [110] direction suggests that the twin interfaces are very effective in strengthening the YBCO films, presumably by blocking the transmission of dislocations in the matrix. Several previous studies in bulk YBCO show that the indentation hardness on YBCO(110) increased about 4% to 7% compared with the hardness values on YBCO (001) [64 , 155]. However the reported twin interface effect is very small compared with our reported value here in YBCO thin films, which shows an increase of more than 50%. A possible reason for the difference in the effect of twins in bulk and thin film YBCO is the different density of the twins. Thin film YBCO has much higher twin density, with a small twin spacing ranging from 10 to 100 nm, while bulk YBCO has a much lower twin density, with twin spacing in the range of few microns.

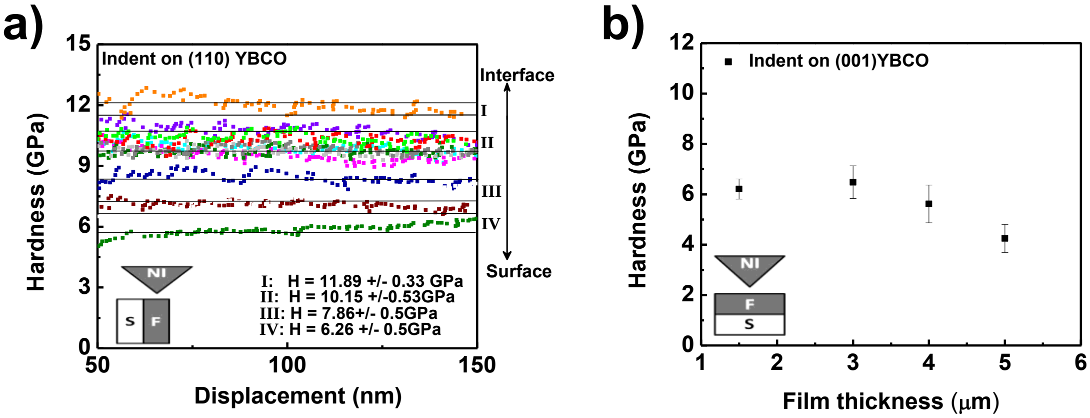

Figure 4.3. a) For the conventional indentation on YBCO (110) plane, hardness measurements are plotted along different indentation depths and different indentation positions from the interface between the film and the substrate. b) After indentation on YBCO (001) plane with different thicknesses, various hardness values are plotted relative to different film thickness. Insets illustrate different indentation directions with regard to film structure.

To fully understand the effect of twins on the deformation mechanisms, *in situ* nanoindentation on YBCO samples has been performed in TEM column. Similar to the above *ex situ* nanoindentation experiments, we conducted the *in situ* nanoindentation along two directions, i.e. indenting on both YBCO (110) planes and (001) planes by preparing the YBCO TEM foils in two specific orientations as illustrated in the insets of Figure 4.4. The loading process at a constant displacement rate continues up to 30 s and is followed by an unloading process at the same rate. A set of typical force-displacement plots along two directions is shown in Figure 4.4, representing data after the loading-unloading experiments. The force for indentation on (110) plane increases up to ~70 μN, whereas the maximum force for indentation on (001) plane is ~50 μN, with the maximum loading depth of 150 nm for both cases. Overall, there is about 40% enhancement in the maximum force for the case of indenting on (110) plane as compared with the case of (001) planes. Apparently indentation on YBCO (110) planes is harder than that on (001) planes, which again confirms that twin interfaces play an important role in the overall deformation mechanism of the film. During the unloading process for the case of indentation on (001) plane, the plot decreases to -15 μN. This is due to some portion of the film sticking onto the indentation tip and extra force was needed to pull out the indentation tip.

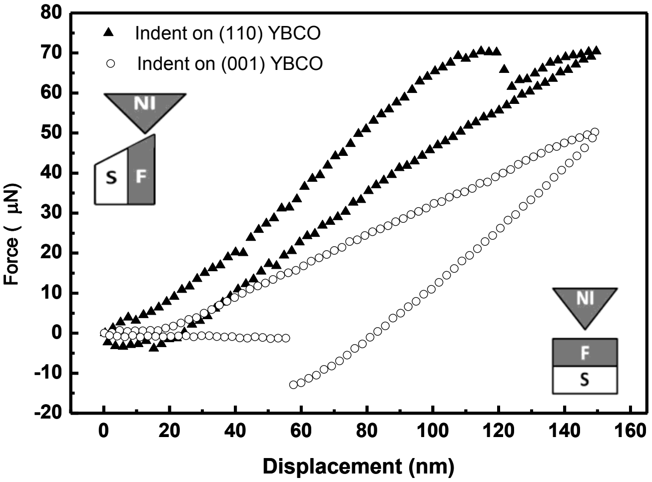

Figure 4.4. Two force-displacement plots are compared for indentation on YBCO (110) plane (solid symbols) and indentation on YBCO (001) plane (open symbols). Insets illustrate different indentation directions along film. (Based on instrument specifications, the estimated measurement error of force is ± 5%.)

Based on the force-displacement curves in *in situ* work, one can estimate the instantaneous pressure corresponding to the maximum load. In previous research reports, it has been discussed that the Hertz contact model does not consider film thickness, which could result in overestimated values [108]. Considering the film thickness and indentation geometries as illustrated in Figure 4.2, we can calculate the instantaneous pressure at the maximum force loaded by applying equations 4.1 and 4.2. The mean stress, σ, can be calculated with equation 4.1

$$\sigma = \frac{F}{A} \qquad (4.1),$$

where F is the load (force) and A is the projected contact area.

With consideration of the thickness of thin TEM foil and geometry of the nanoindentation tip (illustrated in Figure 4.2), the projected contact area, A, can be calculated with following equation:

$$A \approx 2t\left[\frac{R}{\cos(\frac{\alpha}{2})} + (D-R)\tan(\frac{\alpha}{2})\right] \qquad (4.2)$$

where t is sample foil thickness, D is indentation depth, R is the tip radius, and α is the tip angle. The estimated mean stress of indentation on (110) plane is ~ 7.4 GPa with a measured load F of 70.0 μN at the given maximum load, given R = 100 nm, D ≈ 150 nm, t = 30 nm, and a tip angle α of 70^{o} (Figure 4.4). Using the Hertzian theory of elastic contact [107], the maximum stress is 1.5 times the mean stress, which is ~ 11.1 GPa. Consistent with the *ex situ* nanoindentation results, the estimated hardness value for indentation on (001) plane shows a smaller value of ~ 8.0 GPa at the maximum load of 50 μN. Again it is about a 40% increase in the maximum stress value for the case of indenting on (110) planes compared with the case of (001) planes. These results are consistent with our *ex situ* nanoindentation results and again confirm that the twin structure strengthens YBCO films.

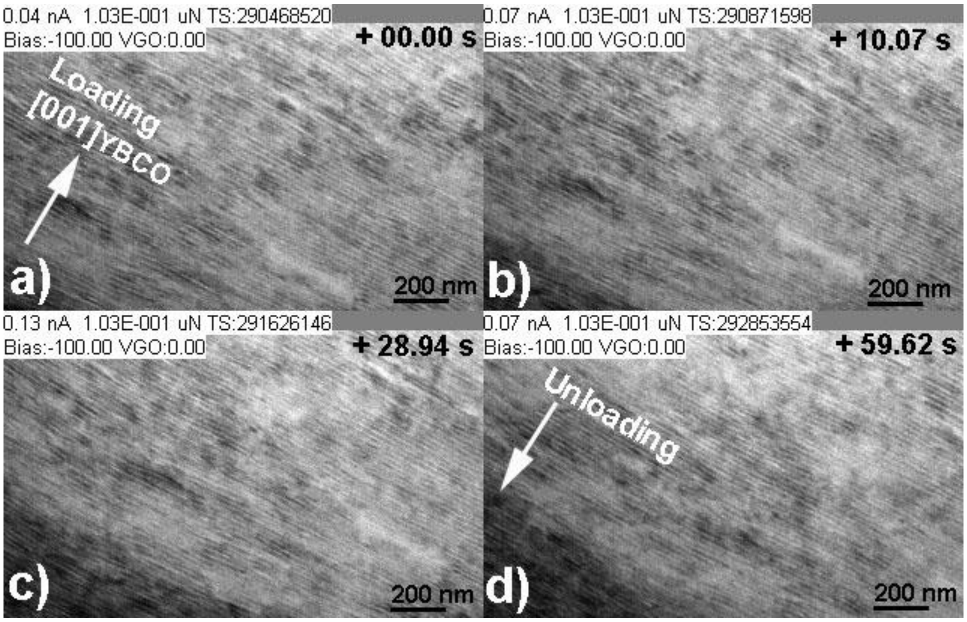

Figure 4.5. A series of movie frames during indentation on YBCO (001) plane is shown in a) before indentation, b) during loading, c) near maximum load, and d) after unloading.

During the *in situ* nanoindentation experiments, the deformation activities were captured by digital videos and snapshots along with the quantitative load-displacement measurements in real time. The loading process at a constant displacement rate continues up to 30 s, followed by an unloading process at the same rate. Figure 4.5 shows a series of snapshots (TEM images) corresponding to the force-displacement curves in Figure 4.4. Figure 4.5a-d are the snapshots taken during the indentation normal to YBCO (001) plane, where the clear lattice fringes of YBCO film can be seen. Each image was labeled with the time in seconds during experiment. Near the maximum load at 28.94 s, there’s a minimal contrast change due to the high strain introduced by indenter; also, the lattice fringes become less clear. Besides this, no other obvious change was observed during the loading process. After the indentation, at 59.62 s, the sample was completely retracted to its original position with a small contrast change. The small contrast variation might be because of lattice distortion caused by the local strain during the indentation. Unlike the indentation on YBCO (001) planes, during the indentation normal to (110) planes, obvious contrast change was observed. Figure 4.6a-d show a series of snap shots taken during the indentation on YBCO (110) planes. Before indentation, clear twin boundaries perpendicular to the loading direction are observed in Figure 4.6a. Twins with bright contrast are narrow, whereas the ones with dark contrast are wider. However, once the loading process starts (at the right-middle region of the image, marked by a box), the contrast of the narrow twin boundaries reversed (from bright to dark) at 7.84 s. Then at 30.00 s under the maximum applied load, the reversed contrast extended from right to the middle of the micrograph as shown in Figure 4.6c. In addition, the widths of the twins changed. Finally, after unloading, at 60.17 s in Figure 4.6d, the sample shows a small variation in both the contrast and twin thickness compared to its initial condition. For example, the twin marked with black arrow shows a slight increase in twin thickness as compared to its initial state. These observations suggest that twin boundaries indeed play an important role in accommodating the stress during the deformation of YBCO films.

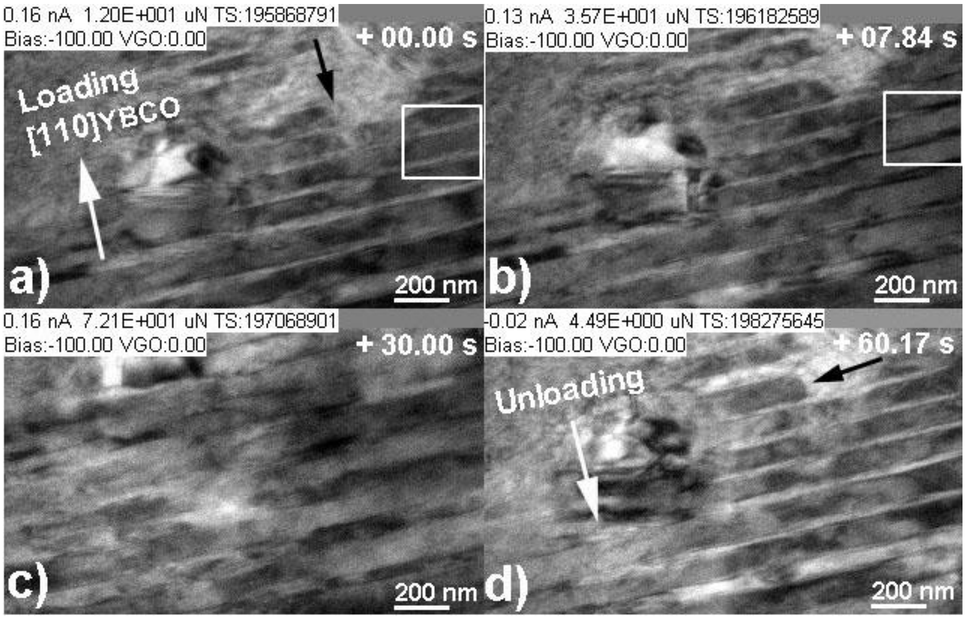

Figure 4.6. After indentation on YBCO (110) planes, the corresponding movie frames are shown a) before indentation, b) during loading, c) at maximum load, and d) after unloading.

To clarify the role of twins in deformation mechanisms of YBCO films, more detailed analyses have been performed, and a typical example is given in Figure 4.7. In this case, the loading-unloading experiment has been conducted for 80 s, from which video frames for the period from 34 to 48 s were selected to understand the activities of twins during deformation. Figures 4.7a and b were taken during the loading process, between 0 and 40 s, and Figure 4.7c–f were captured during unloading process, from 40 to 80 s. During loading up to 34.87 s, twin/matrix boundaries are clearly observed with sharp alternating contrast. To track the twin activities during deformation, two typical twins have been labeled as twin 1 (bright) and twin 2 (dark) for illustration. At 34.87 s, twins 1 and 2 have the thickness of 23.5 nm and 44.2 nm, respectively. As reference, two other twin boundaries were selected and marked with black arrows. Using the references, the relative location of each twin boundary can be traced during deformation. At 39.63 s, the contrast of the twins starts to get blurred and boundaries become less clear. The dark contrast presents in twin 1and spreads up at 41.65 s, showing an increased width of 35.36 nm while twin 2 has a decreased width of 35.67 nm. At 42.65 s, the contrast of twins gets blurred, and the dark contrast area in twin 1 is further extended. At 44.67 s, the dark contrast dominates all of twin 1, while the adjacent twin is covered by bright contrast. At 47.90 s, the contrasts of twin 1 and 2 along the boundaries are completely reversed from their original ones. Finally, twin 1 shows a width of 46.64 nm and twin 2 shows a decreased width of 32.6 nm. This indicates that reorientation of twin structures occurs while each twin accommodates the external stress by twin spacing variation during the deformation process.

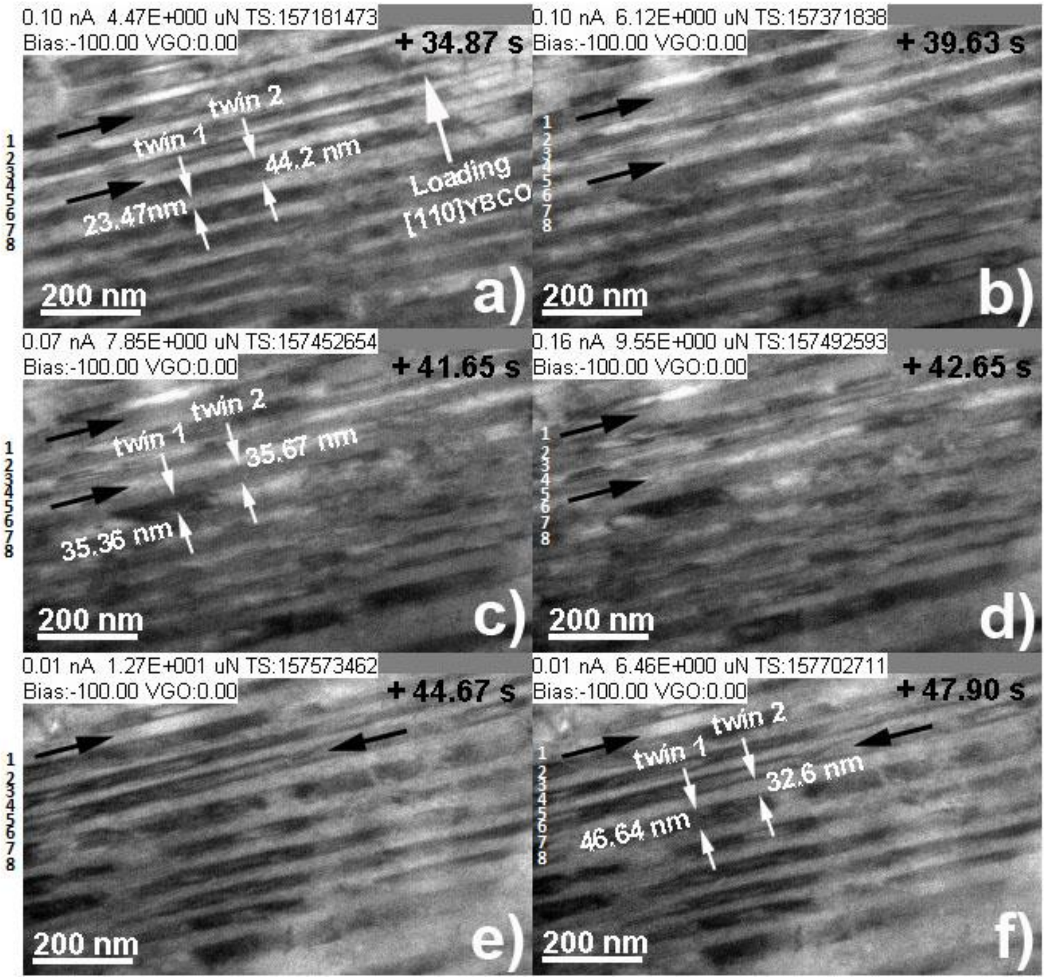

Figure 4.7. During indenting on YBCO (110) plane, obvious deformation of twin structures was observed. A series of movie frames shows the deformation region with a detailed analysis a)-b) during loading and c)-f) during unloading.

Finally an example is presented where the loading-unloading curve is coupled with movie snapshots to reveal the nucleation and propagation of twins. Along with the force-displacement and force-time plots (Figure 4.8h and g), several movie snapshots are shown of interesting deformation events, as shown in Figure 4.8a-f. The loading-unloading process was completed in 80 s, wherein the loading process ran from 0 to 40 s, corresponding to Figures 4.8a-d, and Figures 4.8e and f were taken during unloading process, from 40 to 80 s. Before indentation, as shown in Fig. 4.8a, twins and other planar defects are observed in YBCO films. During initial indentation, the loading force increased rapidly to ~ 20 μN at 17.34 s, at which point the microstructure, as shown in 8b, reveals a group of twins marked inside a circle that appears to encounter a spherical particle to the right and is pined well by the particle. During further loading process, up to 23.61 s, the twins in the circle becomes less distinct. Meanwhile, the corresponding force-displacement plot shows a plateau (or step) in Figure 4.8g (from point b to point c). Upon further loading, the slope of the plot starts to increase abruptly to a maximum load of ~ 67.7 μN. Near the maximum load, at 35.72 s, clear twin contrast is again revealed. Furthermore, twins appear to extend through the lower section of the spherical particle. In the region where the circle was drawn, the twin lamella are clearly offset with respect to one another. Similar to the experiment depicted in Figure 4.7, this set of twin activities again confirms that twins are effective barrier for external stress which always corresponding to the increased load in force-displacement curves. During unloading process, at 50.23 s, as shown in Fig. 4.8e, the offset of twins is insignificant and the twin microstructure is somewhat similar to that of Fig. 4.8b, where a similar load was applied. When unloading is nearly complete, at 79.89 s, the microstructure appears to have recovered by a large extent to their initial condition.

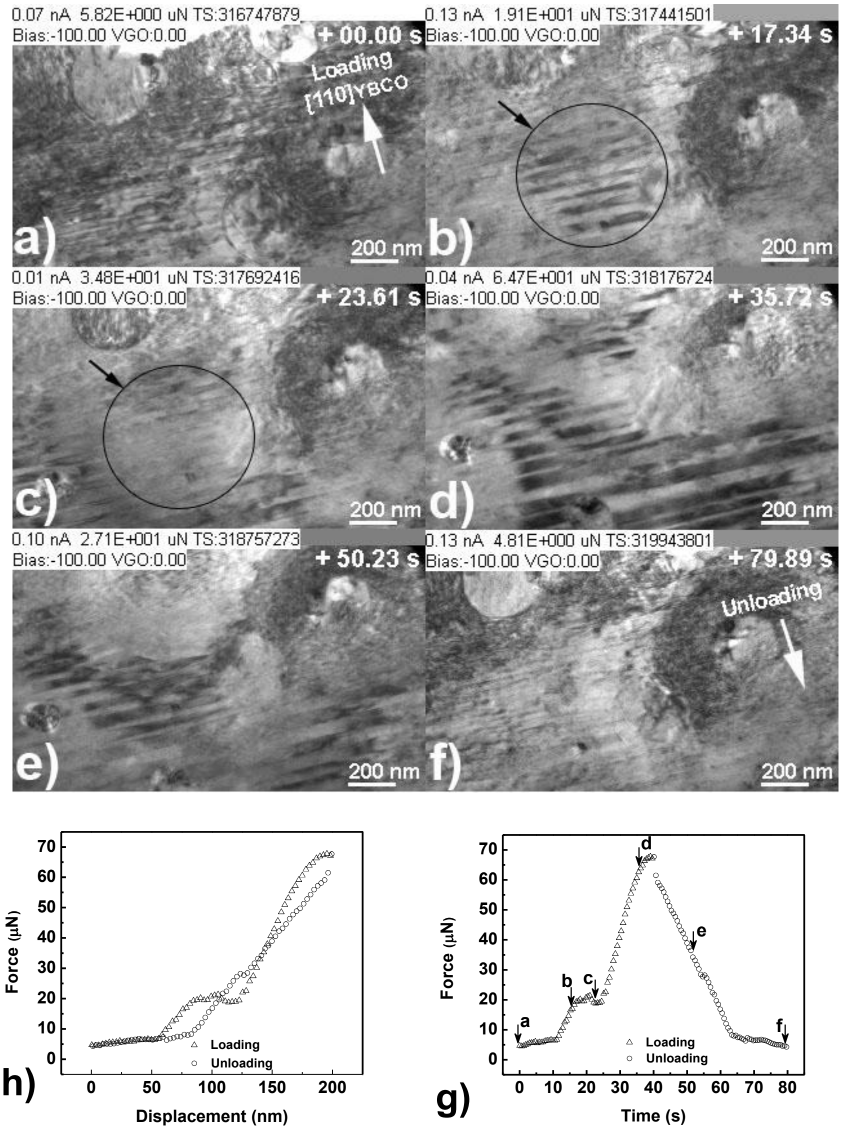

Figure 4.8. A detailed study on deformation mechanisms was carried out by correlating the force-displacement plot with the movie snapshots for indenting on YBCO (110) plane. The movie snapshots are a) before indentation, b) and c) during loading, d) right before maximum load, e) during unloading, and f) after unloading. The corresponding image letters are labelled on h) force-displacement and g) force-time plots. (Based on instrument specifications, the estimated measurement error of force is ± 5%.)

4.5. Conclusions

A series of YBCO thin films with various film thicknesses were prepared by PLD for conventional nanoindentation and *in situ* nanoindentation in TEM column. Through conventional nanoindentation, we observed that the indentation hardness on the (110) planes is about 50% larger than that on the (001) planes. Consistently through the *in situ* nanoindentation experiments, the mean stresses at maximum loads is 11.14 GPa for indentation on (110) planes and 7.95 GPa for indentation on (001) planes, which results in a 40% increase in the maximum load. Through detailed analysis using *in situ* movies, we found that during deformation, a certain portion of the twin structures reverses the contrast; more interestingly, variations in the width of the twin boundaries during the loading and unloading process were observed. This suggests that twin interfaces act as effective barrier for external stress and therefore enhance the mechanical strength of HTS YBCO films, in the direction perpendicular to the twin interfaces by accommodating the external stress through twins.

CHAPTER V

DIRECT OBSERVATION OF LOMER-COTTRELL LOCKS DURING STRAIN HARDENING IN NANOCRYSTALLINE NICKEL BY *IN SITU* TEM

5.1. Overview

Strain hardening capability is critical for metallic materials to achieve high ductility during plastic deformation. A majority of nanocrystalline metals, however, have inherently low work hardening capability with few exceptions. Interpretations on work hardening mechanisms in nanocrystalline metals are still controversial due to the lack of *in situ* experimental evidence. Here we report, by using an *in situ* transmission electron microscope nanoindentation tool, the direct observation of dynamic work hardening event in nanocrystalline nickel. During stain hardening stage, abundant Lomer-Cottrell (L-C) locks formed both within nanograins and against twin boundaries. Two major mechanisms were identified during interactions between L-C locks and twin boundaries. Quantitative nanoindentation experiments recorded during the experiments show an increase of yield strength from 1.64 to 2.29 GPa during multiple loading-unloading cycles. This study provides both the evidence to explain the roots of work hardening at small length scales and the insight for future design of ductile nanocrystalline metals.

5.2. Introduction

In polycrystalline metals with coarse grain size, strain hardening is typically described by Taylor relation, where the increases in flow stress is tied to increased dislocation densities [156, 157]. During plastic deformation, dislocation networks (or forest dislocations) may form in grain interior and thus become barriers to the propagation of successive mobile dislocations. Additionally strain hardening can also be described in terms of the decreasing mean free path of a dislocation and the reduced number of active slip systems for dislocations adjacent to barriers, such as grain boundaries or twin boundaries [158, 159]. Therefore control of slip distance by microstructural refinement can provide a feasible hardening mechanism.

Ultrafine grained and nanocrystalline (nc) materials have a large population of grain boundaries which are considered natural barriers to the propagation of dislocations. Indeed ultra-high mechanical strength has been achieved in nc and recently nanotwinned (nt) metals [160-166]. The size-dependent hardening has been explained by the Hall-Petch relationship, where the decrease of dislocation pile-ups in fine nc and nt metals leads to strengthening [160, 161, 3]. A recent study has suggested dislocation multi-junction formation in single crystal bcc molybdenum measurably increases the strength during a uniaxial compression testing [167].

Although nc metals can have much greater mechanical strength than their bulk counterparts, their ductility is typically low (less than a few percent of true strain) with a handful of exceptions. Strain hardening, which is crucial to achieve high ductility, is typically diminished in nc metals, or very often absent in many cases. There are various mechanisms that explain the lack of strain hardening in nc metals. Grain boundaries are effective sources and sinks for dislocations. Dislocations once emitted from grain boundaries may be absorbed rapidly by opposite grain boundaries in nc metals. Thus there may be lack of sustainable dislocation networks within the grains to provide the necessary strain hardening. *In situ* X-ray experiments evidenced rapid dislocation recovery events during unloading of plastically deformed nc Ni [168]. On the other hand, L-C locks associated with stair-rod dislocations have been observed near grain and twin boundaries after rolling of nc Ni, and were proposed to be effective barriers to mobile dislocations and result in work hardening [169]. There is no *in situ* evidence to explain the origin of such controversy. Additionally stacking fault energy (SFE) appears to play an important role on work hardening capability of nc metals. Stacking faults appear to inject work hardening capability in low SFE metals [170].

Despite extensive studies on work hardening in metallic materials, most of the previous works focused on post-deformation microstructural analysis. Meanwhile, to directly probe the structure-property relationships, various real time phenomena have recently been recorded with *in situ* TEM mechanical testing of different materials systems. Among these studies, several are noteworthy, including evidence of mechanical annealing and dislocation source starvation in nickel pillar [81], increment of strain rate with dislocation nucleation within single crystal Al[80], dislocation slip in TiN thin film[94], grain rotation and coarsening in polycrystalline Al thin film[79], dislocation climb in Al/Nb multilayers[82] and grain boundary sliding and grain rotation in ceramic nanocomposite[108]. However there is scare *in situ* TEM evidence on strain hardening in nc metals.

In this study, *in situ* nanoindentation in a transmission electron microscope was conducted on nc Ni. During multiple loading-unloading cycles, prominent work hardening was observed from quantitative nanoindentation experiment. In parallel, work hardening was found to arise from the formation of abundant L-C Locks both within the grains and at twin boundaries. L-C Locks interacted with twin boundaries through the formation of active partial dislocations. Numerous deformation mechanisms were identified. (See experimental details in methods section).

The nc Ni powders were mixed by roller milling and consolidated by Spark Plasma Sintering (SPS) process. Details on the sample processing can be found elsewhere [26, 54]. TEM specimens were prepared through a conventional procedure including mechanical thinning, polishing and ion milling polishing. This typical set of Ni samples has nanocrystalline grains with a bimodal grain size distribution. The nanograins accompanied by the bimodal grain size distribution in nc Ni allow enhanced ductility and high mechanical strength [171]. Growth twins with an average twin spacing of ~ 30 nm were observed in numerous grains.

5.3. Experimental

In situ nanoindentation was conducted using an *in situ* nanoindentation holder (manufactured by NanoFactory, Inc.). *In situ* TEM analyses were conducted within an analytical electron microscope (JEOL2010) with a point-to-point resolution of 0.23 nm.

Images and movies during indentation events were captured using a built-in high resolution CCD camera in the microscope. While the indentation under the TEM column, the sample is controlled in three dimensions by a piezoelectric actuator. To avoid the slip between tip and sample surface, wedge diamond tip (tip angle ~ 50.5°) for standard load-displacement measurements is used. During *in situ* indentation experiment, the nanoindentation tip was fixed while the sample was moved toward the tip by a piezoelectric stage in a precision movement as fine as 0.1 nm/step. To examine more precise motion of dislocations during work hardening, a maximum depth of 50 nm was used with step length of 0.1 nm/step and holding time of 10 ms. Each loading-unloading cycle spans across 100 seconds, e.g., the loading process occurred at a constant displacement rate continues up to 50 sec, followed by an unloading process at the same rate of 1 nm/sec (the estimated strain rate is 3.6×10^{-2} s^{-1} for the first cycle, 4.1×10^{-2} s^{-1} for the second cycle and 4.5×10^{-2} s^{-1} for the third cycle). While the force was measured along displacement and time, the estimated measurement error was ± 5%.

5.4. Results and discussion

Figure 5.1a shows the TEM image of two major grains, delineated as G1 and G2 in a typical area selected for *in situ* nanoindentation study. G1 contains three twin boundaries (TBs), labelled as TB1-TB3. Figures 5.1b-d show the selected area diffraction (SAD) patterns corresponding to matrix and twin (T1) in G1, and G2. Comparison of Figure 5.1b and 1d shows the formation of a 30^{o} high angle grain boundary between G1 and G2.

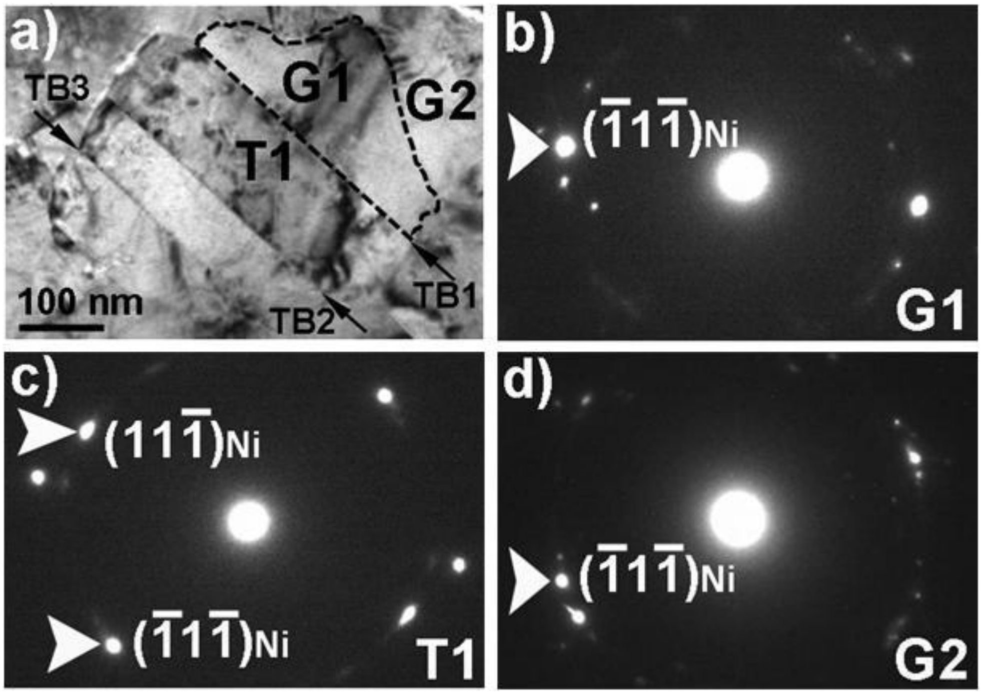

Figure 5.1. a) TEM image shows the area where *in situ* nanoindentation experiments were conducted. It shows very obvious grain and twin structures. From the top to bottom, grains, G2 and G1, and twin, T1, are marked. The arrows point the boundaries between G1, G2 and T1. The inserted SAD diffraction patterns were taken from the area of b) grain, G1, c) twin, T1, and d) grain, G2.

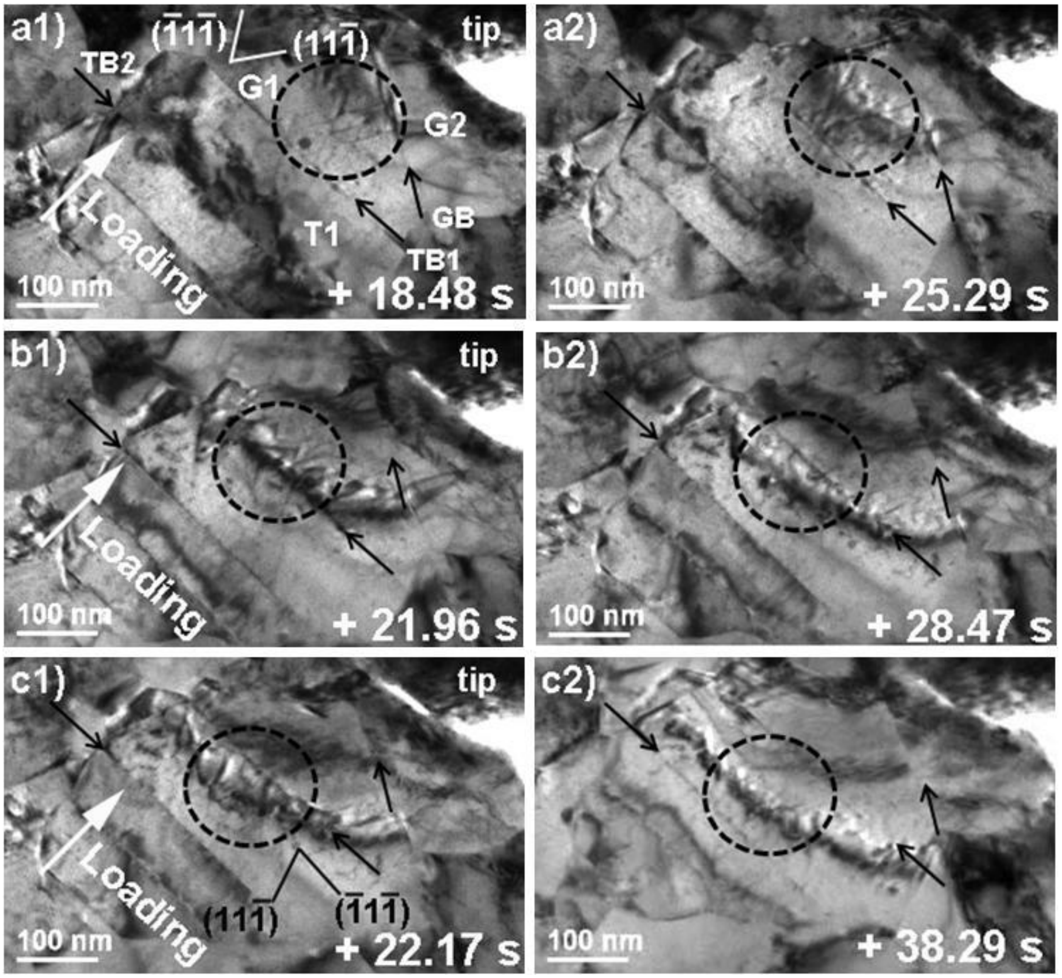

Figure 5.2. Three sets of movie frames during indentation on nc nickel are shown in a1) before and a2) after yield point during the first cycle; b1) before and b2) after yield point during the second cycle; and c1) before and c2) after yield point during the third cycle.

To examine dislocation activity during deformation, *in situ* nanoindentation has been performed. Three indentation (complete loading-unloading experiments) cycles were conducted in exactly the same area as shown in Figure 5.1a. Figure 5.2a1 -a2 are the video snap shots captured during the first loading cycle before (at 18.48 s) and after the yield point (at 25.29 s) as revealed from the force–displacement (F–D) plot in Figure 5.3a. Similarly, microstructure evolutions (before and after yielding) for the 2nd and 3rd loading cycles were recorded in Figure 5.2b1-b2 and 5.2c1-c2. The corresponding F-D plots are shown in Figure 5.3b and c. The yield point was determined from the corresponding F-D plots, on which a clear non-linear deformation can be identified. During these experiments, the nanoindenter tip was positioned at the upper right corner, and the samples were moving towards the tip with the loading direction marked as white arrows as shown in Figure 5.2.

During the first loading cycle before yielding (at 18.48s), groups of dislocations on the $(\bar{1}1\bar{1})$ and $(11\bar{1})$ slip planes in G1 are observed in the circled area in Figure 5.2a1. Many of these dislocations form V- shape junctions, which are typical signature of L-C locks. Under indentation these L-C locks are immobile before yielding (up to 22.96 sec). At the yield point, the L-C locks appear interacted with succeeding dislocations, and then became unlocked. The unlocked dislocations migrate towards the TB1 during continuous deformation after yielding (25.29 sec in Fig. 5.2a2). When numerous dislocations approach TB1, new L-C locks form at the twin boundary (Fig. 5.2b). And the density of dislocations at TB1 is ~ 7.0×10^{15} /m^2.

During the second loading cycle, dislocation density at TB1 rise continuously to ~ 1.2×10^{16}/m^2 by 21.96 sec as shown in Figure 5.2b1 (for details see supplemental information). By 28.47 sec a majority of dislocations including L-C Locks piled up against TB1 have transmitted through TB1. Correspondingly the F-D plot in Figure 5.3b shows a clear non-linear deformation, indicating the occurrence of considerable plastic deformation. Additionally the force at the onset of plastic yield approaches 6.6 μN, greater than that in the first cycle (~ 4.9 μN).

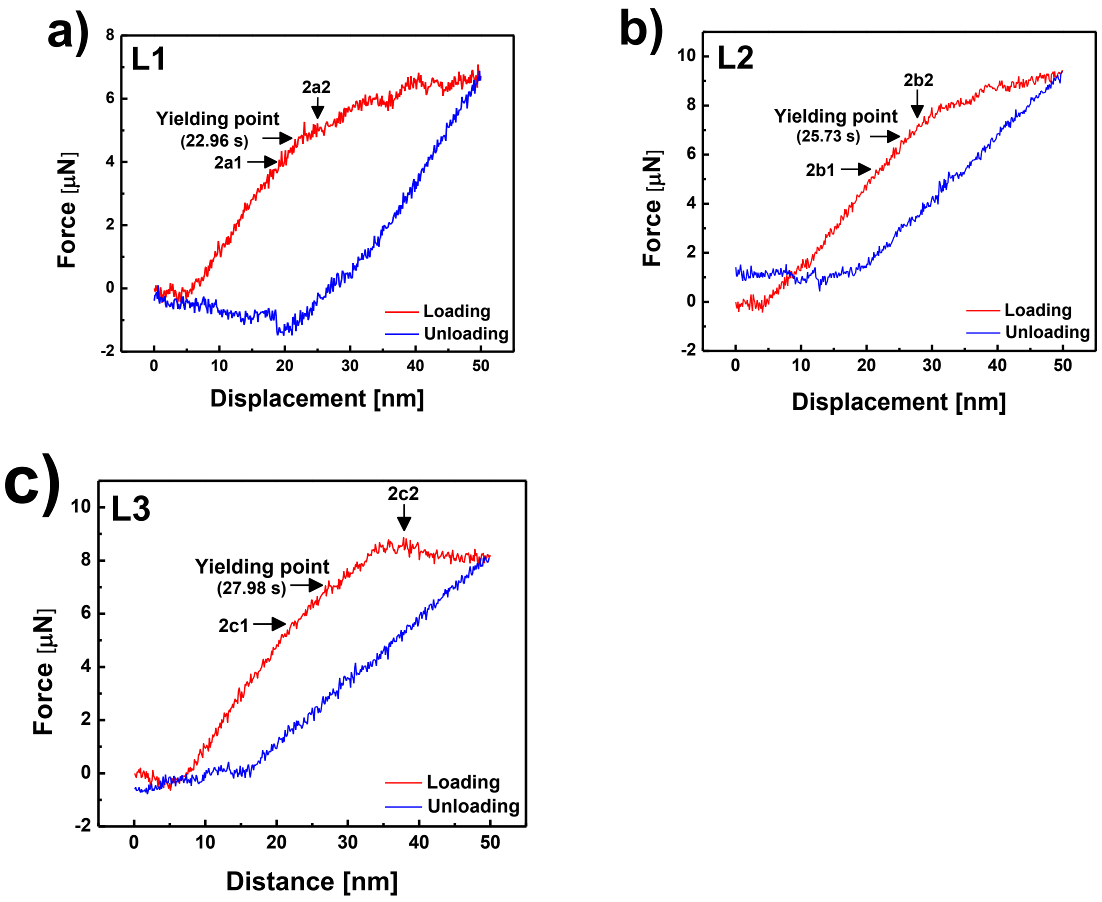

Figure 5.3. a) force-displacement plot was measured during the first *in situ* nanoindentation cycle. During the second cycle, b) force-displacement plot show the yield point increases compared to that in the first cycle. Finally, c) force-displacement plot was measured during the third cycle.

Finally, in the third cycle, at 22.17 sec, high density dislocations including L-C locks emerge underneath TB1 in T1 (the twinned crystal). The newly formed L-C locks become barriers to succeeding dislocations and applied load continues to increase. At the yield point, ~ 28 sec as shown in Figure 5.3c, L-C locks begin to unlock. By 38.29 sec near the maximum load in Figure 5.3c, L-C Locks are nearly completely annihilated, and the TEM image shows dark contrast surrounding a band of forest dislocations resulting from dislocation-L-C Lock interactions in T1 (Fig. 5.2c2). Obvious load drop is identified in Figure 5.3c during continuous deformation.

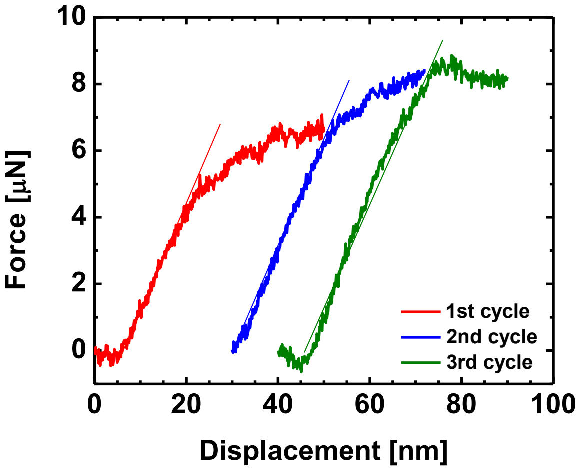

Figure 5.4. Three force-displacement plots only with the loading regime show the nature of work hardening after sequential indentation. Increment of the force at the yield point from ~ 4.9 to 7.0 μN during the three loading cycles is shown. A small regime of softening during the third cycle is observed due to the dislocations exhausted in G1.

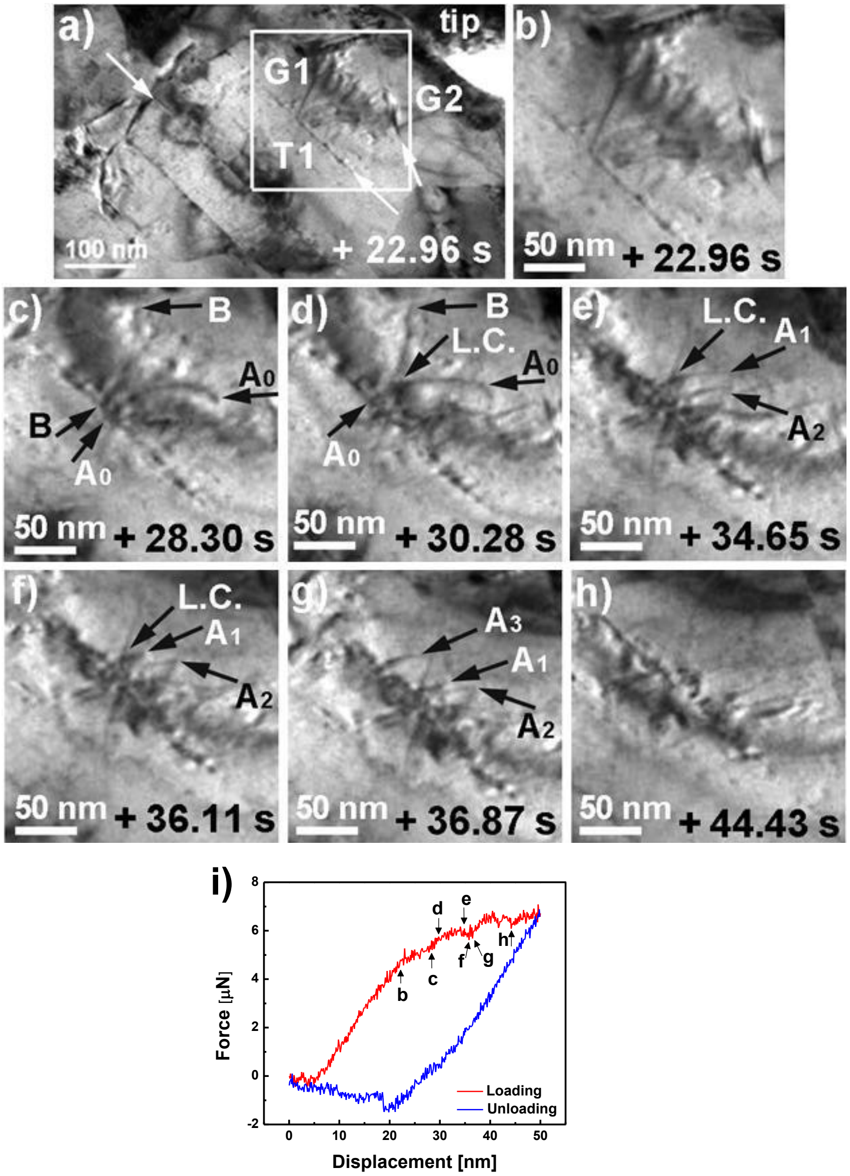

Figure 5.5. During the first indentation cycle, evident activity of dislocations (mainly screw or mixed dislocations) at the twin boundary was observed with formation of L-C lock. a) A snap shot taken shows the area of interest marked by a white box near TB1. And enlarged series of movie frames show the interaction between dislocations and twin boundary b) at yield point and c-h) after yield point, with the corresponding i) force-displacement plot.

Comparison of multiple consecutive F-D plots in Figure 5.4 shows that the force at the yield point increases sequentially from ~ 4.9 to 7.0 μN during the three loading cycles. Consequently given the measured foil thickness and loading depths, we arrive that the yield strength increases from ~ 1.6 to 2.3 GPa by using a relation described in supplemental information.

Work hardening is a complicated plastic deformation phenomenon. Cottrell stated that work hardening is the first phenomenon discovered in studying plasticity of metals, and may be the last problem to be solved [172]. Work hardening deemed necessary for the achievement of ductility is largely absent in a majority of nc metallic materials. But foregoing *in situ* nanoindentation studies strongly suggest that significant work hardening takes place in nc Ni.

Several salient characteristics can be derived from the *in situ* studies. First, work hardening may arise directly from the formation of L-C locks in grain interior. L-C locks form the back-bone of dislocation networks and resist the propagation of mobile dislocations. This mechanism has long been postulated and recently received some support from *ex situ* rolling studies of nc Ni [169]. The formation of L-C locks arises from the interaction of dislocations on two sets of inclined {111} planes. Second, L-C locks formed within grains were removed at higher stress by mobile dislocations (many of which maybe mobile partials). Recent MD simulations show that mobile Shockley partials can engage stair-rod dislocation in stacking fault tetrahedra (SFTs), and the interaction leads to new mobile partials which then glide on the surfaces of SFTs and lead to decomposition of SFTs [173]. Hence it is likely that abundant partials emitted from grain boundaries may lead to the removal of L-C locks in grain interior. Third, L-C locks when encountered twin boundaries can lead to even greater work hardening (as indicated by the necessity of higher stress for plastic yield shown in the second loading cycle). The details of interaction of L-C locks with twin boundaries are complex, and at least two scenarios are identified.

We begin by first examining the work hardening mechanism that arises from the interaction of L-C locks with twin boundaries. Figure 5.5 shows a set of snap shots captured from 22 to 45 sec (after yielding) during the first loading cycle. The area of interest marked by a white box in Figure 5.5a is near TB1, and the box is enlarged in Figure 5.5b. By 28.30 sec two dislocations (possibly mobile screw or mixed dislocations), A_0 and B from different set of {111} plane intercept at TB1. During continuous indentation at 30.28 sec, the two dislocations interact and an L-C. lock forms. At 34.65 sec, A_0 vanishes and two new dislocations, A_1 and A_2, emerge. By 36.87 sec, a new dislocation A_3 appears at TB1. By 44.43 sec, these dislocations appear absorbed by TB1.

The interaction mechanism of these dislocations with twin boundaries is shown in a schematic diagram in Figure 5.6. As shown in Figure 5.6a-b, two full dislocations, A_0 and B, from differently oriented {111} planes form an L-C lock at the twin boundary. Based on the equation of $a/2[101] + a/2[01\bar{1}] = a/2[110]$, the formation of Lomer dislocation (at the intercept of L-C locks) can reduce the overall elastic energy of the dislocations. The Lomer dislocation formed has a Burgers vector parallel to the electron beam, and hence appears as a dot during numerous interaction events.

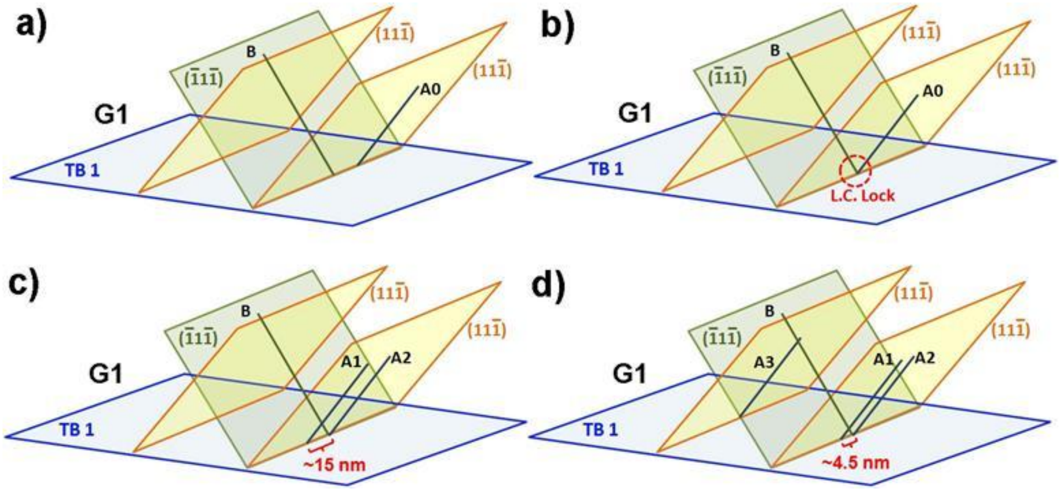

Figure 5.6. Schematic diagrams illustrate the interaction of L-C locks with twin boundaries from series of movie snap shot in Figure 5.5. a) Two full dislocations, (possibly screw or mixed dislocations), A_0 and B, on different set of {111} planes intercept at TB1. b) As dislocation A_0 glides toward dislocation B, an L-C lock is formed at the twin boundary. c) Dislocation A_0 dissociates into two partial dislocations, A_1 and A_2 as separated by ~15 nm. d) As the separation is constricted to ~4.5 nm, another dislocation A_3 is emitted from the dislocation A_1.

A_0 then dissociates into two partial dislocations marked with A_1 and A_2, separated by ~ 15 nm. The dissociation event occurs at a rate of ~19.3 nm·s^{-1} (dividing the separation distance by the time). The force decreases by ~4.8% during the dissociation event. Since the self-stress (line tension) of the dislocation is proportional to its curvature [174], the back stress from the forest dislocations in addition to the line tension in dislocation A_0 causes it to unbow which allows the perfect dislocation to then separate into leading and trailing partials. After dissociation, the partial dislocation A_2 is still associated with the dislocation B. The other partial dislocation A_1 appears to be the source for emission of another dislocation, A_3. The emission of A_3, very likely a screw dislocation, occurs at a rate of 116 nm·s^{-1}. If A_3 was to have non-screw dislocation nature, then its emission and migration shall be a type of climb, which typically occurs at a very low rate at room temperature. During the aforementioned events, continuous increase of stress is necessary in general to promote the interaction of L-C locks with twin boundaries, and consequently work hardening is achieved.

Next we consider a mechanism that may lead to the transmission of dislocations from L-C locks across twin boundaries. In the second indentation cycle, several snap shots captured during 21 to 33 sec are shown in Figure 5.7. This period corresponds to the deformation right before the maximum load is achieved. Figure 5.7a shows a box that outlines the area of interest, which is then magnified in Figure 5.7b (at 21.65 sec). An L-C lock due to interception of A_0 and B (likely to be screw or mixed dislocations) is identified. During continuous deformation from 25.71 to 28.23 sec, the contrast of B decays rapidly; meanwhile, a dislocation labelled as B' emerges from underneath the twin boundary and resides on a (100) plane in the twinned crystal T1. By increase of the applied stress to 2.4 GPa (near 28.56 sec), dislocation A_0 vanish, instead A_1 and A_2 appear as shown in Figure 5.7g. Then dislocation B rapidly passes through the twin boundary and becomes dislocation B' (Fig. 5.7h). By 32.98 sec, dislocation A_1 and A_2 also transmit through twin boundary.

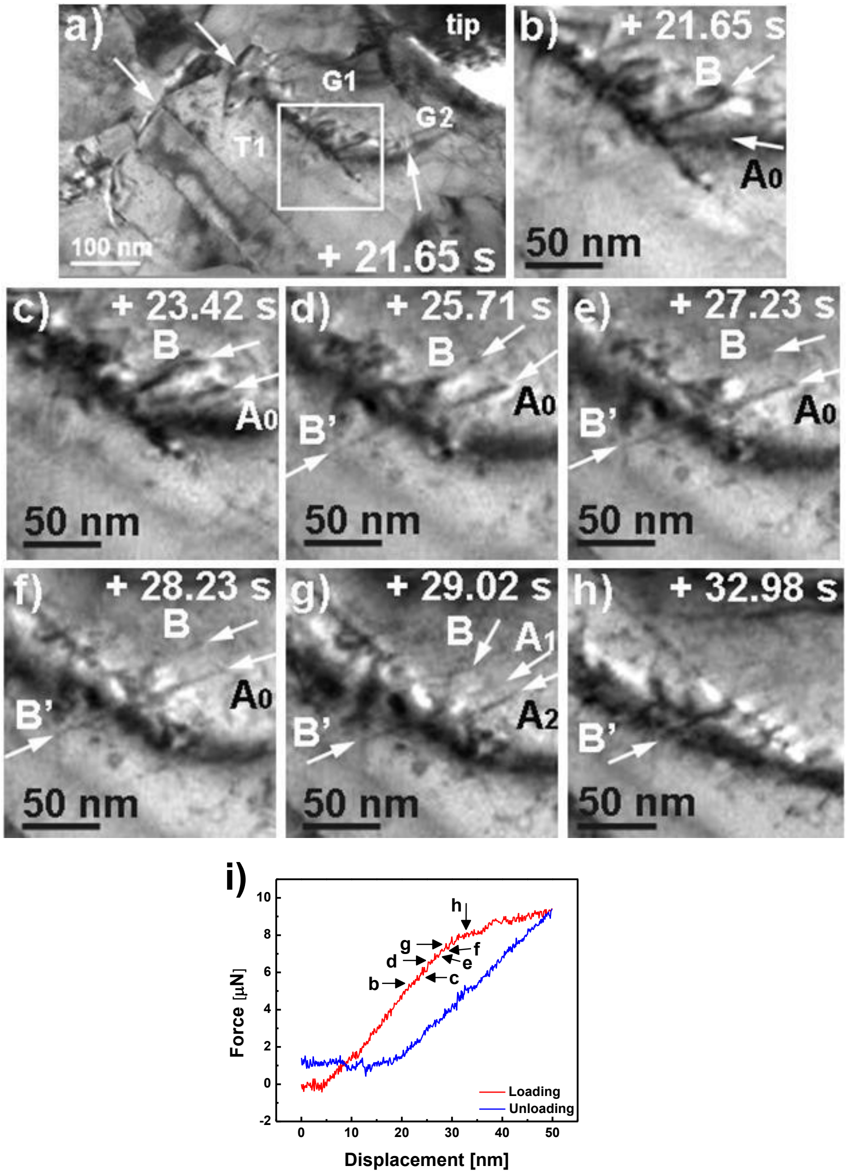

Figure 5.7. a) A snap shot taken during the second indentation cycle shows the area of interest marked by a white box near TB1. And enlarged series of movie frames show interaction between two specific dislocations, A_0 and B (likely to be screw or mixed dislocations), resulting in the transmission from L-C locks across twin boundaries, with a detailed analysis as shown in b), c) and d) before yield point and e), f), g) and h) after yield point, with the corresponding i) force-displacement plot.

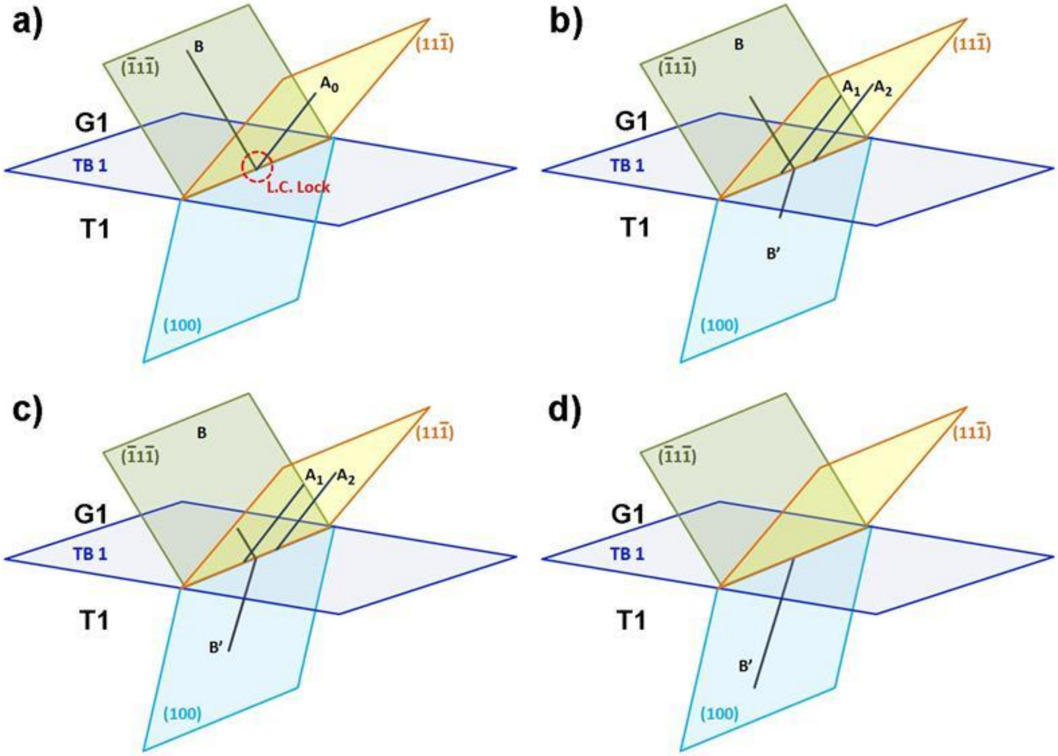

Figure 5.8. Schematic diagrams illustrate process of dislocation transmission across TB1 from series of movie snap shot in Figure 5.7. a) Two full dislocations, A_0 and B, on different set of {111} planes form an L-C lock at the twin boundary. b) Dislocation A_0 dissociates into two partial dislocations, A_1 and A_2. Meanwhile, c) dislocation B penetrates through the twin boundary and glides on the (100) plane in T1 as the dislocation B' as released from the back stress at the L-C lock. d) Dislocation B completely penetrates through the twin boundary. Then, dislocation A_1 and A_2 also pass through the twin boundary.

Figure 5.8 shows the schematics that illustrate the series of interaction event. Basically the L-C lock forms at twin boundary due to interactions of A_0-B dislocations.

B gradually transmits through twin boundary and becomes B' on lower (100) plane, whereas A_0 remains intact. The transmission of full dislocation in Ni has been modelled by MD simulation. The simulation shows that under high resolved shear stress, ~ 3 GPa, a full dislocation will transmit across twin boundary onto the lower {100} plane in the twinned crystal l[175]. At increasing stress, A_0 dissociates into A_1 and A_2 as shown in Figure 5.8b at a velocity of ~12.3 $nm \cdot s^{-1}$. The dissociation is likely to relieve some of the back stress at the L-C lock, and consequently making it easier for B to rapidly transmit across twin boundary as shown in Figure 5.8c.

Twin boundaries have been proved as effective barriers to the transmission of dislocations. It has been previously reported there might be stair-rod dislocation generated along twin boundaries, after the partial dislocation interacts with the boundaries[55] which possibly blocks the dislocation penetration through the boundary in this work. Additionally, residual dislocations density stored at the twin boundary increases during indentation (from 6.96×10^{15} /m^2 to 1.22×10^{16}/m^2). Significant increase in dislocation density has been observed in rolled nt Cu, wherein dislocation density approaches 10^{16}/m^2 at a true strain level of 50% or greater [176]. Consequently high density dislocations may increase the barrier strength of twin boundary to the transmission of dislocations and lead to enhanced work hardening.

5.5. Conclusions

In summary *In situ* nanoindentation experiment shows solid evidence for significant work hardening in nc Ni based on sequential loading-unloading cycles.

During work hardening, the dislocation density along the TB increases, and the yield strength increases gradually by ~40 %. Frequent formation of L-C locks were identified in grain interior and along twin boundaries. L-C locks are effective barriers to dislocations and lead to work hardening. Several mechanisms of interaction between L-C locks and twin boundaries were identified which provide important insight to understand plasticity in nc metals.

CHAPTER VI

GROWTH-CONTROLLED SURFACE ROUGHNESS IN AL-DOPED ZNO AS TRANSPARENT CONDUCTING OXIDE*

6.1. Overview

The surface morphology of Al_2O_3-doped ZnO (AZO, 2wt %) thin films varies from a uniform layer to nanorod structure by simply controlling oxygen pressure during growth. All AZO films were deposited on sapphire (0001) substrates using a pulsed laser deposition (PLD) technique. In the low oxygen pressure regime (vacuum ~ 50 mTorr), AZO films grow as a smooth and uniform layer. In the high oxygen pressure regime (100 ~ 250 mTorr) AZO thin films with nanorods have formed. Detailed cross-section transmission electron microscopy (TEM) and x-ray diffraction (XRD) studies reveal that, besides the obvious variation in the film morphology, the in-plane *d*-spacing of AZO film increases and the out-of-plane *d*-spacing decreases, as oxygen pressure increases. A bilayer AZO film with a nanorod structure on top of a uniform layer was demonstrated by controlling the oxygen pressure for the two layers. Electrical resistivity and optical transmittance measurements were carried out to correlate with the microstructures obtained under different oxygen pressures. The bilayer AZO films could find applications as transparent conducting oxide (TCO) with unique light trapping function in thin film solar cells.

---

*Reprinted from "Growth-controlled surface roughness in Al-doped ZnO as transparent conducting oxide" by J. H. Lee, C.Y. Chou, Z. Bi, C.-F. Tsai, H. Wang, Nanotechnology 20 (2009) 395704. Copyright (2009), with permission from Institute of Physics.

6.2. Introduction

Transparent conducting oxide (TCO) thin films have a large variety of applications, such as transparent interconnects for optoelectronic devices including liquid crystal displays (LCDs), organic light emitting diodes (OLEDs) and solar cells [66-68]. Among all of the TCO materials researched recently, doped ZnO has brought extensive research interests because of its unique physical properties. ZnO is a direct band gap semiconductor with a bandgap of 3.4 eV. It can be used for optoelectronic devices operated in blue to UV regime. Compared with other TCO materials such as indium-tin-oxide is cheaper and non-toxic [69, 70]. To increase its electrical conductivity, ZnO is usually doped with B, Al, Ga or In (group III elements) as n-type [73, 177, 178, 179] or Na, K, P or N (group I or group V elements) as p-type semiconductors [180-183]. Among those, Al-doped ZnO (AZO) is one of the most widely studied n-type ZnO films. AZO films with high transmittance and electrical conductivity have been grown by various deposition techniques such as molecular beam epitaxy [184], Plasma enhanced chemical vapor deposition [185], sol-gel [186], sputtering [187] and pulsed laser deposition (PLD) [188].

Recently AZO film with designed surface roughness has been introduced as light trapping method for solar cell applications [189, 190]. The surface roughness was achieved by anisotropic etching method which involves lithographic patterning and etching steps. This leads us to explore a direct avenue for achieving high surface roughness during growth. It has been reported that deposition techniques and deposition parameters have strong impact on the electrical resistivity and optical property of AZO films. For example, the electrical resistivity of PLD-grown 200 nm thick AZO films has been reported to be in the range of $2.2\times10^{-4} \sim 1\times10^{-3}$ Ω·cm while a MOCVD-grown AZO film with same thickness possesses a resistivity value in the range of $4.5\times10^{-3} \sim 1\times10^{-2}$ Ω·cm [191, 192]. One of the main deposition parameters is oxygen pressure. Oxygen pressure has been reported to have strong effect on the surface roughness and optical properties of pure ZnO films [193, 75]. Therefore, it is highly possible that the oxygen pressure plays a very important role in the growth and nucleation of the AZO films and therefore results in a large variation in the physical properties of AZO films deposited by different techniques.

In this work, a systematic study has been conducted by depositing AZO films under various oxygen pressures to explore the effects of oxygen pressure on film morphology and properties. Bilayer AZO thin films were also grown with each layer deposited under different oxygen pressures. Detailed microstructural characterizations and electrical and optical measurements were conducted to resolve the effects of oxygen pressure on the microstructure and physical properties of AZO films.

6.3. Experimental

Depositions of 2 wt% Al_2O_3-doped ZnO films on sapphire (0001) single-crystal substrate were performed in a UHV chamber with a KrF excimer laser (Lambda Physik 210, = 248 nm, 10 Hz). The laser beam was focused to obtain an energy density of approximately 4 J/ cm^2 at 45° angle of incidence. The targets were hot pressed using a mixture of Al_2O_3 and ZnO powders and sintered at 1100 ^oC for 11 h in presence of oxygen. Single layer depositions were conducted under different oxygen partial pressures, i.e., 250 mTorr, 100 mTorr, 50 mTorr and vacuum. The bilayer deposition was conducted under two different oxygen pressures; i.e., first vacuum and then 250 mTorr. The substrate temperature was fixed at 750 °C for all depositions. The back pressure of the system was 1×10^{-7} Torr before oxygen was introduced. Microstructural characterizations, including X-ray diffraction (XRD) by Bruker D8 Discover X-ray diffractometer, surface morphology by atomic force microscopy (AFM), high resolution field emission scanning electron microscope (FE-SEM) and cross-sectional transmission electron microscopy (TEM) using a JEOL2010 analytical electron microscope with a point-to-point resolution of 0.23 nm, were performed on all the single layer and bilayer thin films. The optical properties of the single and bilayer films were measured by a U-4100 UV-VIS-NIR Spectrophotometer. Electrical resistivity was measured by a four-point probe measurement system.

6.4. Results and discussion

6.4.1. Microstructure and surface morphology

XRD $\Theta \sim 2\Theta$ scans of all four single layer Al-doped ZnO films under different oxygen pressures were plotted in Figure 6.1a. For all single layer samples, ZnO (0002) and (0004) peaks are aligned well with sapphire (0006) which suggests highly textured ZnO films grown along sapphire (000*l*). It is noted that the peak position of ZnO (0002) shifts from 34.5° to 34.12° as the oxygen pressure reduced from 250 mTorr to vacuum, i.e., the *d* spacing of the ZnO (0002) increases from 2.597Å to 2.625Å as the oxygen pressure decreases. Compared with the bulk value, $d_{ZnO(0002)}$ = 2.605Å, the film deposited under 250 mTorr has lattice parameters close to that of bulk ZnO. As the oxygen pressure reduces, the film starts to be in tension out-of-plane and in compression in-plane.

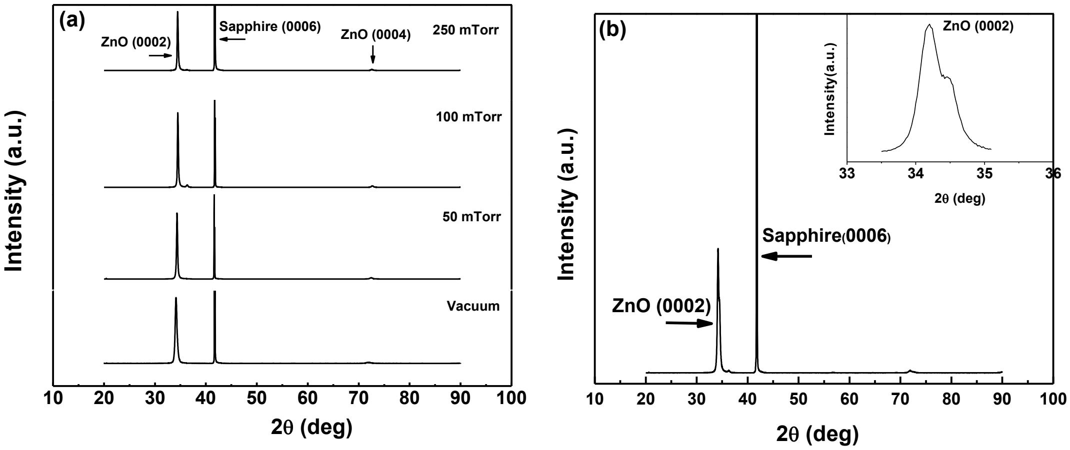

Figure 6.1. (a) XRD θ ~ 2θ scans of AZO single layer films grown under different oxygen pressures: 250 mTorr, 100 mTorr, 50 mTorr and vacuum, and (b) XRD pattern of a bilayer grown at vacuum and 250 mTorr sequentially. Inset in b is the enlarged ZnO (0002) peak showing an obvious peak splitting for the bi-layers in the sample.

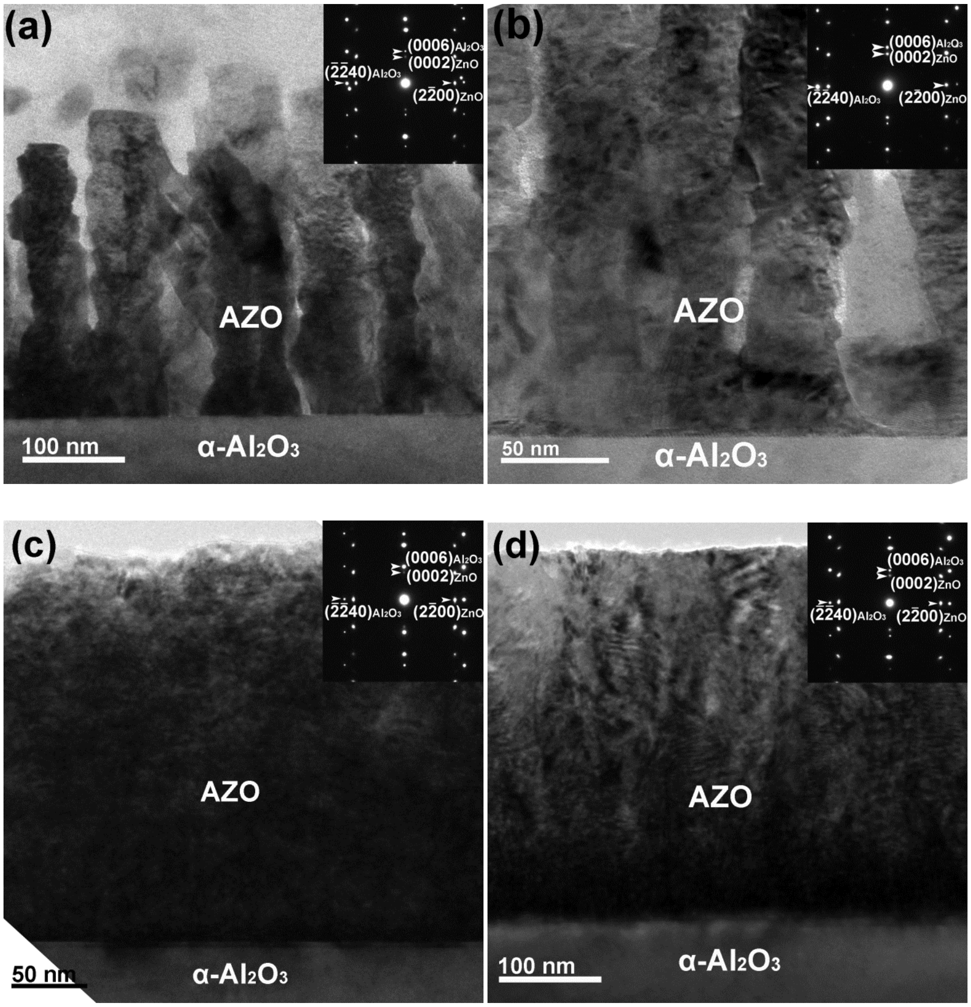

Figure 6.2. Cross-sectional TEM micrographs show a nanorod structure of AZO single layer epitaxially grown on sapphire substrate at oxygen pressures of (a) 250 mTorr (b) 100 mTorr while continuous layers grow at oxygen pressures of (c) 50 mTorr and (d) Vacuum.

Figure 6.1b shows the XRD Θ~2Θ scan of the bilayer of AZO film with first layer deposited at vacuum and second layer deposited at 250 mTorr. The overall XRD pattern is very similar to that of the single-layer samples, except that the ZnO (0002) peak splits into two peaks as shown as inset in figure 6.1b. This suggests that the bilayer sample consists of two layers with two different out-of-plane lattice parameters. The first peak at 2Θ = 34.2° (d = 2.626Å) is close to that of the single layer deposited under vacuum. The second peak at 2Θ = 34.4° (d = 2.605Å) has a similar 2Θ value as that of the single layer deposited under 250 mTorr.

In order to fully understand the microstructure variation as a function of oxygen pressure, we conducted a detailed cross-sectional TEM study for all the samples. Figure 6.2a-d show the cross-section TEM images of single-layer AZO films on α-Al_2O_3 (0001) substrates. It is very obvious that, the films, deposited under oxygen pressure of 250 mTorr (figure 6.2a) and 100 mTorr (figure 6.2b), are both grown as nanorods on sapphire substrate. The nanorods have an average diameter of 50 nm and an average spacing of 5-10 nm. On the other hand, under a low oxygen pressure regime at vacuum (2d) and 50 mTorr (2c), AZO films grow as a continuous layer with a smooth surface. More interestingly the nanorod average diameter decreases from 66 nm for the film deposited at 250 mTorr (2a) to 44 nm for the film deposited at 100 mTorr (2b), i.e., the width of the nanorods decreases as the oxygen pressure decreases. The insets are corresponding SAD pattern for all the samples. It is noted that the epitaxial quality of all the films is high, shown by the distinguished diffraction dots from the films, despite the fact that they have very different film morphology.

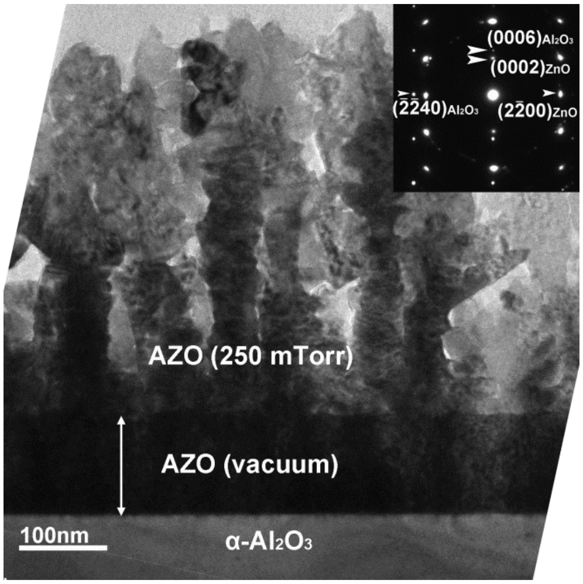

Figure 6.3. A cross-sectional TEM micrograph shows AZO bilayer epitaxially grown on sapphire substrate with sequential deposition at oxygen pressures of vacuum and 250 mTorr. The first AZO layer is grown with uniform layer structure under vacuum. The second layer is structured with nanorods under oxygen pressure of 250 mTorr.

It is possible that surface energy of the substrate might be different at different oxygen pressures, which results in the different surface morphologies under different oxygen pressures. To understand the growth mechanism under different oxygen pressures, we grew a bilayer film with a sequential deposition of a layer under vacuum and a layer under 250 mTorr of O_2 pressure. A cross-section TEM image of one such bilayer sample is shown in figure 6.3. A clear interface is observed between the two layers. The first layer deposited under vacuum grows as a continuous layer and the second layer grows as a nanorod structure as if it directly grew on top of the sapphire substrate. It suggests that the oxygen pressure plays more important role in the growth morphology rather than the surface energy of the underlying substrates.

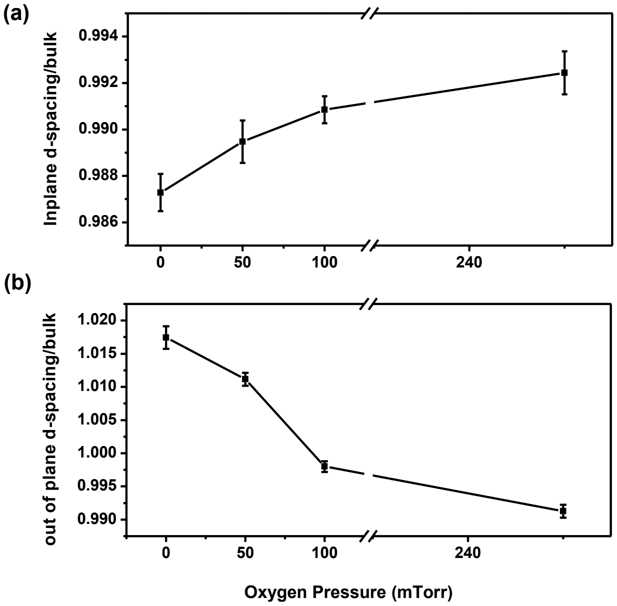

Figure 6.4. A plot of out-of-plane d-spacing change as a function of oxygen pressure. As oxygen pressure increases, (a) in-plane d-spacing increases while (b) out-of-plane d-spacing decreases.

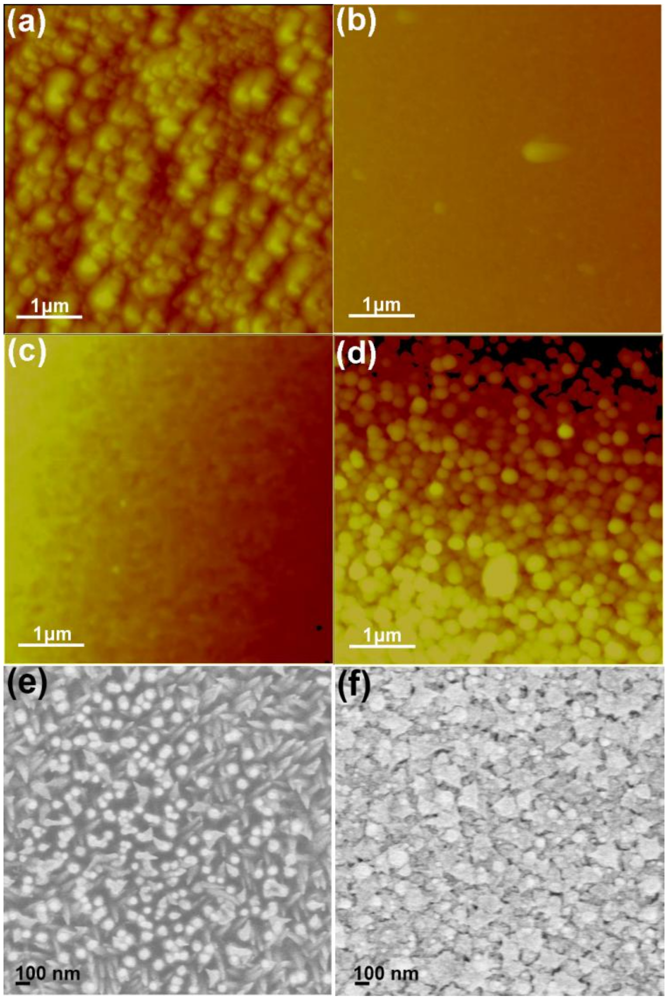

Figure 6.5. AFM images of AZO films grown at oxygen pressures of (a) 250 mTorr, (b) 50 mTorr, (c) vacuum and (d) bilayer of 250 mTorr and vacuum. SEM images of AZO films grown at oxygen pressures of e) 250 mTorr and f) bilayer of 250 mTorr and vacuum. Both the single layers grown at 250 mTorr and the bilayer have high surface roughness with nanorods. Films grown at low pressure regime (50 mTorr and vacuum) have a smooth film surface.

Besides the morphology variation we also observe a systematic change in the out-of-plane and in-plane *d*-spacing of AZO as a function of oxygen pressure (figure 6.1), which is confirmed by a detailed analysis on the corresponding SAD patterns. Based on the TEM SAD patterns and XRD patterns (figure 6.2) we calculated the out-of-plane *d* spacing of AZO (0002) and in-plane *d* spacing of AZO $(10\bar{1}0)$ and compared it with its bulk values as plotted in figure 6.4. Figure 6.4a shows the in-plane *d* spacing of AZO $(10\bar{1}0)$ increases with increasing oxygen pressure. On the other hand, in figure 6.4b the out-of-plane *d* spacing of ZnO (0002) decreases with increasing oxygen pressure.

The TEM microstructure result is consistent with the XRD data. In the range of 100 ~ 250 mTorr oxygen, the films grow as nanorods as the film lattices are relaxed without significant substrate lattice effect. While the films deposited at vacuum and 50 mTorr are continuous film, the films with $d_{ZnO\ (10\bar{1}0)\ \mathrm{bulk}} = 2.8179Å$ and $d_{ZnO\ (0002)\ \mathrm{bulk}} = 2.6049Å$ are highly strained by the substrate lattices with $d_{Al2O3\ (\bar{1}\bar{1}20)} = 2.3777Å$ due to the 18.5% lattice mismatch, i.e. in compression in-plane with $d_{ZnO\ (10\bar{1}0)\ \mathrm{under\ 50\ mTorr}} = 2.788Å$ and $d_{ZnO\ (10\bar{1}0)\ \mathrm{under\ vacuum}} = 2.782Å$ and in tension out-of-plane with $d_{ZnO\ (0002)\ \mathrm{under\ 50\ mTorr}} = 2.634Å$ and $d_{ZnO\ (0002)\ \mathrm{under\ vacuum}} = 2.650Å$. This is consistent with the XRD data, i.e. out-of-plane lattice parameter decreases as oxygen pressure decreases.

Surface morphologies of AZO films under different oxygen pressures were characterized by AFM and SEM and shown in figure 6.5. Increasing the oxygen pressure leads to an increase of surface roughness, which is consistent with the cross-sectional TEM observations. The film deposited at 250 mTorr (figure 6.5a and 6.5e) shows the highest surface roughness with its root mean square (rms) value of 33.425 nm. The surface roughness decreases to 6.3 nm for the film deposited at 50 mTorr (figure 5b) and 1.325 nm for film deposited at vacuum (figure 5c). Additionally, obvious island structures are observed on the film deposited at 250 mTorr O_2 pressure which corresponds to the top view of nanorods (figure 5a and 5e). In figure 6.5e, few tilted nanorod structures are also observed on the surface. The sample deposited at low oxygen pressure samples (50 mTorr and vacuum) show a rather smooth surface without such structures (figure 5b and 5c). The surface morphology of the bilayer AZO film (figure 5d and 5f) also shows a very rough surface with the RMS value of 30.742 nm, similar to that of the single-layer sample deposited at 250 mTorr (figure 5a). In order to view the nanorod structure, figure 6.6 plots the surface morphologies in line profile and the corresponding 3D images for the film deposited at 250 mTorr and the bilayer sample. Interestingly the film deposited at 250 mTorr (figure 6.6a and b) has randomly distributed nanorods while the bilayer film grown at 250 mTorr and vacuum (figure 6.6c and d) shows much more ordered arrangement of the nanorods. It suggests that the nucleation of the AZO nanorods on AZO films is more ordered than the one on sapphire substrate directly.

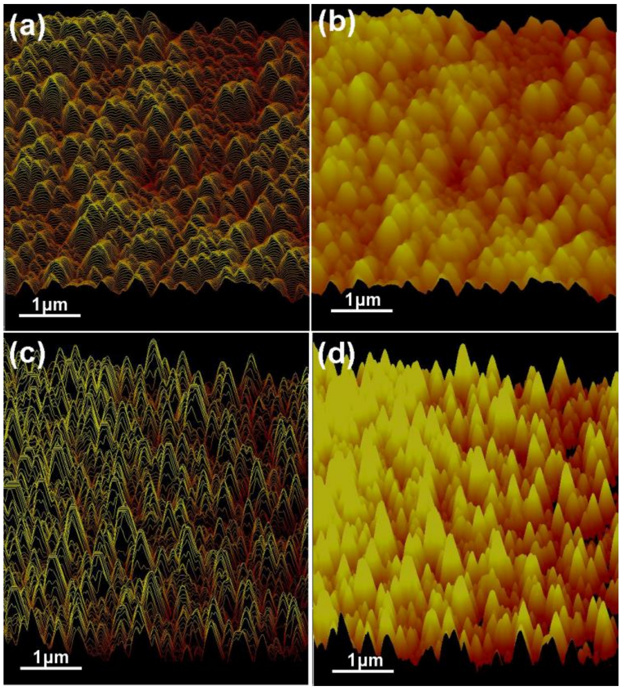

Figure 6.6. Line scans ((a) and (c)) and 3D surface plots ((b) and (d)) for single layer deposited under 250 mTorr ((a) and (b)) and bilayer AZO film ((c) and (d)). The bilayer film shows a more ordered nanorod distribution than the single layer deposited under 250 mTorr.

Similar oxygen pressure effects on growth morphology have been reported in other thin film materials. It was reported that ambient gas pressure during PLD affects nanocluster growth rate of CeO_2 film, which can determine the density of the microstructure [194]. However it is not yet clear why high oxygen pressure induces the columnar grain structure with intergranular gap while a film grown under vacuum grows as a fully dense columnar structure. A detailed study on AZO growth mechanisms is on-going in the authors' lab.

6.4.2. Optical and electrical properties

Optical transmittance measurements were conducted on all the AZO single-layer films to compare the oxygen pressure effect on optical properties of AZO films. Figure 6.7 shows the plot of optical transmittance spectra (%) versus wavelength for all single-layer films. For the single layers grown under low oxygen pressure regime (50 mTorr and vacuum) the spectra shows a very sharp absorption edge at 384 nm (E_g = 3.23eV) and a smooth wave form right after the absorption edge which suggests that the film has a high epitaxial quality with very smooth surface. On the other hand, the spectra of single layers deposited under a high oxygen pressure regime (250 and 100 mTorr) shows a relatively wider absorption edge and no wave form was observed. This suggests that these films have a rough surface, which is consistent with the nanorod structures observed in TEM. This result clearly suggests that AZO films in nanorods form have higher light reflection than the ones with smooth and continuous layer.

Room temperature electrical resistivity was measured by a four-point probe system and summarized in table 6.1. The electrical resistivity was varied from 25 mΩ-cm for the continuous layer deposited at vacuum, to 106 mΩ-cm for the single-layer with discontinuous nanorods structure deposited at high oxygen pressure regime (250 mTorr). Electrical resistivity data is again consistent with the microstructure study as the films with nanorods deposited at higher oxygen pressures have less conductivity in-plane than the continuous films deposited under lower oxygen pressures. The bilayer deposited at vacuum and then 250 mTorr has a resistivity value of 149 mΩ-cm, higher than the single-layer deposited at 250mTorr. Here the film porosity was not taken into count for the resistivity calculation. Recently it was reported that increasing oxygen pressures affects oxygen vacancies, zinc interstitials and grain sizes which reduce the carrier concentration and increase the resistivity [75]. However for our case, the surface morphology controlled by oxygen pressure affect the electrical conductivity strongly. The nanorod structure deposited at a high oxygen pressure regime will have very limited electrical transport in-plane and therefore result in high electrical resistance. The smooth layers deposited at low oxygen pressure have much better electrical transport in-plane and therefore higher electrical conductivity. It is interesting to note that a one-order of magnitude difference in electrical conductivity can be achieved by simply control the oxygen deposition condition.

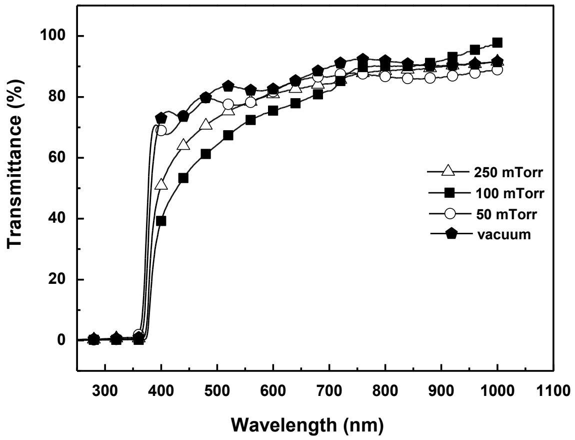

Figure 6.7. Optical transmittance spectra for single layers grown under different oxygen pressures at 250 mTorr, 100 mTorr, 50 mTorr and vacuum. The spectra for film grown at 50 mTorr and vacuum show a sharp absorption edge; instead, wider absorption edges are found with spectra for film grown at 250 and 100 mTorr.

Oxygen Pressure	Thickness (nm)	Resistivity (Ω-cm)
Single layer under 250mTorr	324.11	0.106
Single layer under vacuum	323.76	0.025
Bilayer of 250 mTorr and Vacuum	483.46	0.149

Table 6.1. List of samples and electrical resistivity values.

6.5. Conclusions

Single-layer and bilayer AZO films were deposited by PLD at various oxygen pressures. AZO films grown at different oxygen pressures result in different surface morphologies and microstructures, and thus different properties. The films grown at high oxygen regime have shown obvious nanorod structures with a large surface roughness. On the other hand, films grown in low oxygen pressure regime and vacuum show continuous layers with small surface roughness. The bilayer film deposited at vacuum and 250 mTorr sequentially grows as nanorods on top of a continuous layer. This suggests that the oxygen pressure plays a more important role on the growth morphology and the lattice parameters of AZO films than the substrate surface energy. The bilayer AZO films have strong potential in TCO layers with light-trapping function for thin film solar cells as they essentially combine high electrical conductivity of the continuous layer and high surface roughness of the top nanorod layer as the light-trapping layer.

(http://dx.doi.org /10.1088/0957-4484/20/39/395704)

CHAPTER VII

GROWTH OF AL-DOPED ZNO FILMS WITH TILTED NANO-COLUMNS ON R-CUT SAPPHIRE SUBSTRATES BY PULSED LASER DEPOSITION*

7.1. Overview

2wt% Al_2O_3-doped ZnO (AZO) thin films in both single layer and bi-layer forms were deposited on α-Al_2O_3 $(01\bar{1}2)$ (r-cut) and (0001) (c-cut) substrates by a pulsed laser deposition technique. Single layer AZO films were grown under either vacuum or 33.3 Pa of O_2 pressure. Bilayer AZO films were grown with a sequential deposition of a uniform template layer under vacuum and a nano-column-structured layer under 33.3 Pa of O_2 pressure. Interestingly, single layer AZO film grown on r-cut sapphire in high oxygen pressure (33.3 Pa) shows tilted grain boundaries along $[\bar{1}10\bar{2}]_{AZO}$. The bilayer film deposited on r-cut substrate shows tilted nano-column growth while the film grown on c-cut substrate has vertically grown nano-columns. The results of X-ray diffraction and cross-section transmission electron microscopy studies show a systematic variation of the d-spacing of $(0002)_{AZO}$ and $(11\bar{2}0)_{AZO}$ for all AZO films. Electrical resistivity was measured and found to be strongly dependent on the different microstructures achieved under different oxygen pressures and substrates.

---

*Reprinted from "Growth of Al-doped ZnO films with tilted nano-columns on r-cut sapphire substrates by pulsed laser deposition," by J. H. Lee, T. Lu, S. Cho, F. Khatkatay, L. Chen, H. Wang, Thin solid films (2012) in press Copyright (2012), with permission from Elsevier.

7.2. Introduction

Al-doped ZnO (AZO) as a transparent conducting oxide material has been widely explored for various applications, such as solar cells, light emitting diodes and transparent thin film transistors because of its unique optical and electrical properties, and especially its tunable nanostructures as nanorods, nanotubes, nanowires and nanobelts [195,196, 197, 198, 199, 200, 201,71]. Aluminum (Al) is a typical n-type dopant for ZnO, which is broadly used to increase the electrical conductivity [202, 203]. Other approaches to enhance the electrical conductivity are to employ different processing methods and deposition parameters. For example, the AZO film grown by magnetron sputtering at 350 °C showed the electrical resistivity in the range of $3\times10^{-4} \sim 6\times10^{-4}$ Ω·cm while a AZO film grown by chemical vapor deposition has resistivity values ranging from 4.6×10^{-3} to 1×10^{-1} Ω·cm [76, 77]. As the oxygen partial pressure increased from 0.133 to 13.33 Pa (from 1 to 100 mTorr), the resistivity increased drastically from 5.1×10^{-4} to 5.2 Ω·cm [78].

Besides optimizing its electrical conducting properties, there is a growing need on tuning the surface properties of the AZO films. For example, incorporating a light trapping layer for solar cells has been proposed for enhancing the solar cell efficiency [189, 204]. Recently most of the light trapping layers were introduced through anisotropic etching method using diluted hydrochloride (HCl). This method leads to high surface roughness to deflect the sun light [195]. However, it is time consuming by involving multiple steps of deposition, chemical etching process and lithography patterning. Recently several reports demonstrate that controlling the partial gas pressure can directly tune the microstructure and surface morphologies of thin films [197, 194, 205]. In isothermal condition, under the partial gas pressure, the grain size can be usually governed by mean free path of the mobile atoms [206-208]. The collisions between the atoms from the target and gas molecules reduce the mobility of the atoms and limit the nucleation size of the films on the substrate, which leads to the formation of nanorods/nano-columns. We have previously demonstrated that vertically aligned nano-columns can be formed in AZO films when they are deposited under high oxygen pressure larger than 26.66 Pa (200 mTorr) [209].

In this work we report the direct growth of tilted nano-columns of AZO films by a two-step template deposition method. In analogy to the abovementioned light trapping scheme with high surface roughness to deflect the sunlight, the inclined surface of these tilted nano-columns could possibly provide more effective light trapping scheme compared to the vertical ones. The films were grown as single layer or bilayer on α-Al_2O_3 $(01\bar{1}2)$ (r-cut) or (0001) (c-cut) substrates under different oxygen pressures. The resulted microstructures based on substrate types, growth parameters and layer structures were characterized by X-ray diffraction (XRD), transmission electron microscopy (TEM) (with selected area diffraction (SAD)) and scanning electron microscopy (SEM), and correlated with their electrical properties.

7.3. Experimental details

In a high vacuum chamber 2 wt% Al_2O_3-doped ZnO films were deposited on α-Al_2O_3 (r-cut) or (c-cut) single crystal substrate by a KrF excimer laser (Lambda Physik

210, = 248 nm, 10 Hz). The laser beam was focused to obtain an energy density of approximately 4 J/ cm^2 at 45° angle of incidence. The targets were hot pressed using a mixture of Al_2O_3 and ZnO powders and sintered at 1100 ^{o}C for 11 h in flow of oxygen. Different oxygen partial pressures, i.e., 33.3 Pa and vacuum, were applied to deposit the single layer film on α-Al_2O_3 r-cut substrates (176.8 nm thick with deposition rate of 0.98 Å/s under vacuum, and 206.9 nm thick with the rate of 3.4 Å/s under 33.3 Pa of O_2 pressure). Two bilayer samples were deposited; i.e., the first sample on α-Al_2O_3 r-cut substrate is a vacuum layer (107.9 nm thick with deposition rate of 1.8 Å/s) as the template and then a 33.3 Pa layer (321.8 nm thick with deposition rate of 5.4 Å/s), and the second sample on c-cut substrate has a 3.3 template (111.7 nm thick with deposition rate of 1.9 Å/s) and then a 33.3 Pa layer (347.5 nm thick with deposition rate of 5.8 Å/s). The substrate temperature was fixed at 750°C for all depositions. The back pressure of the system was at 1.3×10^{-5} Pa. TEM samples were prepared through a conventional procedure, including mechanical grinding, polishing, and ion milling, to be used for TEM study. Microstructural characterizations, using X-ray diffractometer (XRD, Bruker D8 Discover X-ray diffractometer with copper x-ray radiation under theta-2 theta configuration, operation voltage of 40 kV and current of 40 mA; 0.001° as step-size and 0.1 s per step were used in all scans), high resolution field emission scanning electron microscopes (FE-SEM, JEOL JSM-7500F with operation voltage of 5 kV) and transmission electron microscope (TEM, JEOL 2010 analytical electron microscope with a point-to-point resolution of 0.23 nm and operating voltage of 200 kV), were performed on all the single layer and bilayer thin films. Electrical resistivity was measured by a four point probe measurement system under room temperature along different in-plane directions. The resistivity-temperature dependence was conducted by a physical property measurement system (PPMS, Quantum Design, Inc.) using van der Pauw method.

7.4. Results and discussion

7.4.1. Microstructure and surface morphology

Figure 7.1a shows the XRD Θ ~ 2Θ scans of single layer AZO films deposited on r-cut sapphire under 33.3 Pa and vacuum. For both samples, AZO $(11\bar{2}0)$ peak is aligned with sapphire $(01\bar{1}2)$ peak indicating highly textured film along the out-of-plane direction of the substrate. As the oxygen pressure reduces from 33.3 Pa to vacuum, it is noticed that the peak position of AZO $(11\bar{2}0)$ shifts from 56.76° to 56.57°, i.e., the d-spacing of the AZO (0002) increases from 1.621 Å to 1.626 Å. Compared to the bulk value of ZnO $(11\bar{2}0)$ d-spacing, 1.625 Å [210], the film deposited under oxygen pressure is in compression while that under vacuum is in tension out-of-plane. Figure 7.1b shows the XRD Θ ~ 2Θ scans of two bilayer AZO films. The top plot is for the film with the first vacuum layer and the second layer deposited at 33.3 Pa on r-cut sapphire. The peak of AZO $(11\bar{2}0)$ is at 56.62° with a calculated d-spacing of 1.624 Å, which is close to the bulk value. The bottom plot shows the XRD scan for the bilayer film grown first under 3.3 and then 33.3 Pa of O_2 on c-cut sapphire. AZO (0002) peak is aligned well with sapphire (0006). The peak is at 34.44° with a calculated d-spacing of 2.602 Å. The peak intensity is higher than that in the films grown on r-cut sapphire. This suggests that AZO films on c-cut sapphire have a better crystallinity than that on r-cut sapphire. In our previous report [209], the bilayer film grown under vacuum for the first layer and 33.3 Pa (250 mTorr) for the second layer shows a peak split of AZO (0002). In this case, as the oxygen partial pressure for the first layer was adjusted to 3.3 Pa (Figure 7.1b), a single AZO (0002) peak was observed. The d-spacing of AZO (0002) peak, 2.602 Å, is close to that of the second layer grown with 33.3 Pa (250 mTorr) of O_2 (2.605 Å) from the previous study. This suggests that a little amount of oxygen presented during the first layer deposition could increase the d-spacing of the first layer and relax the film to its bulk value of ZnO (0002) d-spacing, 2.603 Å [210].

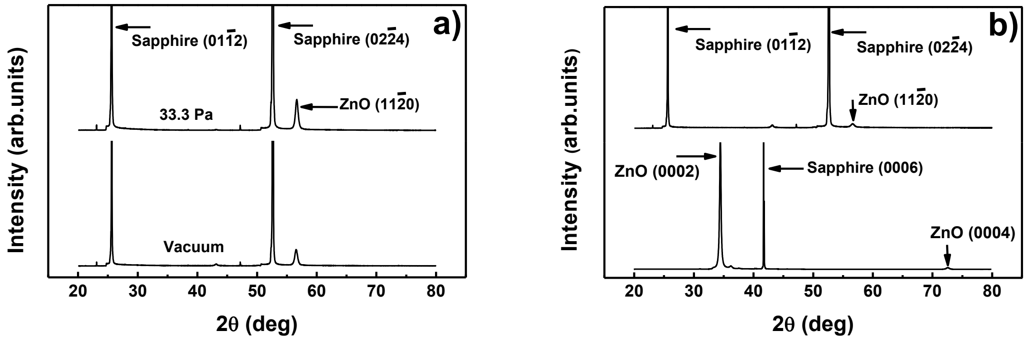

Figure 7.1. (a) XRD θ~ 2θ scans of AZO single layer films grown on α-Al_2O_3 $(01\bar{1}2)$ (r-cut) substrate under 33.3 Pa oxygen pressure and vacuum, and (b) XRD pattern of a bilayer films grown at vacuum and 33.3 Pa sequentially on α-Al_2O_3 $(01\bar{1}2)$ (r-cut) and at 3.3 and 33.3 Pa on (0001) (c-cut) substrates.

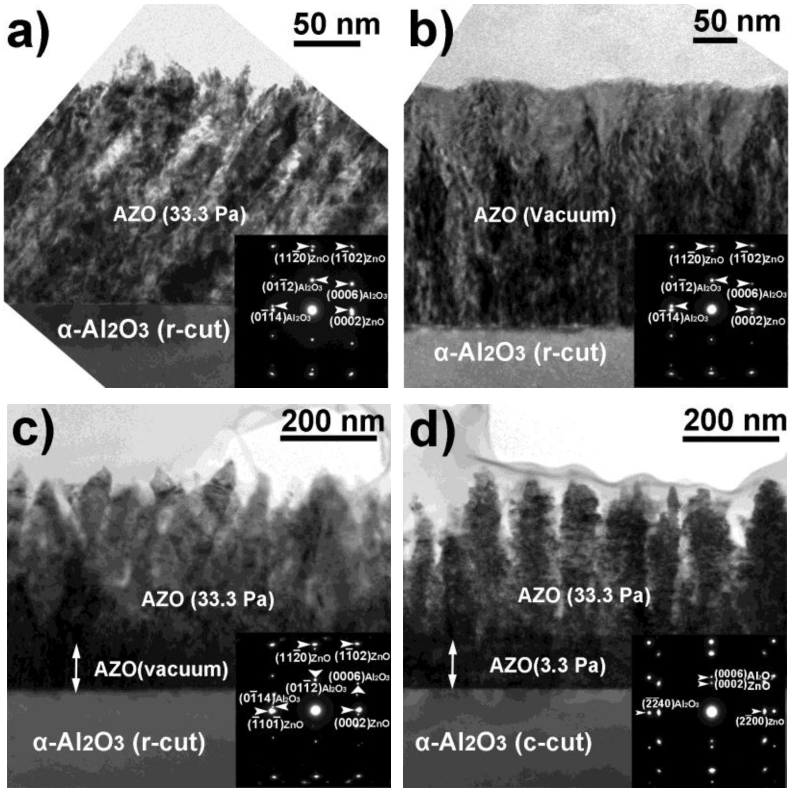

Figure 7.2. Cross-sectional TEM micrographs show the AZO single layers epitaxially grown on α-Al_2O_3 $(01\bar{1}2)$ (r-cut) substrate at the oxygen pressure of (a) 33.3 Pa and (b) vacuum, and the AZO bilayer grown with sequential deposition at oxygen pressures of vacuum and 33.3 Pa on (c) α-Al_2O_3 $(01\bar{1}2)$ (r-cut) substrate and 3.3 and 33.3 Pa on (d) α-Al_2O_3 (0001) (c-cut) substrate.

To fully understand the microstructure variation as functions of oxygen pressure and substrate type, a detailed cross-sectional TEM study for all the samples was conducted. Figure 7.2a and b shows the cross-section TEM images of single layer AZO films on r-cut substrates under 33.3 Pa and vacuum, respectively. The single layer film deposited under 33.3 Pa shows very evident tilted grain boundaries with the average grain size of around 27.53 nm. The tilted angle of the boundaries is about 52.76° regarding to the substrate surface, which corresponds to the extended direction of $[\bar{1}10\bar{2}]_{AZO}$. These tilted grain boundaries are possibly caused by the preferred growth orientation of the tilted grains, i.e., $[\bar{1}10\bar{2}]_{AZO}$. Further discussion on the grain orientation is given later. Figure 7.2b shows the single layer film deposited under vacuum. The film has no evident grain boundary observed which is similar to the microstructure of the AZO film grown under vacuum on c-cut substrate from our previous report [209]. Figure 7.2c and d shows bilayer AZO films on r-cut and c-cut substrates, respectively. For the bilayer film grown on r-cut substrate (Figure 7.2c), the vacuum layer is about 108 nm and a sequential layer deposited under 33.3 Pa of O_2 pressure is about 322 nm. For the other bilayer grown on c-cut substrate (Figure 7.2d), the layer under 3.3 is about 112 nm and the sequential layer under 33.3 Pa is about 348 nm. In both cases, the bilayers show evident nano-column growth on a thin smooth layer. More interestingly, while the bilayer on c-cut substrate shows vertically grown nano-columns, the one deposited on r-cut substrate has nano-columns grown with a tilted angle of 63.74° in regard to the substrate surface. This might be due to the different preferred growth orientations on two different substrates. The insets are corresponding SAD patterns for all the samples. It is noted that the epitaxial quality of all the films is highly evidenced by the distinguished diffraction dots from the films, despite the fact that they have very different film morphologies. Based on the above XRD and SAD analyses, schematic diagrams describing the orientation relationships for the single layer and bilayer films are presented in Figure 7.3a and b, respectively, both on r-cut substrate. For the single layer sample (Figure 7.3a) which is corresponding to the films in Figure 7.2a and b, the matching relationships are determined to be $(11\bar{2}0)_{AZO}//(01\bar{1}2)_{r\text{-cut}}$ and $[\bar{1}100]_{AZO}//[2\bar{1}\bar{1}0]_{r\text{-cut}}$. For the bilayer sample (Figure 7.3b) which is corresponding to the film in Figure 7.2c, the bottom smooth nanolayer has the same orientation as those of the single layer samples. However, the top nano-column layer shows a very different orientation, i.e., $(1\bar{1}01)_{AZO\ nano\text{-}column}//(0002)_{AZO\ nanolayer}$ and $[\bar{1}100]_{AZO}//[2\bar{1}\bar{1}0]_{r\text{-cut}}$.

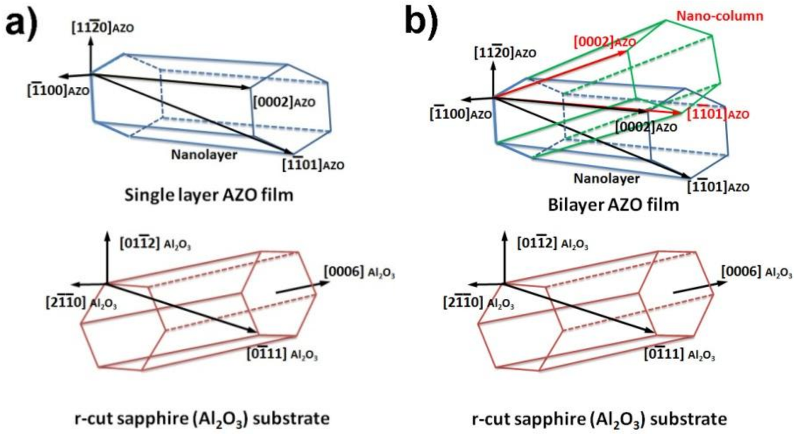

Figure 7.3. Schematic diagrams describe the orientation relationship between the film and the substrate for (a) single layer and (b) bilayer AZO films grown on α-Al_2O_3 ($01\bar{1}2$) (r-cut) substrate.

In addition to the evident morphology variation introduced by different oxygen pressures and substrates, a systematic variation of the d-spacing of AZO (0002) and (

$11\bar{2}0$) as a function of film geometry was found based on a detailed analysis of the corresponding SAD patterns. Based on the TEM SAD patterns and XRD plots, the d-spacings of AZO (0002) and ($11\bar{2}0$) were compared with their bulk values ($d_{ZnO\,(0002)\,bulk}$ = 2.603 Å and $d_{ZnO\,(11\bar{2}0)\,bulk}$ = 1.625 Å [208]) and plotted in Figure 7.4a and b, respectively. Figure 7.4a shows that the film deposited under vacuum has a smaller d-spacing of AZO [0002], i.e., in compression. However, as oxygen is introduced in the bilayer growth, the d-spacing starts to approach its bulk value and the film starts to be relaxed. For the bilayer grown on α-Al_2O_3 c-cut substrate the d-spacing increases to its bulk value. Finally, the single layer film grown under 33.3 Pa of O_2 pressure shows the film in tension. On the other hand, in Figure 7.4b the variation of d-spacing of ($11\bar{2}0$) shows exactly opposite trend, i.e., decreasing with increasing oxygen pressure.

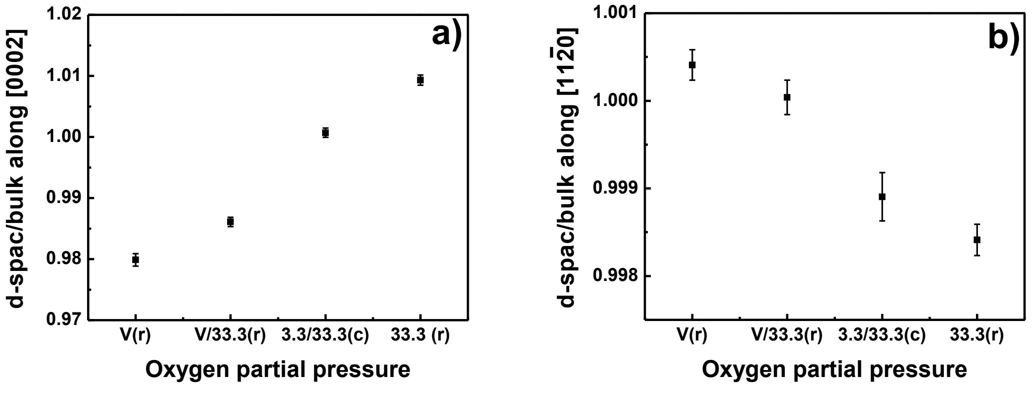

Figure 7.4. Plots show variation in d-spacing along AZO [0002] and [$11\bar{2}0$] as a function of oxygen pressure and effect of different substrates.

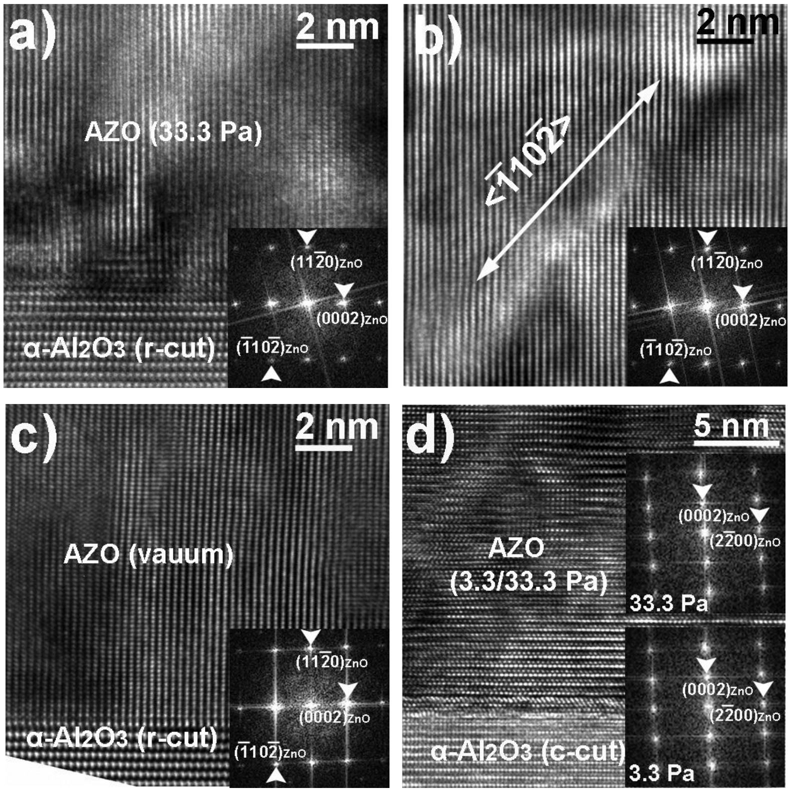

Figure 7.5. HRTEM images show the single layer AZO films grown on α-Al_2O_3 $(01\bar{1}2)$ (r-cut) substrate. (a) is for the film/substrate interface area and (b) is the area near the tilted grain boundary, both for 33.3 Pa sample. (c) is the film/substrate interface area for the vacuum sample, and (d) is the film/substrate interface region for the bilayer film grown on α-Al_2O_3 (0001) (c-cut) substrate. The insets are corresponding FFT diffraction patterns for each image.

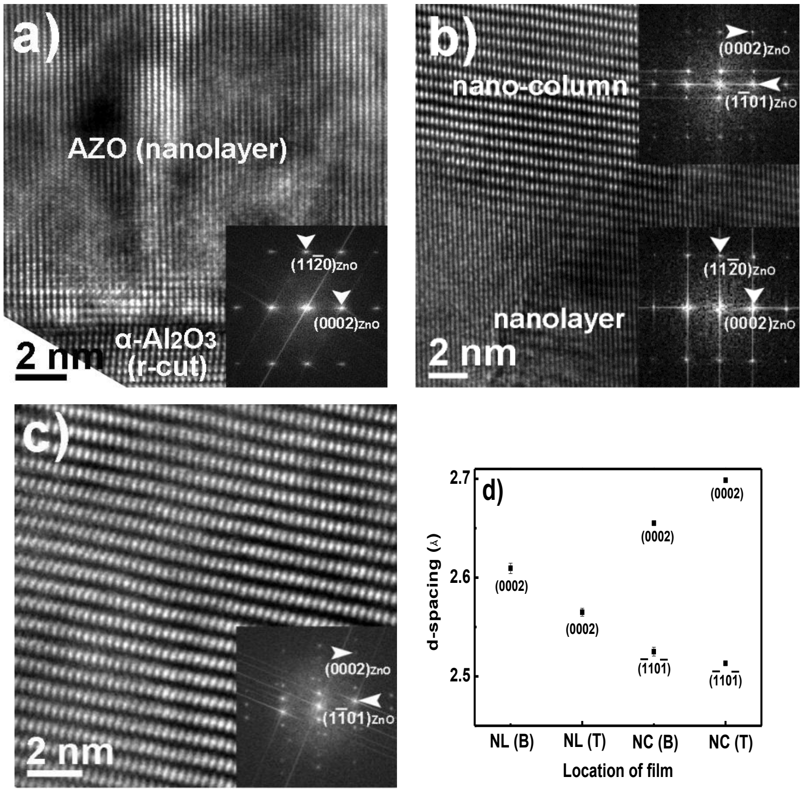

Figure 7.6. HRTEM images from the different areas of bilayer deposited on α-Al_2O_3 ($01\bar{1}2$) (r-cut) substrate under different oxygen pressures: (a) the vacuum layer and (b) the interface area between the vacuum and 33.3 Pa layers, and (c) the 33.3 Pa layer. The insets are the corresponding FFT diffraction patterns. The in-plane d-spacing variation is calculated on the areas along the film growth direction and plotted in (d), i.e., i) NL(B): the area right above the film/substrate interface, ii) NL(T): the area of film right below the nanolayer/nano-columns interface, iii) NC(B): the area right above the nanolayer/nano-columns interface and iv) NC(T): the area from the tip portion of the nano-columns.

To further elucidate the formation mechanism(s) of the tilted grain boundaries in the single layer film grown under 33.3 Pa of O_2 pressure and the bilayer films with tilted nano-columns, both on r-cut substrates, more detailed analysis with cross sectional high resolution TEM (HRTEM) and fast Fourier transform (FFT) analysis were performed on specific areas of the AZO films and presented in Figures 7.5 and 7.6. Figure 7.5a and b shows the HRTEM images of the single layer AZO film grown under 33.3 Pa of O_2 pressure. Figure 7.5a was taken near the interface area between the film and the substrate. A clear interface is observed without any evident intermixing. The inset is the corresponding FFT diffraction pattern of the area. In the film the evident lattice fringes of (0002) and $(11\bar{2}0)$ could be observed and measured as $d_{ZnO(0002)}$= 2.613 Å and $d_{ZnO(11\bar{2}0)}$= 1.646 Å, which are both in tension. Figure 7.5b shows a HRTEM image taken at a typical tilted grain boundary. Similarly in Figure 7.5a, evident lattice fringes are identified and the inset of FFT diffraction pattern shows clear diffractions from AZO (0002) and $(11\bar{2}0)$. Interestingly, $d_{ZnO(0002)}$ and $d_{ZnO(11\bar{2}0)}$ near the tilted grain boundary are calculated to be 2.581 Å and 1.618 Å, respectively. The values are about 1.2% and 1.7% smaller than the un-tilted area, for AZO (0002) and AZO $(11\bar{2}0)$, respectively. As a result of the d-spacing reduction in both in-plane and out-of-plane, the sum of the stress along $<\bar{1}10\bar{2}>$ is quite large (~2%) which might be the main driving force for the formation of the tilted grain boundaries. Interestingly, by forming the tilted grain boundaries, the resulted in-plane mismatching between the film and the substrate ($(1\bar{1}04)_{sapphire}$//$(0002)_{AZO}$) is reduced from 2.4% to 1.2%, based on the following measured d-spacing values, $d_{\text{sapphire}(1\bar{1}04)}$ = 2.550 Å, $d_{\text{ZnO}(0002)\text{ without tiled boundary}}$ = 2.613 Å and $d_{\text{ZnO}(0002)\text{ with tiled boundary}}$ = 2.581 Å. Figure 7.5c shows the HRTEM image of the film grown under vacuum with high epitaxial quality, and the inset corresponds to the FFT diffraction pattern of the area. Similarly, the film grown under vacuum also shows evident lattice fringes and diffraction dots corresponding to (0002) and $(11\bar{2}0)$. In Figure 7.5d HRTEM image of the AZO bilayer film grown on c-cut substrate was taken near the interface and shows high quality epitaxial growth of the film. The insets correspond to the FFT diffraction patterns of the nano-columns layer (top) and the nanolayer (bottom). In both nano-columns and nanolayer FFT patterns, very clear (0002) and $(2\bar{2}00)$ diffractions are observed and the corresponding d-spacings are calculated to be $d_{\text{ZnO}(0002)\text{ nano-columns}}$ = 2.611 Å and $d_{\text{ZnO}(0002)\text{ nanolayer}}$ = 2.630 Å, and $d_{\text{ZnO}(2\bar{2}00)\text{ nano-columns}}$ = 1.404 Å and $d_{\text{ZnO}(2\bar{2}00)\text{ nanolayer}}$ = 1.399 Å.

Figure 7.6 shows the HRTEM images of the bilayer sample on r-cut substrate, from (a) nanolayer/substrate, (b) nano-columns/nanolayer, and (c) nano-columns areas. It is clear that within each region grown under different oxygen partial pressures the sample has high crystallinity. However, via the interface the change of the orientation in the AZO film is observed. Based on the FFT inset, the nano-column grown under high oxygen pressure shows an interesting 62.51° counter clockwise rotation of [0002] in regard to $[1\bar{1}01]$. The tilted angle is very close to the observed tilt angle (63.74°) in Figure 7.2c. As a result of d-spacing measurement based on the FFT diffraction pattern, it reveals that there is a variation of in-plane d-spacing along the film growth direction. The in-plane d-spacing, $d_{\text{ZnO}(0002)}$, of the nanolayer near the substrate is 2.609 Å (Figure

7.6a and d). Then it is reduced to 2.565 Å for the area right below the interface between the nanolayer and the nano-columns (Figure 7.6b and d). In the nano-columns grown under high oxygen pressure, the $d_{ZnO\,(0002)}$ was increased to 2.656 Å right above the interface between the nanolayer and the nano-column (Figure 7.6b and d). Then the $d_{ZnO\,(0002)}$ was further increased to 2.700 Å near the tip area of the nano-columns (Figure 7.6c and d). At the same time, the in-plane d-spacing, $d_{ZnO\,(1\bar{1}01)}$, of 2.525 Å for the nano-columns area right above the interface decreases to 2.513 Å for the tip area (Figure 7.6d). $d_{ZnO\,(0002)}$ is compressed for the layer under vacuum; but for the film deposited under high oxygen pressure, the $d_{ZnO\,(0002)}$ is in tensile. As a result, the lattice strain between $d_{ZnO\,(0002)\,nanolayer}$ and $d_{ZnO\,(0002)\,nano\text{-}columns}$ increased to 3.43%. Instead, the lattice strain between $d_{ZnO\,(0002)\,nanolayer}$ and $d_{ZnO\,(1\bar{1}01)\,nano\text{-}columns}$ is 1.58 %. This lattice strain difference between the above two cases might be one of the main reasons for the formation of the tilted nano-columns on top of the template layer but with very different lattice orientations, i.e., $(1\bar{1}01)_{AZO\ nano\text{-}columns}//(0002)_{AZO\ nanolayer}$. A similar tilted growth structure induced by strain has been reported previously [211-213]. This result suggests that it is highly possible to manipulate the AZO nano-columns growth as well as their tilting angles based on the growth orientations and oxygen pressures.

Overall surface morphology studies for all samples were conducted by SEM and presented in Figure 7.7. Figure 7.7a shows the surface morphology of the single layer AZO film deposited under 33.3 Pa of O_2 pressure on r-cut substrate. There are very evident tilted nano-columns observed with triangular shape. Interestingly, the nano-columns are ordered distributed on the surface. In contrast, the film deposited under vacuum shows a very smooth structure without any evident surface features observed (Figure 7.7b). The surface morphologies of the bilayer grown on α-Al_2O_3 r-cut and c-cut substrates show very evident nano-column structures on the surfaces (Figure 7.7c and d). The nano-columns on r-cut are elongated to a certain direction marked by the arrow in Figure 7.7c. The feature is consistent with the above TEM results.

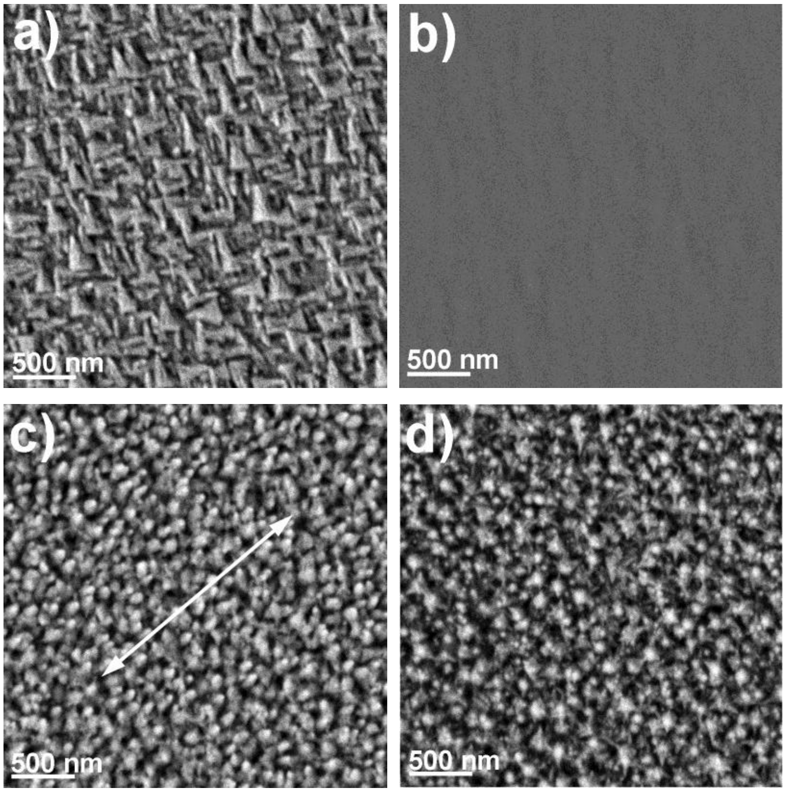

Figure 7.7. SEM images show the different surface morphologies of AZO films grown at (a) 33.3 Pa, (b) vacuum and (c) the bilayer of vacuum and 33.3 Pa on r-cut substrate, and (d) the bilayer of 3.3 and 33.3 Pa on c-cut substrate.

7.4.2. Electrical properties

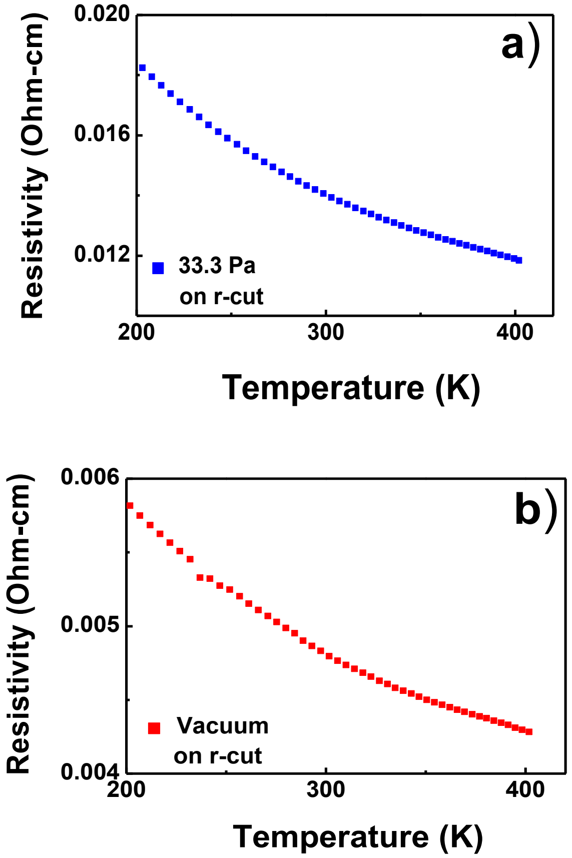

Figure 7.8. Plots show the electrical resistivity values of AZO films grown at a) 33.3 Pa and b) vacuum on r-cut substrate. The values are measured along the variation of the temperature in the range of 200~400K.

To clarify the effect of variation of microstructure and surface morphology of the AZO films on the electrical properties, electrical resistivity was first measured by a four point probe system at room temperature. Data is summarized in Table 7.1. For the single layer deposited under vacuum, the electrical resistivity was around 1 mΩ-cm while the single layer deposited under high oxygen pressure regime (33.3 Pa) shows increased value with around 9.8 mΩ-cm. The resistivity measurement along different orientations in-plane for the films was conducted to explore the possible in-plane anisotropic properties. No obvious differences were observed for all the tested samples. Similarly, the temperature dependent electrical resistivity for both AZO films grown at 33.3 Pa and vacuum on r-cut substrate has been measured and plotted in figure 7.8. It shows the decrease of the resistivity values as the temperature increases from 200 K to 400 K following a typical semiconductor behavior. The reduced electrical resistivity in the single layer sample grown under vacuum is because of less grain-boundary-induced scattering similar to previous reports [214-216]. The tilted grain boundaries in the film grown under high oxygen pressure could enhance the scattering and therefore lead to the increased resistivity. But interestingly, compared to the electrical resistivity of the single layer grown on α-Al_2O_3 (0001) (c-cut) substrate from previous study (25 mΩ-cm for single layer under vacuum) [209], the film on r-cut substrate shows significantly reduced values. This suggests that the electrical transport could prefer a certain in-plane orientation on the AZO film, i.e. $(11\bar{2}0)_{AZO}$ rather than $(0001)_{AZO}$. The bilayer deposited on r-cut substrate has 104.5 mΩ-cm while 112.9 mΩ-cm was measured for the bilayer sample deposited on c-cut substrate (Table 7.1). This is because nanopillar structure limits the electrical transport along in-plane direction and the thickness of the nanolayer is quiet small (~110 nm). It is noted that the films were all deposited under a high temperature of 750°C where a possible deterioration of the Al doping distribution could occur and lead to a lower conductivity. Further optimization on the growth temperature is underway to achieve the tilted nanopillar films with a better electrical conductivity.

Sample Information	**Thickness (nm)**	**Uniform Layer Thickness (nm)**	**Resistivity (Ω-cm)**
Vacuum (r)	**176.75**	**-**	**0.0010**
33.3 Pa (r)	**206.87**	**-**	**0.0098**
Vacuum/ 33.3 Pa (r)	**429.68**	**107.96**	**0.1045**
3.3/ 33.3 Pa (c)	**459.25**	**111.74**	**0.1129**

Table 7.1. List of the samples and their electrical resistivity values.

7.5. Conclusions

Both oxygen pressure and substrate orientation play a very important role on the overall microstructure and electrical properties of the AZO films. On r-cut sapphire substrates, single layer AZO films grown under high oxygen pressure (33.3 Pa) show the tilted grain boundaries possibly induced by internal lattice strain while the film deposited under vacuum shows no evident grain boundaries. Bilayer AZO films were deposited sequentially with a uniform vacuum layer first followed by a nano-column layer under 33.3 Pa of O_2 pressure on both c-cut and r-cut substrates. The tilted nano-columns in bilayer sample on r-cut substrate grow along AZO [0002] which results in a tilt angle of 63.74° in regard to the substrate surface. This tilted nano-column structure could minimize the lattice strain between the in-plane lattices of the nanolayer and the nano-columns. Electrical resistivity of the single layer on r-cut substrate is significantly smaller (25 times) than that on the c-cut substrates. It suggests that higher conductivity values can be achieved in AZO films with the electrical path along $(11\bar{2}0)_{AZO}$. More interestingly the self-assembled tilted nano-columns can be formed by properly selected AZO growth orientation and oxygen pressures. These structures could find unique applications for light trapping schemes in future thin film solar cells.

CHAPTER VIII

DIRECT OBSERVATION OF DEFORMATION BEHAVIOR OF AL DOPED ZNO NANORODS GROWN WITH DIFFERENT WIDTH/LENGTH RATIOS

8.1. Overview

In situ TEM nanoindentation has been conducted to explore the size dependent deformation behavior of two different types (type I and II) of 2wt% Al_2O_3-doped ZnO (AZO) nanorods. The AZO films are grown on α-Al_2O_3 (0001) (c-cut) substrates under 250 mTorr of O_2 pressure by a pulsed laser deposition technique. Type I has grown with a width/length ratio of ~0.51 while type II nanorod has ~0.88 ratio. During the indentation on the type I nanord structure, annihilation of defects has been observed which is caused by limitation of the defect activities by relatively small size of the width. On the other hand, the type II nanorod shows dislocation activities which enhance the grain rotation under the external force applied on more isotropic direction through the type II nanorod.

8.2. Introduction

As a transparent conducting oxide material, ZnO has been broadly employed on various applications, such as solar cells, light emitting diodes and transparent thin film transistors, due to its unique optical and electrical properties [215, 68, 217, 197]. Especially, as a direct bandgap semiconductor with a bandgap of 3.4 eV, ZnO can be used for optoelectronic devices operating in the blue to UV regime [218, 219]. Usually for n-type ZnO, ZnO is usually doped with group III elements, B, Al, Ga and In to increase its electrical conductivity [220, 73,178, 217]. Among those, Al is one of the most typical dopant for n-type ZnO film as result of high transmittance and electrical conductivity of Al doped ZnO (AZO).

More potentially, the microstructure of AZO can be tuned to nanorod, nanowire or nanotube under different processing conditions. It has been recently reported that microstructure can be tuned under various partial gas pressures during the deposition process with which the grain size can be determined by mean free path of adatoms [194, 205, 206]. For example, Lee et al. demonstrated that during the pulsed laser deposition (PLD) processing vertical aligned AZO nanorods were grown in 250 mTorr of oxygen partial pressure while smooth continuous layer has been formed under vacuum [209].

Once the size of two dimensional thin film nanostructure is reduced to one dimensional nanorod structure, it is necessary to address the physical properties of the AZO nanostructure. For example, the deformation behaviors of the nanorod structures are crucial for mechanical manipulation for future nano-electromechanical systems (NEMS), using ZnO nanostructures [222, 223]. Recently several research reports introduced interesting results from mechanical tests on ZnO nanostructures, e.g. phase transition from wurtzite to body centered tetragonal structure during the tensile test on ZnO nanorod [224], size dependent ZnO nanostructure deformation behavior such as a significant increase in both elastic modulus [225] and fracture strain [226] with the reduction of its diameter size.

In spite of that, the recent development of *in situ* TEM technique has brought research opportunities in real time dynamic and quantitative studies under TEM column. Lately, during *in situ* TEM deformation on ZnO nanowire, observations of size dependent fracture processing during the tensile test [90] and transition from crystalline to amorphous structure during compressive and bending test [89] have been reported.

In this work we have conducted *in situ* TEM nanoindentation on two different types of AZO nanorods with different ratios of width/length (w/l), (type I: $l >> w$ and type II: $l \geq w$), grown on c-cut sapphire substrate to explore the size dependent deformation behavior of AZO nanorod structures. During the indentation on the type I AZO nanorod, relatively small size of the width limits the defect activity during the deformation and finally size confinement induces annihilation of the defects. Meanwhile, more defect activities have been observed during the indentation on type II nanorod, which enhances the grain boundary activity by grain boundary shear.

8.3. Experimental details

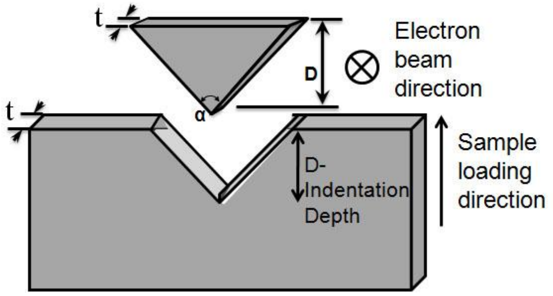

Figure 8.1. A schematic diagram illustrates *in situ* nanoindentation experimental setup, including the sample, electron beam and naoindenter tip (a wedge shape tip) positions, and sample moving direction.

In a high vacuum chamber, depositions of 2 wt% Al_2O_3-doped ZnO films on α-Al_2O_3 (c-cut) single crystal substrate were performed by pulsed laser deposition (PLD) with a KrF excimer laser (Lambda Physik LPX210i, = 248 nm, 10 Hz). The laser beam was focused to obtain an energy density of approximately 4 J/cm^2 at a 45° angle of incidence. The targets were hot pressed using a mixture of Al_2O_3 and ZnO powders and sintered at 1100 ^{o}C for 11 hours in flow of oxygen. The substrate temperature and oxygen pressure were fixed at 750 °C and 250 mTorr of O_2 pressure for deposition. The back pressure of the system was at 1 $\times 10^{-7}$ Torr before oxygen was introduced. Post-annealing was performed under 750 °C and 100 Torr of O_2 pressure for 30 minutes after deposition. TEM samples were prepared through a conventional procedure, including mechanical grinding, polishing, and ion milling, to be used for both conventional TEM and *in situ* TEM studies. *In situ* nanoindentation was conducted using an *in situ* nanoindentation holder (NanoFactory, Inc.). The sample is controlled in three dimensions by a piezoelectric actuator. Both conventional TEM and *in situ* TEM analyses were conducted on a JEOL 2010 analytical electron microscope with a point-to-point resolution of 0.23 nm. Images and movies during indentation events were recorded using a built-in CCD camera in the microscope. For the *in situ* nanoindentation experiment, indentation experiments were performed with a wedge-shaped diamond tip (tip radius of ~100 nm and tip angle of ~50.5°) for standard load-displacement measurements within TEM column. *In situ* movies and images were taken during the loading and unloading processes under the experimental setup described in Figure 8.1. During the indentation experiment, the nanoindentation tip was fixed while the sample was moved toward the tip by a piezoelectric stage in a precision movement as fine as 0.1 nm/step. During the loading process, a constant loading rate of 10 nm/s and a holding time of 15 ms were used for all of the indentation experiments. For the *in situ* experiments, a maximum depth of 50 nm was used to protect the tip from damage.

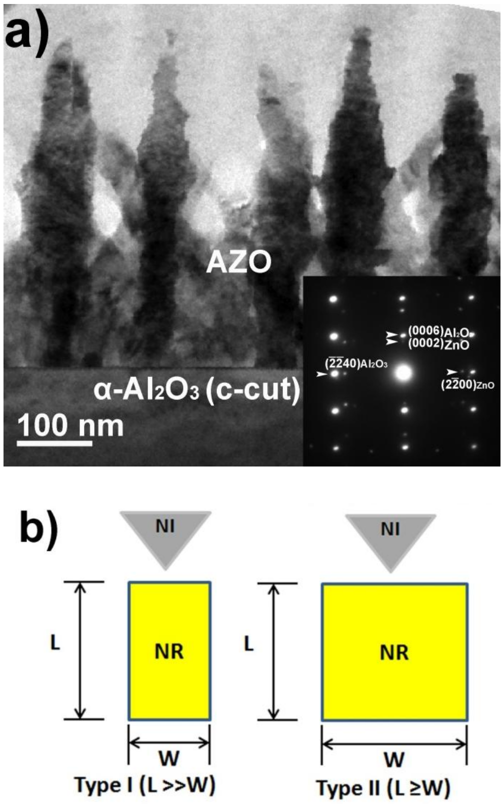

Figure 8.2. (a) Cross-sectional TEM micrograph shows the AZO single layer epitaxially grown on α-Al_2O_3 (0001) (c-cut) substrate at the oxygen pressure of 250mTorr. (b) Schematic diagrams describe two different types of nanorod structures with different ratios of width/length (*w/l*), e.g. (i) for type I size of length is much larger than that of width with *w/l* ratio of ~0.51 and (ii) for type II size of width and length are on similar range with *w/l* ratio of ~0.88, selected for *in situ* TEM nanoindetation.

8.4. Results and discussion

Figure 8.2a shows the cross-section TEM image of single layer AZO films on c-cut sapphire substrate under 250 mTorr of O_2. It is very obvious that the film is grown as nanorods along [0001] on the substrate. The inset is corresponding selected area diffraction (SAD) pattern for the sample. It is noted that the epitaxial quality of the film is high, shown by the distinguished diffraction dots from the film. In order to explore the size dependent deformation behavior of AZO nanorods, two different types of nanorod have been selected for the *in situ* TEM nanoindentation. Figure 8.2b shows the two different *w/l* ratios of nanorods and indentation direction. For type I, size of nanorod width is much smaller than that of the length while the type II shows that the size of width becomes similar to that of length. Therefore, it is expected that during the indentation process, different deformation behaviors in two different types of nanorods could be driven by different defect activities which can be controlled by the width of the nanorods.

To investigate size dependent deformation behavior of two different types of AZO nanorods, *in situ* TEM nanoindentation on AZO samples has been performed in TEM column while the deformation behaviors were captured on video. The loading process at a constant displacement rate continues up to 50 sec, followed by an unloading process at the same rate of 1 nm/sec. During the loading-unloading experiments, a set of typical force-displacement plots from two different geometries of AZO nanorods has been conducted. For the indentation on the type I nanorod, nanorod with *w/l* ratio of 0.51 with length and width of about 308 and 157 nm has been selected. Figure 8.3a-f are the snapshots taken during the indentation normal to the AZO (0001) plane. Figure 8.3a-d were captured during the loading process between 0 and 50 s, and Figure 8.3e was taken right after the maximum load. Finally, Figure 8.3f was taken after the indentation.

Before the indentation, in Figure 8.3a a lot of defects are observed over the entire nanorod structure. Once the indentation has been initiated, density of defects in the top area of the nanord marked by the red dashed circle in Figure 8.3a becomes decreased at the 18.81 sec. And at 25.52 sec it is noticed that movement of defects is more active with dark contrast in the center of the nanorod while top portion (right below the indenter tip) is cleaner with bright contrast. Then after the yielding initiated at about 37 sec in figure 8.3g and h, at 39.28 sec even boarder area right under the indenter tip within circled area becomes cleaner. It might be possible because before defects interact and multiply with other defects, they could leave from the free surface of the crystal as the size of width becomes relatively smaller than that of length, which is similar to previous reports [81, 102]. Finally, near the maximum load at 50.36 sec, about upper half of the nanorod structure becomes much cleaner than previous condition during the loading process. Additionally, it has been noticed that through yielding, significant deformation behavior from lower half of the nanorod was observed, which could be induced as at the yield point the dislocation penetration through the boundaries marked with A and B in figure 8.3c. More noticeably, after indentation, lower portion of the nanorod still have a lot of defects, but top area right below the indenter tip is very clean with less defect compared to the its initial condition in figure 8.3a. Finally, it can be concluded that during the indentation on the nanorod with *w/l* ratio of 0.51, relatively small size of width could confine the activation of the defects; thus, annihilation of defects has been led by their escape from the crystal surface.

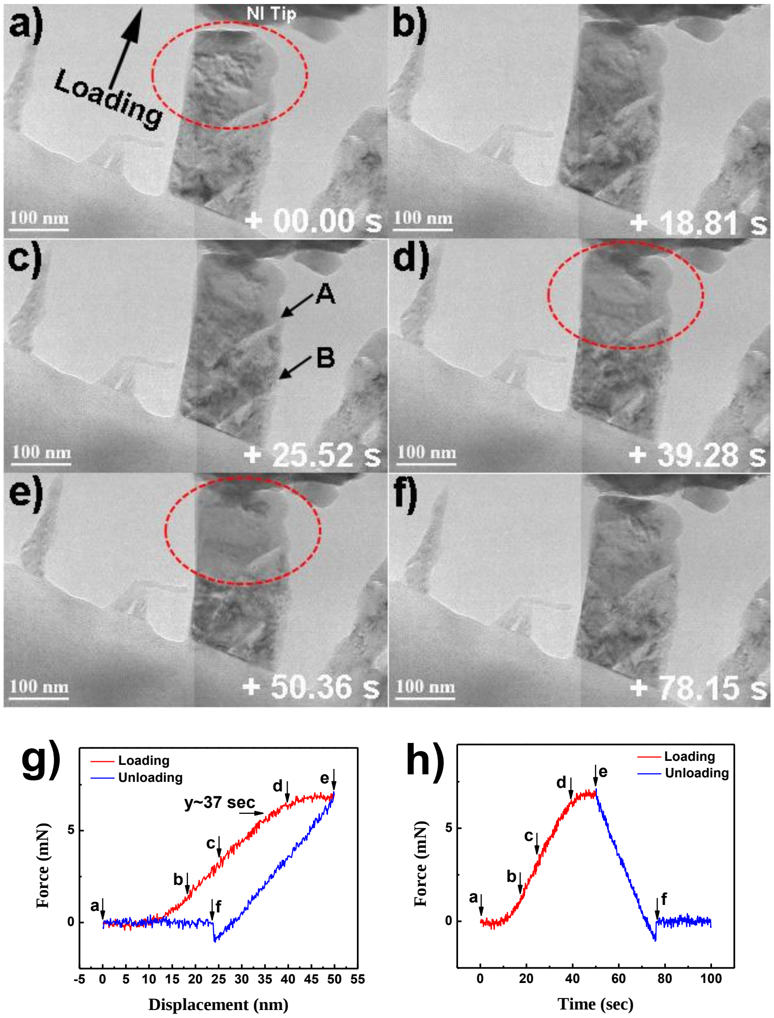

Figure 8.3. A detailed study of deformation mechanism was carried out by correlating the force–displacement plot with the movie snapshots for indentation on type I AZO nanorod. A set of movie frames during indentation on AZO (0001) is shown in (a) before indentation, (b), (c) and (d) during loading process, (e) right after maximum load, and (f) after indentation. The corresponding image letters are labelled on the (h) force–displacement and (g) force–time plots. (Based on instrument specifications, the estimated measurement error of force is ±5 %.)

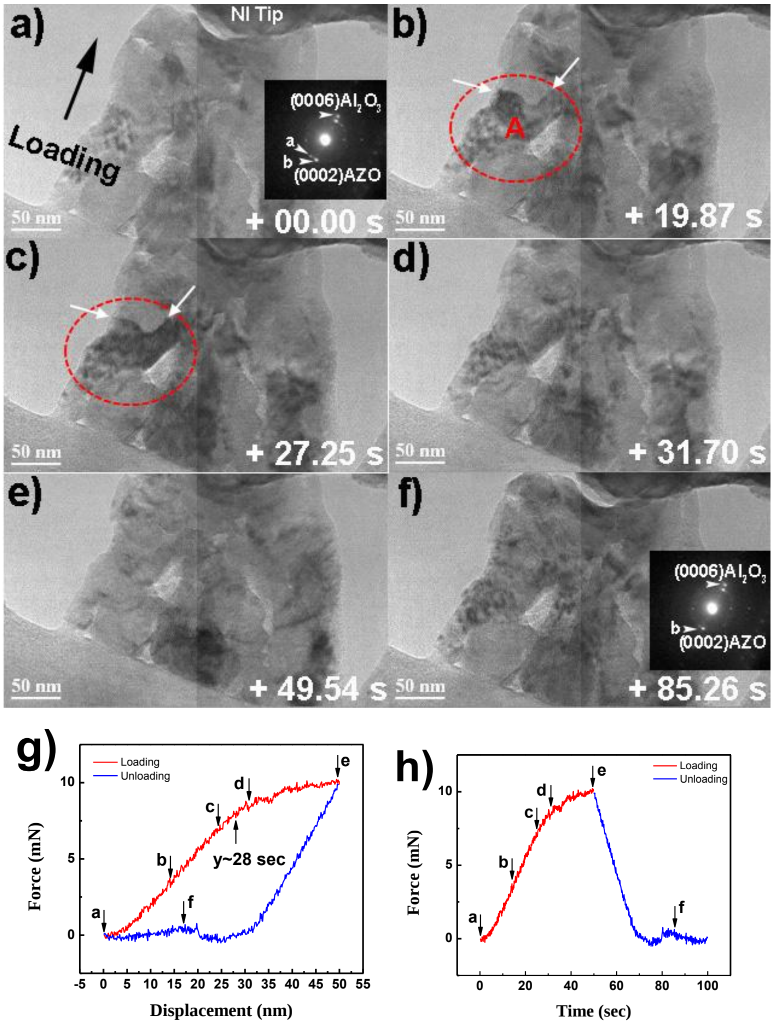

Figure 8.4. During indentation on type II AZO nanorod, a set of movie frames was captured in (a) before indentation, (b), (c), (d) and (e) during loading process, (f) after indentation. The corresponding image letters are labelled on the (h) force–displacement and (g) force–time plots. (Based on instrument specifications, the estimated measurement error of force is ±5 %.)

On the other hand, for the type II nanorod, several type I nanorods have been conglomerated during the deposition and postannealing processes; then finally, a type II nanorod with length of 261 nm and width of 232 nm could be formed. As the *w/l* ratio of type II nanorod becomes much greater than that of type I nanorod, more active microstructural evolution by defect activities on isotropic direction would be expected in type II nanorod structure unlike the limited defect activation on the anisotropic direction in type I. Figure 8.4a-e were taken during the loading process between 0 and 50 s, and Figure 8.4f was taken after the indentation. Before indentation in Figure 8.4a, based on the inset of SAD pattern, two bright dots (indexed with 'a' and 'b') of AZO (0002) are observed, which are possible from differently oriented grain structures. Once the indentation process has been initiated, at 19.87 sec activation of defects is observed. Especially, in the grain A within the circled area, contrast becomes dark, which possibly induced by high density of mobile dislocations piled up at the grain boundary indicated by white arrows. Then right before the yield point (y ~28 sec in figure 8.4g), at 27.25 sec as the dark contrast completely dominates the upper area of grain A. After the yield point, as the dislocations penetrate through the grain boundary, the grain boundary of the grain A becomes blurred. Then up to near the maximum load at 49.54 sec, as severe plastic deformation has been accompanied along the grain A, the grain boundary has been completely disappeared. Finally, after the indentation, in figure 8.4f it has been observed that in the inset of SAD pattern 'a' of AZO (0002) has been vanished and small textured structure has been formed with single dot 'b' of AZO (0002). This strongly suggests that during dislocation piling up at the grain boundary of grain A, internal stress exerted on the boundary could be high enough to lead rearrangement of lattices near the boundary during grain rotation of grain A through the yielding. Finally, it can be explained that as the *w/l* ratio has exceed much more than 50%, more isotropic geometry of nanorod allows more defect activity over broad range of structure. Therefore, increased internal stress induced by higher density of the defects in the grain with size of ~110 nm perhaps promotes grain boundary shear under which the grain and grain boundary activities could be observed as dominating the deformation behavior of type II nanorod structure. Although this phenomenon has been suggested in nanostructured copper by Conrad [53], by the *in situ* TEM nanoindentation, we could demonstrate that such high stress from high detect density could possibly lead similar process in a ceramic material.

8.5. Conclusions

Two different types of AZO nanorod with different *w/l* ratios (*w/l*: 0.51 for type I and 0.88 for type II) were prepared by PLD for direct observation of size dependent deformation behavior during *in situ* TEM nanoindentation. During the indentation on the type I nanorod structure, relatively small size of width could limit the activation of the defects which inducing their annihilation. On the other hand, type II nanorod formed with conglomerating several type I nanorods showed that as the external force spreading on the isotropic direction, broad range of dislocation activities has been observed, which is accompanied with the grain boundary shear during dislocation piling up at a grain boundary, enhancing the grain rotation. Briefly, the *in situ* TEM experiment recorded the two different size dependent deformation behaviors of nanorods and revealed the importance of controlling their width size for various application under which different deformation mechanisms are required.

CHAPTER IX

SUMMARY

The following list summarizes the deformation behaviours of :

AZM: Fully dense AZM ceramic nanocomposites were consolidated by SPS and prepared for the *in situ* nanoindentation experiment in a TEM column. Through conventional TEM study, we observed a unique "necklace" grain structure with bi-modal grain size distribution, where all the large white grains (Al_2O_3 and $MgAl_2O_4$) are surrounded by small ZrO_2 grains. Through *in situ* nanoindentation experiment, we monitored the grain activities during deformation. We found that in certain areas where a clear 'necklace' structure exists, the region mainly went through elastic deformation, i.e., the grains recover to their original alignment after indentation by the assistance of the strong grain activities in the small ZrO_2 grains. In other regions where mainly the hard Al_2O_3 and soft $MgAl_2O_4$ grains exist, a certain amount of plastic deformation was observed and the grains undergo a series of grain rotation, grain-boundary sliding, and realignment. This experiment demonstrates elastic and plastic deformation through grain and grain boundary activities in local grain areas of multi-phase ceramic nanocomposites at room temperature. This *in situ* study could provide useful insight for future designs of ceramic nanocomposites with superplasticity.

YBCO twins: A series of YBCO thin films with various film thicknesses were prepared by PLD for conventional nanoindentation and *in situ* nanoindentation in TEM column. Through conventional nanoindentation, we observed that the indentation hardness on the (110) planes is about 50% larger than that on the (001) planes. Consistently through the *in situ* nanoindentation experiments, the mean stresses at maximum loads is 11.14 GPa for indentation on (110) planes and 7.95 GPa for indentation on (001) planes, which results in a 40% increase in the maximum load. Through detailed analysis using *in situ* movies, we found that during deformation, a certain portion of the twin structures reverses the contrast; more interestingly, variations in the width of the twin boundaries during the loading and unloading process were observed. This suggests that twin interfaces act as effective barrier for external stress and therefore enhance the mechanical strength of HTS YBCO films, in the direction perpendicular to the twin interfaces by accommodating the external stress through twins.

Nc Nickel: *In situ* nanoindentation experiment shows solid evidence for significant work hardening in nc Ni based on sequential loading-unloading cycles. During work hardening, the dislocation density along the TB increases, and the yield strength increases gradually by ~40 %. Frequent formation of L-C locks were identified in grain interior and along twin boundaries. L-C locks are effective barriers to dislocations and lead to work hardening. Several mechanisms of interaction between L-C locks and twin boundaries were identified which provide important insight to understand plasticity in nc metals.

AZO nanorods: Two different types of AZO nanorod with different *w/l* ratios (*w/l*: 0.51 for type I and 0.88 for type II) were prepared by PLD for direct observation of size dependent deformation behavior during *in situ* TEM nanoindentation. During the indentation on the type I nanord structure, relatively small size of width could limit the activation of the defects which inducing their annihilation. On the other hand, type II nanorod formed with conglomerating several type I nanorods showed that as the external force spreading on the isotropic direction, broad range of dislocation activities has been observed, which is accompanied with the grain boundary shear during dislocation piling up at a grain boundary, enhancing grain rotation. Briefly, the *in situ* TEM experiment recorded the two different size dependent deformation behaviours of nanorods and revealed the importance of controlling their width size for various application under which different deformation mechanisms are required.

REFERENCES

[1] R. Chau, S. Datta, M. Doczy, B. Doyle, J. Jin, J. Kavalieros, A. Majumdar, M. Metz, M. Radosavljevic, *IEEE Trans. Nanotechnol.* 4 (2005) 153.

[2] L. Lu, Y. Shen, X. Chen, K. Lu, *Science* 304 (2004) 422-426.

[3] L. Lu, X. Chen, X. Huang, K. Lu, *Science* 323 (2009) 607-610.

[4] Y. Wang, M. Chen, F. Zhou, E. Ma, *Nature* 419 (2002) 912-915.

[5] K. Nihara, J. *Ceram. Soc. Jpn.* 99 (1991) 974-982.

[6] A. Mukhopadhyay, B. Basu, *Int. Mater. Rev.* 52 (2007) 257-288.

[7] H. Hahn, P. Mondal, K.A. Padmanabhan, *Nanostruct. Mater.* 9 (1997) 603-606.

[8] S. V. Bobylev, A. K. Mukherjee, I.A. Ovid'ko, *Rev. Adv. Mater. Sci.* 19 (2009) 103-113.

[9] M. A. Meyers, A. Mishra, D.J. Benson, *Prog. Mater. Sci.* 51 (2006) 427-556.

[10] S. J. Tans, M. H. Devoret, H. Dai, A. Thess, R. E. Smalley, L. J. Geerligs, C. Dekker, *Nature* 386 (1997) 474.

[11] Y. Cui, C. M. Lieber, *Science* 291 (2001) 851.

[12] A. K. Geim, K. S. Novoselov, *Nature Mater.* 6 (2007) 183

[13] J. C. H. Spence, *Experimental high-resolution electron microscopy*. (Oxford U. Press, New York, 1988).

[14] J. S. Wall, J. F. Hainfeld, *Annu. Rev. Biophys. Biophys. Chem.* 15 (1986) 355−376.

[15] R. F. Egerton, *Electron Energy Loss Spectroscopy in the Electron Microscope*, 2nd ed., (Plenum, New York, 1996).

[16] M. Wall, U. Dahmen, *Microsc. Microanal.*3 (1997) 593.

[17] Z. Y. Tang, N. A. Kotov, *Adv. Mater.* 17 (2005) 951-962.

[18] S. Kuchibhatla, A. S. Karakoti, D. Bera, S. Seal, *Prog. Mater Sci.* 52 (2007*)* 699.

[19] H. Gleiter, *Acta Mater.* 48 (2000) 1.

[20] B.N. Kim, K. Hiraga, K. Morita, Y. Sakka, *Nature* 413 (2001) 288.

[21] L. Samuelson, *Mater. Today* 6 (2003) 22–31.

[22] M. J. Zehetbauer, Y. T. Zhu, *Bulk Nanostructured Materials,* (Wiley-VCH, Weinheim, 2009).

[23] H. J. Chen, W. M. Rainforth, W. E. Lee, *Scripta Mater.* 42 (2000) 555.

[24] G. Zhan, A. K. Mukherjee, Rev. Adv. Mater. Sci. 10 (2005)185.

[25] M. Cain, R. Morrell, *Appl. Organomet. Chem.* 15 (2001) 321.

[26] Z.A. Munir, U. Anselmi-Tamburini, M. Ohyanagi, *J. Mater. Sci.* 41 (2006) 763.

[27] M. Suganuma, Y. Kitagawa, S. Wada, N. Murayama, *J. Am. Ceram. Soc.*, 86 (2003) 387-394.

[28] R. S. Mishra, A. K. Mukherjee, *Mater. Sci. Eng. A* A287 *(2000)* 178–82.

[29] T. Hungría, F. Houdellier, M. Algueró, A. Castro, *Phys. Rev.* B 81 (2010) 100102.

[30] Z. Shen, M. Johnsson, Z. Zhao, M. Nygern, *J. Amer. Ceram. Soc.* 85 (2002) 1921.

[31] M. Tokita, *Proceeding of NEDO International Symposium on Functionally Graded Materials, Kyoto, Japan,* (1999) 23–33.

[32] M. A. Meyers, K. K. Chawla, *Mechanical Behavior of Materials,* 2nd Ed., (Cambridge University. Press, Cambridge, 2009)

[33] J. Schiøtz, K. W. Jacobsen, *Science* 301 (2003) 1357–1359.

[34] J. Schiøtz, F. D. Di Tolla, K. W. Jacobsen, *Nature* 391 (1998) 561.

[35] J. Schiøtz, T. Vegge, F. D. Di Tolla, K. W. Jacobsen, *Phys. Rev. B* 60 (1999) 11971.

[36] L. L. Shaw, A. L. Ortiz, J. C. Villegas, *Scripta Mater.* 58 (2008) 951–954.

[37] M. Ohring, *Material Science of Thin Films*, 2nd Ed., (Academic Press, London, 2002).

[38] S. Zhang, D. D. Jayaseelan, G. Bhattacharya, W. E. Lee, *J. Am. Ceram. Soc.* 89 (2006) 1724.

[39] C. Aksel, B. Rand, F. L. Riley, P. D. Warren, *J. Euro. Ceram. Soc.* 24 (2004) 2839-2845.

[40] T. Yamamura, T. Hamazaki, H. Kato, *Taikabutsu Overseas* 12 (1992) 21–27

[41] C. Wang, Z. Zhao, *Scripta Mater.* 61 (2009) 193-196.

[42] J. M. Sands, C. G. Fountzoulas, G. A. Gilde, P. J. Patel, *J. Euro. Ceram. Soc.* 29 (2009) 261.

[43] D. R. Wilson, R. M. Evans, I. Wadsworth, J. Cawley, *Proc. UniteCR* 93 (1993), 749–760

[44] Morita, K., B. N. Kim, K. Hiraga, Y. Sakka, (2003). *Mater. Sci. Forum* 447-8 (2004) 329.

[45] R. Sarkar, S. Chatterjee, B. Mukherjee, H. S. Tripathi, M. K. Haldar, S. K. Das, A. Ghosh, *Ceram. Int.* 29 (2003) 195-198.

[46] D. T. Jiang., D. M. Hulbert, J. D. Kuntz, U. Anselmi-Tamburini, A. K. Mukherjee, *Mater. Sci. Eng. A* 463 (2007) 89-93.

[47] B. N. Kim, K. Hiraga, Y. Sakka, B. W. Ahn, *Acta Mater.* 47 (1999) 3433-3439.

[48] H. Lou, F. Wang, B. Xia, L. Zhang, *Oxid. Met.* 38 (1992) 299-307.

[49] R. Darolia, *JOM* 43 (1991) 44-49.

[50] J. C. Slater, *Phys. Rev.* 49 (1936) 0537-0545.

[51] K. S. Kumar, S. Suresh, M. F. Chisholm, J. A. Horton, P. Wang, *Acta Mater.* 51 (2003) 387-405.

[52] T. H. Courtney, *Mechanical behavior of materials*, 2nd Ed., (McGraw-Hill, Inc, New York, 1990).

[53] H. Conrad, *Met. Mater. Trans.* 35A (2004) 2681.

[54] T. B. Holland, I. A. Ovid'ko, H. Wang, A. K. Mukherjee, *Mater. Sci. Eng. A* 528 (2010) 663-671.

[55] Y. T. Zhu, X. L. Wu, X. Z. Liao, J. Narayan, L. J. Kecskes, S. N. Mathaudhu, *Acta Mater.* 59 (2011) 812-821.

[56] J. G. Bednorz, K. A. Muller, *Z. Phys. B* 64 (1986) 189-193

[57] P. N. Barnes, M. D. Sumption, G. L. Rhoads, *Cryogenics* 45(2005) 670.

[58] N. Fujiwara, H. Hayashi, S. Nagaya, Y. Shiohara, *Physica C* 470 (2010) 980.

[59] S. Mukoyama, M. Yagi, H. Hirano, Y. Yamada, T. Izumi, Y. Shiohara, *Physica C* 445 (2006) 1050.

[60] D. L. Shi, M. S. Boley, J. G. Chen, M. Tang, U. Welp, W. K. Kwok, B. Malecki. *Supercond. Sci. Technol* 2 (1989) 255-260.

[61] H. Safar, S. Foltyn, H. Kung, M. P. Maley, J. O. Willis, P. Arendt, X.D. Wu, *Appl. Phys. Lett.* 68 (1996) 1853.

[62] J. A. Kilner, Y. P. Li, *Nucl. Instrum. Methods Phys. Res.* 139 (1998) 108-119.

[63] C. J. Jou, J. Washburn, *J. Mater. Res.* 4 (1989) 795.

[64] A. S. Raynes, S. W. Freiman, F. W. Gayle, D. L. Kaiser, *J. Appl. Phys.* 70 (1991) 5254-5257.

[65] R. C. Pohanka, S. W. Freiman, B. A. Bender, *J. Am. Ceram. Soc.,* 61*(1978)* 72–75.

[66] B.Y. Oh, M. C. Jeong, T. H. Moon, W. Lee, J. M. Myoung, *J. Appl. Phys.* 99 (2006) 124505.

[67] J. W. Kang, W. I. Jeong, J. J. Kim, H. I. Kim, D, J. Kim, G. H. Lee, *Electrochem. Solid St.* 10 (2007) J75-J78.

[68] K. Matsubara, P. Fons, K. Iwata, A. Yamada, K. Sakurai, H. Tampo, S. Niki, *Thin Solid Films*, 431 (2003) 369-372.

[69] H. Kim, J. S. Horwitz, W. H. Kim, A. J. Mäkinen, Z. H. Kafafi, D. B. Chrisey, *Thin Solid Films*, 420 (2002) 539-543.

[70] T. Minami, *Thin Solid Films*, 516 (2008) 5822-5828.

[71] Z. L.Wang, *J. Phys. Condens. Mat.* 16 (2004) R829–R858.

[72] K. Matsubara, P. Fons, K. Iwata, A. Yamada, S. Niki, *Thin Solid Films* 422 (2002) 176-179.

[73] H. Agura, A. Suzuki, T. Matsushita, T. Aoki, M. Okuda, *Thin Solid Films* 445 (2003) 263-267.

[74] N. Fujimura, T. Nishihara, S. Goto, J. Xu, T. Ito, *J. Cryst. Growth* 130 (1993) 269-279.

[75] B. L. Zhu, X. Z. Zhao, S. Xu, F. H. Su, G. H. Li, X. G. Wu, J. Wu, R. Wu, J. Liu, *Jpn. J. Appl. Phys.* 47 (2008) 2225-2229.

[76] T. Minami, H. Sato, H. Imamato, S. Takata, Jpn. *J. Appl. Phys.* 31 (1992) L257.

[77] H. Sato, T. Minami, T. Miyata, S. Takata, M. Ishii, *Thin Solid Films* 246 (1994) 65.

[78] S. M. Park, T. Ikegami, K. Ebihara, *Jpn. J. Appl. Phys*. 44 (2005) 8027.

[79] M. Jin, A. M. Minor, E. A. Stach, J. W. Morris, *Acta Mater.* 52 (2004) 5381-5387.

[80] S. H. Oh, M. Legros, D. Kiener, G. Dehm, *Nat. Mater*. 8 (2009) 95-100.

[81] Z. W. Shan, R. K. Mishra, S. A. Syed Asif, O. L. Warren, A. M. Minor, *Nat. Mater*. **7** (2008) 115-119.

[82] N. Li, J. Wang, J. Y. Huang, A. Misra, X. Zhang, *Scripta Mater* 63 (2010) 363-366**.**

[83] N. Li, J. Wang, A. Misra, X. Zhang, J.Y. Huang, J.P. Hirth, *Acta Mater*. 59 (2011) 5989-5996.

[84] H. Zheng, A. Cao, C. R. Weinberger, J. Y. Huang, K. Du, J. Wang, Y. Ma, Y. Xia, S. X. Mao, *Nat. Commun.* (2010) 1.

[85] Y. Lu, J. Y. Huang, C. Wang, S. Sun, J. Lou, *Nat. Nanotechnol.* 5 (2010) 218-224.

[86] R. C. Hugo, H. Kung, J.R. Weertman, R. Mitra, J.A. Knapp, D.M. Follstaedt, *Acta Mater.* 51 (2003) 1937-1943.

[87] T. Ohmura, A. M. Minor, E.A. Stach, J.W. Morris, Jr., *J. Mater. Res.* 19 (2004) 3626-3632.

[88] J. Y. Huang, H. Zheng, S. X. Mao, Q. Li, G. T. Wang, *Nano Lett.* 11 (2011) 1618-1622.

[89] A. Asthana, K. Momeni, A. Prasad, Y. K. Yap, R. S. Yassar, *Nanotechnology* 22 (2011) 265712.

[90] R. Agrawal, B. Peng, E. E. Gdoutos, H. D. Espinosa, *Nano Lett.* 8 (2008) 3668-3674.

[91] Y. Yu, C. H. Jin, R. H. Wang, Q. Chen, L.-M. Peng, *J. Phys. Chem. B* 109 (2005) 18772-18776.

[92] J. Y. Huang, L. Zhong, C. Min Wang, J. P. Sullivan, W. Xu, L. Q. Zhang, S. X. Mao, N. S. Hudak, X. H. Liu, A. Subramanian, H. Fan, L. Qi, A. Kushima, J. Li, *Science* 330 (2010) 1515-1520.

[93] Z. Xu, D. Golberg, Y. Bando, *Nano Lett.* 9 (2009) 2251-2254.

[94] A. M. Minor, E. A. Stach, J. W. Morris, Jr, I. Petrov, *J. Electron. Mater.* 32 (2003) 1023-1027.

[95] J. Y. Huang, F. Ding, B. I. Yakobson, *Phys. Rev. Lett.* 100 (2008) 035503.

[96] J. Y. Huang, S. Chen, Z. F. Ren, Z. Q. Wang, D. Z. Wang, M. Vaziri, Z. Suo, G. Chen, M. S. Dresselhaus, *Phys. Rev. Lett.* 97 (2006) 075501.

[97] J. Y. Huang, F. Ding, B. I. Yakobson, P. Lu, L. Qi, J. Li, *P. Natl. Acad. Sci.USA* 106 (2009) 10103-10108.

[98] X. H. Liu, H. Zheng, L. Zhong, S. Huang, K. Karki, L. Qi. Zhang, Y. Liu, A. Kushima, W. T. Liang, J. W. Wang, J.-H. Cho, E. Epstein, S. A. Dayeh, S. T.

Picraux, T. Zhu, J. Li, J. P. Sullivan, J. Cumings, C. Wang, S. X. Mao, Z. Z. Ye, S. Zhang, J. Y. Huang, *Nano Lett.* 11 (2011) 3312-3318.

[99] H. S. Leipner, D. Lorenz, A. Zeckzer, H. Lei, P. Grau, *Physica B* 308 (2001) 446-449.

[100] J. W. Yan, H. Takahashi, X. Gai, H. Harada,J. Tamaki, T. Kuriyagawa, *Mat. Sci. Eng. A-Struct.* 423 (2006) 19-23.

[101] Y. T. Zhu, J. Narayan, J. P. Hirth, S. Mahajan, X. L. Wu, X. Z. Liao, *Acta Mater.* 57 (2009) 3763-3770.

[102] J. R. Greer, W. D. Nix, *Phys. Rev. B* 73 (2006) 245410-1.

[103] B. M. Wen, J. E. Sader, J. J. Boland, *Phys. Rev. Lett.* 101 (2008) 175502-1.

[104] D. B. Williams, *Practical Analytical Electron Microscopy in Materials Science*, Philips Electronic Instruments, Inc. Electron Optics Publishing Group, NewJersey, 1984.

[105] D. B. Williams, C. B. Carter, *Transmission Electron Microscopy*, (Plenum Press, New York, 1996).

[106] A.C.Fischer-Cripps, *Nanoindentation*, Presentation in CSIRO Division of Telecommunications and Industrial Physics, Lindfield, NSW Australia.

[107] K. L. Johnson, *Contact mechanics.* (Cambridge Univ Press, New York, 1996).

[108] J. H. Lee, I. Kim, D. M. Hulbert, D. Jiang, A. K. Mukherjee, X. Zhang, H. Wang, *Acta Mater.* 58 (2010) 4891.

[109] J. H. Lee, X. Zhang, H. Wang, *J. Appl. Phys.* 109 (2011) 083510.

[110] B. D. Cullity, *Elements of X-Ray Diffraction*, (Addison-Wesley Publishing Co., Inc. 1982).

[111] L. Azaroff, R. Kaplow, N. Kato, R. Weiss, A. Wilson, R. Young, *X-ray Diffraction*, (Mc. Gtaw-Hill, Inc., New York, 1974).

[112] D. Dijkkamp, T. Venkatesan, X. D. Wu, S. A. Shareen, N. Jiswari, Y. H. Min-Lee, W. L. McLean, M. Croft, *Appl. Phys. Lett.* 51 (1987) 619.

[113] R. K. Singh, O. W. Holland, J. Narayan, *J. Appl. Phys.* 68 (1990) 233.

[114] R. K. Singh, J. Narayan, *Phys. Rev. B* 41 (1990) 8843.

[115] C. Suryanarayana, C. C. Koch, *Hyperfineinteract* 130 (2000)5.

[116] B. Q. Han, E. J. Lavervia, F. A. Mohamed, *Rev. Adv. Mater. Sci.* 9 (2005) 1.

[117] A. A. Voevodin, A. V. Prasad, J. S. Zabinski, *J. Appl. Phys.* 82 (1997) 855.

[118] S. H. Kim, S. W. Lee, T. Sekino, T. Kusunose, T. Nakayama, K. Niihara, *J. Ceram. Soc. Jpn.* 112 (2004) 1079.

[119] G. Das, *Ceram. Eng. Sci. Proc.* 17 (1996) 25.

[120] L. E. McCandlish, V. Kevorkian, K. Jia, T. E. Fischer, *Advances in Powder Metallurgy Particulate Materials.* (In: C. Lall, A. J. Neupaver, editors. Princeton: Metal Powder Industries Federation, 1994).

[121] G. Zhan, J. Kuntz, J. Wan, J. Garay, A. K. Mukherjee, *Scripta Mater.* 47 (2002) 737.

[122] J. Wan, R. Duan, A. K. Mukherjee, *Scripta Mater.* 53 (2005) 663.

[123] A. K. Mukherjee, J. E. Bird, J. E. Dorn, *ASM Trans. Q* 62 (1969) 155.

[124] X. Zhou, D. M. Hulbert, J. D. Kuntz, R. K. Sadangi, V. Shukla, B. H. Kear, A. K. Mukherjee, *Mater. Sci. Eng. A* 394 (2005) 353.

[125] S. Ishihara, K. Akashiro, T. Tanizawa, N. Furushiro, Y. Umakoshi, S. Hori, *Mater. T Jim* 41 (2000) 376.

[126] A. M. Minor, S. A. S. Asif, Z. Shan, E. A. Stach, E. Cyrankowski, T. J. Wyrobek, O. L. Warren, *Nat. Mater*. 5 (2006) 697.

[127] Z. Shan, E. A. Stach, J. M. K. Wiezorek, J. A. Knapp, D. M. Follstaedt, S. X. Mao, *Science* 305 (2004) 654.

[128] D. M. Hulbert, D. Jiang, J. D. Kuntz, Y. Kodera, A. K. Mukherjee, *Scripta Mater*. 56 (2007) 1103.

[129] D. W. Stollberg, J. M. Hampikian, L. Riester, W. B. Carter, *Mater. Sci. Eng. A* 359 (2003) 112.

[130] S. Bhaduri, S. B. Bhaduri, *Ceram. Int*. 28 (2002) 153.

[131] M. G. Zelin, M. R. Dunlap, R. Rosen, A. K. Mukherjee, *J. Appl. Phys*. 74 (1993) 4972.

[132] M. G. Zelin, A. K. Mukherjee, *Acta Metall. Mater*. 43 (1995) 2359.

[133] M. G. Zelin, A. K. Mukherjee, *Philos. Mag. A* 68 (1993) 1183.

[134] A. V. Sergueeva, N. A. Mara, N. A. Krasilnikov, R. Z. Valiev, A. K. Mukherjee, *Philos. Mag*. 86 (2006) 5797.

[135] A. V. Sergueeva, N. A. Mara, A. K. Mukherjee, *Mater. Sci. Eng. A* 463 (2007) 8.

[136] M. W. Barsoum, *Fundamentals of ceramics* (Taylor and Francis Group, UK, 2003.)

[137] D. D. Upadhyaya, S. K. Roy, G. K. Dey, S. B. Banerjee, *Mater. Sci.* 17 (1994) 875.

[138] M. K. Wu, J. R. Ashburn, C. J. Torng, P. H. Hor, R. L. Meng, *Phys. Rev. Lett.* 58 (1987) 908.

[139] S. R. Foltyn, L. Civale, J. L. MacManus-Driscoll, Q. X. Jia, B. Maiorov, H. Wang, M. Maley, *Nat. Mater*. 6 (2007) 631-642.

[140] T. Okudera, A. Murakami, K. Katagiri, K. Kasaba, Y. Shoji, K. Noto, N. Sakai, M. Murakami, *Physica C* 392-396 (2003) 628 – 633 .

[141] H. Fujimoto, M. Murakami, N. Koshizuka. *Physica C* 203 (1992) 103.

[142] X. W. Zhou, H. N. G. Wadley, *Acta Mater*. 47 (1999) 1063.

[143] A. Nagasawa, S. Ogawa, *J. phys. Soc. Japa*n 15 (1960) 1421.

[144] L. Lu, R. Schwaiger, Z. W. Shan, M. Dao, K. Lu, S. Suresh, *Acta Mater*. 53 (2005) 2169.

[145] Y.F. Shen, L. Lu, Q.H. Lu, Z.H. Jin, K. Lu, *Scripta Mater*. 52 (2005) 989.

[146] O. Anderoglu, A. Misra, H. Wang, F. Ronning, M. F. Hundley, X. Zhang, *Appl. Phys. Lett.* 93 (2008) 083108.

[147] A. Frøseth, H. Van Swygenhoven, P. M. Derlet, *Acta Mater*. 52 (2004) 2259.

[148] S. K. Chen, L. Zhou, K. G. Wang, X. Z. Wu, P. X. Zhang, Y. Feng, *Physica C* 377 (2002) 571.

[149] W. K. Kwok, U. Welp, V. M. Vinokur, S. Fleshler, J. Downey, G. W. Crabtree, *Phys. Rev. Lett.* 67 (1991) 390.

[150] I. F. Voloshin, A. V. Kalinov, L. M. Fisher, K. I. Kugel, A. L. Rakhmanov, *J. Exp. Theor. Phys.* 84 (1997) 1177.

[151] Z. Ye, Q. Li, Y. Hu, W. D. Si, P. D. Johnson, Y. Zhu, *Appl. Phys. Lett.* 87 (2005) 122502.

[152] H. Yamasaki, Y. Nakagawa, A. Sawa, H. Obara, K. Develos, *Physica C* 372−376 (2002) 1885−1889.

[153] J.J. Roa, E. Jiménez-Piqué, X.G. Capdevila and M. Segarra, *J. Eur. Ceram. Soc.* 30 (2010) 1477.

[154] H. Fujimoto, M. Murakami, N. Koshizuk, *Physica C* 203 (1992) 103.

[155] Y. Yoshino, A. Iwabuchi, K. Katagiri, K. Noto, N. Sakai, M. Murakami, *IEEE Trans. Appl. Supercond.* 12 (2002) 1755.

[156] H. Mecking, U. F. Kocks, *Acta metall.* 29 (1981) 1865-1875.

[157] P. Franciosi, M. Berveiller, A. Zaoui, *Acta Metall.* 28 (1980) 273-283.

[158] B. Devincre, T. Hoc, L. Kubin, *Science* 320 (2008) 1745-1748.

[159] U. F. Kocks, H. Mecking, *Prog. Mater. Sci.* 48 (2003) 171-273.

[160] E. O. Hall, *Proc. Phys. Soc. B* 64 (1951) 747-753.

[161] N. J. Petch, *J. Iron Steel Inst.* 174 (1953) 25-28.

[162] W. M. Lomer, *Phil. Mag.* 42 (1951) 1327-1331.

[163] A. H. Cottrell, *Phil. Mag.* 43 (1952) 645-647.

[164] X. Zhang, A. Misra, H. Wang, M. Nastasi, J. D. Embury, T. E. Mitchell, R. G. Hoagland, J. P. Hirth, *Appl. Phys. Lett.* 84 (2004) 1096-1098.

[165] Bouaziz, S. Allain, C. Scott, *Scripta Mater.* 58 (2008) 484-487.

[166] K. A. Afanasyev, F. Sansoz, *Nano Lett.* 7 (2007) 2056-2062.

[167] V. V. Bulatov, L L. Hsiung, M. Tang, A. Arsenlis, M. C. Bartelt, W. Cai, J. N. Florando, M. Hiratani, M. Rhee, G. Hommes, T. G. Pierce, T. D. de la Rubia, *Nature* 440 (2006) 1174-1178.

[168] Z. Budrovic, H. V. Swygenhoven, P. M. Derlet, S. V. Petegem, B. Schmitt, *Science* 304 (2004) 273–276.

[169] X. L. Wu, Y. T. Zhu, Y. G. Wei, Q. Wei, *Phys. Rev. Lett*. 103 (2009) 205504-1-4.

[170] V. Yamakov, D. Wolf, S. R. Phillpot, A. K. Mukherjee, H. Gleiter, *Nature Mater*.3 (2004) 43-47.

[171] Y. H. Zhao, T. Topping, J. F. Bingert, J. J. Thornton, A. M. angelewicz, Y. Li, W. Liu, Y. Zhu, Y. Zhou, E. J. Lavernia, *Adv. Mater.* 20 (2008) 3028-3033.

[172] H. Cottrell, *Dislocations and Plastic Flow in Crystals.* (Oxford University Press, London, 1953.)

[173] M. Niewczas, R. G. Hoagland, *Phil. Mag.* 89 (2009) 727-746.

[174] J. P. Hirth**,** J. Lothe**,** *Theory of Dislocations* **(**Krieger, Malabar, ed. 2, Florida, 1982).

[175] X. Zhang, A. Misra, H. Wang, A. L. Lima, M. F. Hundley, R. G. Hoagland, *J. Appl. Phys.* 97 (2005) 094302.

[176] Anderoglu, A. Misra, J. Wang, R.G. Hoagland, J.P. Hirth, X. Zhang, *Int. J. Plasticity* 26 (2010) 875-886.

[177] X. D. Liu, E. Y. Jiang, Z. Q. Li, *J. Appl. Phys*., 102 (2007) 073708-073708-4.

[178] Z. F. Liu, F. K. Shan, Y. X. Li, B. C. Shin, Y. S. Yu, *J. Cryst. Growth*, 259 (2003) 130-136.

[179] D. H. Kim, N. G. Cho, H. G. Kim, W. Y. Choi, *J. Electrochem. Soc.*, 154 (2007) H939-H943.

[180] S. S. Lin, J. G. Lu, Z. Z. Ye, H. P. He, X. Q. Gu, L. X. Chen, J. Y. Huang, B. H. Zhao, *Solid State Commun.*, 148 (2008) 25-28.

[181] W. Jun, Y. Yintang, *Mater. Lett.*, 62 (2008) 1899-1901.

[182] V. Vaithianathan, B. T. Lee, S. S. Kim, *Phys. Status Solidi. A.*, 201 (2004) 2837-2840.

[183] S. Chakrabarti, B. Doggett, R. O'Haire, E. McGlynn, M. O. Henry, A. Meaney, J. P. Mosnier, *Superlattice Microst.*, 42 (2007) 21-25.

[184] T. Ohgaki, N. Ohashi, H. Kakemoto, S. Wada, Y. Adachi, H. Haneda, T. Tsurumi, *J. Appl. Phys.*, 93 (2003) 1961-1965.

[185] K. Haga, M. Kamidaira, Y. Kashiwaba, T. Sekiguchi, H. Watanabe, *J. Cryst. Growth*, 214 (2000) 77-80.

[186] V. Musat, B. Teixeira, E. Fortunato, R. C. C. Monteiro, P. Vilarinho, *Surf. Coat. Tech.*, 180-81 (2004) 659-662.

[187] W. Gao, Z. W. Li, *Ceram. Int.*, 30 (2004) 1155-1159.

[188] M. Kawakami, A. B. Hartanto, Y. Nakata, T. Okada, *Jpn. J. Appl. Phys.* 42 (2003) L33-L35.

[189] J. A. A. Selvan, A. E. Delahoy, S. Guo, Y. M. Li**,** *Sol. Energ. Mat. Sol. C.*, 90 (2006) 3371-3376.

[190] O. Kluth, G. Schöpe, J. Hüpkes, C. Agashe, J. Müller, B. Rech, *Thin Solid Films*, 442 (2003) 80-85.

[191] H. Kim, J. S. Horwitz, S. B. Qadri, D. B. Chrisey, *Thin Solid Films*, 420 (2002) 107-111.

[192] I. Volintiru, M. Creatore, B. J. Kniknie, C. I. M. A. Spee, M. C. M. van de Sanden, *J. Appl. Phys.*, 102 (2007) 043709.

[193] S. Choopun, R. D. Vispute, W. Noch, A. Balsamo, R. P. Sharma, T. Venkatesan, A. Iliadis, D. C. Look, *Appl. Phys. Lett.*, 75 (1999) 3947-3949.

[194] A. Infortuna, A. S. Harvey, L. J. Gauckler, *Adv. Funct. Mater.* 18 (2008) 127-135.

[195] O. Kluth, A. Löffl, S. Wieder, C. Beneking, L. Houben, B. Rech, H. Wagner, S. Waser, J. A. Selvan, H. Keppner, *Proceedings of the 26th IEEE PVSEC* 0160-8371 (1997) 715–718.

[196] H. Kim, A. Pique, J. S. Horwitz, H. Murata, Z. H. Kafafi, C. M. Gilmore, D. B. Chrisey, *Thin Solid Films* 377–378 (2000) 798.

[197] P. F. Carcia, R. S. McLean, M. H. Reilly, G. Nunes Jr., *Appl. Phys. Lett.* 82 (2003) 1117.

[198] U. Ozgur, Y. I. Alivov, C. Liu, A. Teke, M. A. Reshchikov, S. Dogan, V. Avrutin, S. J. Cho, H. Morkoc, *J. Appl. Phys.* 98 (2005) 041301.

[199] Y. H. Tong, Y. C. Liu, C. L. Shao, Y. X. Liu, C. S. Xu, J. Y. Zhang, Y. M. Lu, D. Z. Shen, X. W. Fan, *J. Phys. Chem. B* 110 (2006) 14714.

[200] G.-C. Yi, C. Wang, W. I. Park, *Semicond. Sci. Technol.* 20 (2005) S22.

[201] C. Hsu, S. Chang, H. Hung, Y. Lin, C. Huang, Y. Tseng, I. Chen, *J. Electrochem. Soc.* 152 (2005) G378.

[202] W. G. Carlson, T. K. Gupta, *J. Appl. Phys.* 53 (1982) 5746.

[203] W. C. Long, J. Hu, J. Liu, J. L. He, R. Zong, *J. Am. Ceram. Soc.* 93 (2010) 2441–4.

[204] M. Berginski, J. Hüpkes, M. Schulte, G. Schöpe, H. Stiebig, B. Rech, M. Wuttig, *J. Appl. Phys.* 101 (2007) 074903.

[205] M. Alaf, M. O. Guler, D. Gultekin, M. Uysal, A. Alp, H. Akbulut, *Vacuum* 83 (2009) 292–301.

[206] J. P. Jernot, J. L. Chermant, M. Coster, *Powd. Tech.* 30 (1981) 31.

[207] L. Makhele-Lekala, S. Luyckx, F. R. N. Nabarro, *Int. J. Refract. Met. Hard Mater.* 19 (2001) 245–249.

[208] S. Choi, J. Lee, *J. Vac. Sci. Technol. A* 19 (2001) 2043.

[209] J. H. Lee, C.-Y. Chou, Z. Bi, C.-F. Tsai, H. Wang, *Nanotechnology* 20 (2009) 395704.

[210] H. McMurdie, M. Morris, E. Evans, B. Paretzkin, W. Ettling, L. Ettlinger, *Powder Diffraction* 1 (1986) 76.

[211] A.Yamada, P. J. Fons, R. Hunger, K. Iwata, K. Matsubara, S. Niki, *Appl. Phys. Lett.* 79 (2001) 608.

[212] C. M. Wang, L. V. Saraf, Y. Qiang, *Thin Solid Films* 516 (2008) 8337.

[213] M. Peruzzi, J.D. Pedarnig, D. Bäuerle, W. Schwinger, F. Schäffler, *Appl. Phys. A* 79 (2004) 1873.

[214] H. Kim, J. S. Horwitz, S. B. Qadri, D. B. Chrisey, *Thin Solid Films* 420–421 (2002) 107-111.

[215] T. Minami, *MRS Bull.* 25 (2000) 38.

[216] A. F. Mayadas, M. Shatzkes, *Phys. Rev. B* 1 (1970) 1382.

[217] S. J. Jiao, Z. Z. Zhang, Y. M. Lu, D. Z. Shen, B. Yao, J. Y. Zhang, B. H. Li, D. X. Zhao, X. W. Fan, Z. K. Tang, *Appl. Phys. Lett. 88 (*2006) 031911.

[218] A. Tsukazaki, M. Kubota, A. Ohtomo, T. Onuma, K. Ohtani, H. Ohno, S.F. Chichibu, M. Kawasaki, *Jpn. J. Appl. Phys.* 44 (2005) L643-L645.

[219] J. -H. Lim, C. -K. Kang, K. -K. Kim, I. -K. Park, D. -K. Hwang, S. -J. Park, *Adv. Mater.* 18 (2006) 2720-2724.

[220] W.W. Wenas, A. Yamada, M. Konagai, K. Takahashi, *J. Appl. Phys.* 70 (1991), 7119.

[221] P. M. Ratheesh Kumar, C. Sudha Kartha, K. P. Vijayakumar, T. Abe, Y. Kashiwaba, F. Shingh, D. K. Avasthi, *Semicond. Sci. Technol.* 20 (2005), 120-126.

[222] M.-Y. Choi, D. Choi, M.-J. Jin, I. Kim, S.-H. Kim, J.-Y. Choi, S. Y. Lee, J. M. Kim, S.-W. Kim, *Adv. Mater.* 21 *(2009)* 2185-2189.

[223] S. Xu, Y. Qin, C. Xu, Y. G. Wei, R. S. Yang, Z. L. Wang, *Nat. Nanotechnol.* 5 (2010) 366–373.

[224] J. Wang, A. J. Kulkarni, F. J. Ke, Y. L. Bai, M. Zhou, *Comput. Methods Appl. Mech. Eng.* 197 (2008) 3182.

[225] C. Q. Chen, Y. Shi, Y. S. Zhang, J. Zhu, Y. J. Yan, *Phys. Rev. Lett.* 96 (2006) 075505.

[226] A. V. Desai, M. A. Haque, *Sensors Actuators A* 134 (2007) 169-76.